OPTICAL RESPONSE OF DOPED ZINC OXIDE FILMS

By

DANIEL STEVEN HILDEBRAND

Bachelor of Science in Mechanical Engineering
Oklahoma State University
Stillwater, Oklahoma, USA
2009

Submitted to the Faculty of the
Graduate College of the
Oklahoma State University
in partial fulfillment of
the requirements for
the Degree of
MASTER OF SCIENCE
December, 2012

OPTICAL RESPONSE OF DOPED ZINC OXIDE FILMS

Thesis Approved:

Don A. Lucca

Thesis Adviser

Matt J. Klopfstein

Prabhakar R. Pagilla

Sheryl A. Tucker

Dean of the Graduate College

ACKNOWLEDGMENTS

First off, I would like to thank my wonderful wife Cate for continual support and encouragement throughout this entire experience. I would also like to thank my parents, my sisters, and Cate's family for the support and regular status update requests.

This work could not be done without the use of the facilities of the Ultraprecision Surfaces Group at Oklahoma State University. I would like to thank my advisor, Dr. Lucca, for giving me the opportunity to work as a research assistant in the lab, for continually working hard to find funding to support this work, and for exploring new directions of research to keep the lab thriving. I would like to thank Dr. Quanxi Jia of Los Alamos National Laboratory, who in large part provided the basis for this research. I would also like to thank Drs. Pagilla and Klopfstein for agreeing to serve on my thesis committee and for providing valuable feedback. A special gratitude is extended to Mr. Tres Harriman, who provided intellectual support and guidance that simply cannot be put into words. I would also like to thank Mr. Kyle Ford, Mr. Ali Shojaee, and Mr. Steven Qi of the Ultraprecision Surfaces Group for assisting me in the lab and helping me to understand the many complexities of this scientific field.

This work was performed, in part, at the Center for Integrated Nanotechnologies, a U.S. Department of Energy, Office of Basic Energy Sciences user facility at Los Alamos National Laboratory (Contract DE-AC52-06NA25396) and Sandia National Laboratories (Contract DE-AC04-94AL85000).

This material is based upon work supported by the National Science Foundation under Grant No. CMMI-0529085. Any opinions, findings, and conclusions or recommendations expressed in this material are those of the author and do not necessarily reflect the views of the National Science Foundation.

TABLE OF CONTENTS

LIST OF TABLES

LIST OF FIGURES

NOMENCLATURE

AFM	Atomic force microscopy
CCD	Charge-coupled device
CL	Cathodoluminescence
CVD	Chemical vapor deposition
cw	Continuous wave
D^0X	Donor bound exciton
DAC	Diamond anvil cell
DAP	Donor-acceptor pair
DMS	Diluted magnetic semiconductors
e	Electron charge
E	Energy
E_A	Thermal activation energy
ENDOR	Electron nuclear double resonance
E_{bulk}	Band gap of bulk crystal
E_{loc}	Localization energy
FWHM	Full width at half maximum
GL	Green luminescence
h	Planck's constant
$\hbar$	Reduced Planck's constant
HRTEM	High-resolution transmission electron microscopy
IR	Infrared-absorption
k	Thermal conductivity
LED	Light emitting diode
LO	Longitudinal optical
m	Mass
m_e^*	Effective mass of electron
m_h^*	Effective mass of hole

MBE	Molecular beam epitaxy
MW	Manoogian and Woolley
n	Index of refraction
NA	Numerical aperture
NBE	Near band-edge
NDT	Nondestructive Technique
p	Momentum
PECVD	Plasma enhanced chemical vapor deposition
PL	Photoluminescence
PLD	Pulsed laser deposition
PMMA	Poly(methyl methacrylate)
rf	Radio frequency
SEM	Scanning electron microscopy
SERS	Surface enhanced Raman spectroscopy
SNOM	Scanning near-field optical microscopy
T_m	Melting temperature
TEM	Transmission electron microscopy
TES	Two electron satellite
TO	Transverse optical
UV	Ultraviolet
v	Velocity
XRD	X-ray diffraction
ZPL	Zero phonon line
λ	Wavelength
θ_{D}	Debye temperature

Chapter 1

Introduction

1.1 Motivation for the Present Study

ZnO has historically been a very attractive semiconductor material in the scientific community largely due to its wide band gap (∼3.4 eV), large exciton binding energy (∼60 meV), and high transparency in the visible spectrum. The optical and electrical properties of ZnO have been extensively studied, but the ability to alter these properties has been a challenge. Reports of ZnO doped with many group III and transition metal ions have appeared, typically with the goal of modifying the electrical, optical, or magnetic properties of ZnO. Recent interest in Re-doped ZnO has emerged, however investigations of the properties and behavior of ZnO when doped with Re have not been reported. Re has not been extensively studied, and reports of doping semiconductor materials with Re are not common. In this study, the effects of doping ZnO with Re are investigated in order to understand the physics driving the changes observed in the optical response. By examining the vibrational modes and band structure of Re-doped ZnO, insight can be gained into the physical mechanisms taking place when Re is introduced to the ZnO lattice.

1.2 Objectives

The objective of the present study is to investigate the changes observed in ZnO when doped with Re and to identify the physical mechanisms responsible for these changes. Specifically, the objectives are to:

1. Characterize undoped and ReO_2 doped ZnO thin films deposited on *c*- and *r*-plane sapphire substrates using the following experimental techniques: X-ray diffraction (XRD), photolumi-

nescence (PL) spectroscopy, and Raman spectroscopy.

2. Compare results for undoped specimens to bulk single crystal ZnO to characterize the quality of undoped specimens.
3. Evaluate the effects of the substrate type on ReO_2 doped ZnO thin films.
4. Extract information such as localization energies, strain states, and Debye temperature from experimental data to evaluate the effects of doping ZnO with ReO_2 and to understand the physical mechanisms taking place when Re is incorporated into ZnO.

1.3 Approach

In order to achieve the objectives of this study, a variety of ZnO thin film specimens doped with ReO_2 were created. Undoped and ReO_2 doped ZnO films were deposited on either *c*-plane (0001) sapphire or *r*-plane $(1\bar{1}02)$ sapphire. The use of two substrates created a variation in initial film quality and state of strain. The concentration of ReO_2 was varied from 0 to 50 wt.% for specimens created on each substrate type. Each of the specimens was characterized using XRD to determine crystalline quality, orientation, and residual strain.

The films were initially characterized using XRD to verify crystallinity and to identify phases. Following initial characterization of the specimens, an investigation of the undoped specimens was carried out, the results of which were compared to bulk single crystal ZnO and reported results in the literature. Raman spectroscopy was used to characterize the bonding and chemical nature of the specimens, and the Raman spectra were compared to reported results for ZnO. PL spectroscopy was used to analyze the optical response at temperatures ranging from 4.2 to 300 K. Analysis of the fine band structure was conducted and each of the observed PL peaks were identified. PL behavior as a function of temperature was utilized to estimate localization energies and constants related to lattice dilatation and electron-phonon interaction. Finally, the same experiments were performed on the ReO_2 doped specimens and a comparison was made between PL and Raman spectra, localization energies, physical parameters, and states of strain.

Chapter 2

Background

Some background on the experimental techniques utilized in this study will be given followed by a discussion and literature review on ZnO and similar semiconductors. A review of studies focused on doping semiconductors to modify physical and optical properties will be given as well as a review of the properties of Re and a review of studies focusing on doping material systems with Re.

2.1 Optical Spectroscopy

Raman spectroscopy and photoluminescence (PL) spectroscopy were utilized as characterization tools in this study. Some of the mechanisms and principles of these techniques will be reviewed in this section.

2.1.1 Raman Spectroscopy

Raman spectroscopy is a nondestructive analysis technique that utilizes the Raman effect, or inelastic scattering of light. The Raman scattering effect in fluids was discovered by C. V. Raman in 1928 [1], and was later applied to solid materials. Raman scattering can be described as the change in frequency of a small portion of monochromatic light as a result of interacting with a material. When a monochromatic beam hits a molecule, Rayleigh scattering, or elastic scattering, is predominant. However, a small amount of Raman scattering can occur, and the change in wavelength is characteristic of the substance.

The classical treatment of first-order Raman scattering can be described by the energy level diagram in Fig. 2.1. An incident photon of energy $h\nu_0$ interacts with a material. In the case of Rayleigh scattering, the scattered photon has the same energy as the incident photon. However,

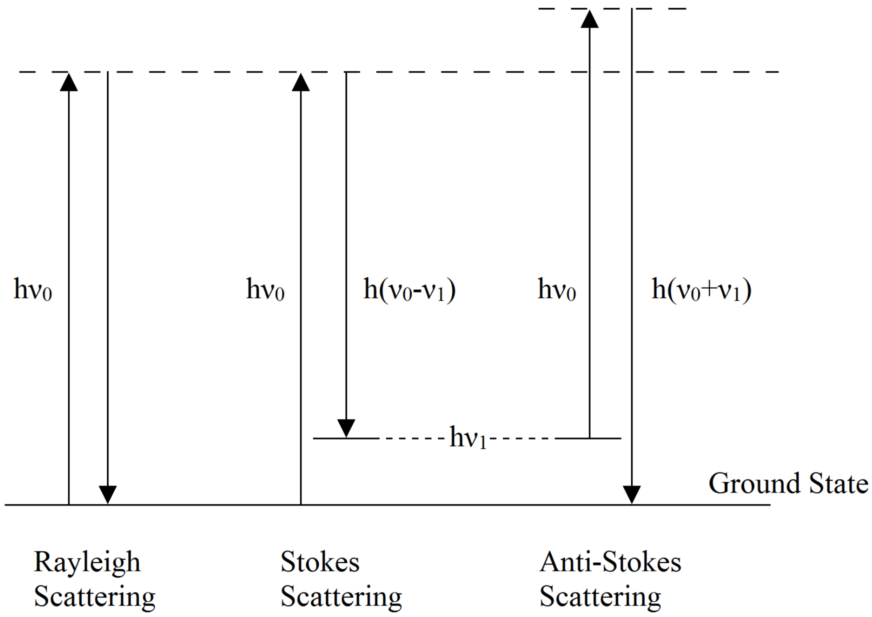

Figure 2.1: Schematic showing Rayleigh, Stokes, and anti-Stokes scattering.

when a state of energy $h\nu_1$ exists, attributed to molecules in an excited vibrational state, the incident photon may interact with the vibrational state and induce a change in the energy of the photon of either $h(\nu_0 + \nu_1)$ (anti-Stokes scattering) or $h(\nu_0 - \nu_1)$ (Stokes scattering) [2]. More specifically, the incident photon interacts with phonons, or lattice vibration quanta. The energy of the phonons in a given material system depends on the allowable lattice vibration frequencies.

Different types of bonding and crystal configurations in a material produce different vibrational modes. In a system with more than one type of atom with different sizes or bonding characteristics, two types of phonons exist. The vibration frequency of a lattice can be approximated as a function of wave vector $|\vec{k}| = 2\pi/\lambda$ by considering a linear chain of alternating atoms of mass m_1 and m_2 separated by a distance a and connected by springs with spring constant K, which results in the dispersion relation. The solution to this simplified dispersion relation is two branches, referred to as the acoustic and optical branches. As the wave vector approaches zero, or at long wavelengths, the acoustic branch becomes linear with slope ωa equal to the speed of sound [3]. Different types of atoms in a solid move in the same direction for acoustic modes [4]. The acoustic modes appear in the acoustic frequency range and therefore will not be detected with Raman spectroscopy. The optical mode is separated completely from the acoustic mode with a frequency typically in the optical range. Unlike the acoustic mode, the different types of atoms move in opposite directions for optical modes, or are out of phase [4].

In three-dimensional structures, multiple acoustic and optical modes exist. The number of acoustic and optical modes depends on the number of atoms per primitive cell in realistic structures [4]. Both types of modes may be longitudinally polarized, in which case the displacement of the atoms is in the same direction as the wave vector. The modes also may be transversely polarized, where the atoms move in planes normal to the wave vector. In summary, four types of modes may exist: longitudinal optical (LO), longitudinal acoustic (LA), transverse optical (TO), and transverse acoustic (TA).

Only vibration modes of certain symmetries result in Raman scattering—these are Raman-active modes, the selection rules for which may be determined using group-theory methods [5]. Raman spectroscopy experimental techniques have been developed to turn the analysis of vibrational modes of solids into a very powerful tool. To name a few, Raman spectroscopy has been used in defect studies [6], analysis of strain in semiconductors [7–9], and analysis of nanostructures [10] and their associated disorder [11].

2.1.2 Photoluminescence Spectroscopy

In PL spectroscopy, photons are used to excite electrons of charge $-e$ in a semiconductor from the valence band to the conduction band. The resulting vacant orbital in the valence band is termed a hole, which acts with a positive charge $+e$. The electron and hole may remain bound by their attractive Coulombic interaction, creating an exciton. When photons of sufficient energy are absorbed by a semiconductor, an electron becomes excited from the valence band to an energy state located in the conduction band. A non-radiative decay mechanism allows the electron to return to the bottom of the conduction band. Radiative recombination of the electron and hole occurs when the excited electron returns from the conduction band back to the valence band. When this occurs, a photon is emitted with energy near that of the band gap, or the difference in energy between the valence band-edge and the conduction band-edge of a material. This scenario is depicted graphically in Fig. 2.2.

The probing depth of PL for a material depends on the optical absorption of the material at the wavelength of the probing light. When probing depths are small, PL may be emitted from near the surface of a material, and thus can be utilized to characterize surfaces [12]. This can also be the case for very thin films or small particles with a large surface to volume ratio. Adsorbed molecules may be present and can act as mid-band gap states to which the electrons may be excited and may serve as long-lived traps [12]. Surface states typically include deep and shallow traps, the energy of which may be determined by the thermal activation energy of the transition [12]. When probing depths are high, the majority of PL is emitted from the bulk of a material. In addition to recombination from the conduction band to the valence band, structural defects such as vacancies, interstitial atoms, or substitutional atoms may provide an allowed defect state in the band gap. Upon recombination, these shallow traps, deep traps, or other intermediate states result in the emission of a photon of energy less than the band gap. The spectral location of a defect state PL peak can give insight into the type of defects, adsorbed molecules, or dopants in a material and thus can help indicate crystal quality.

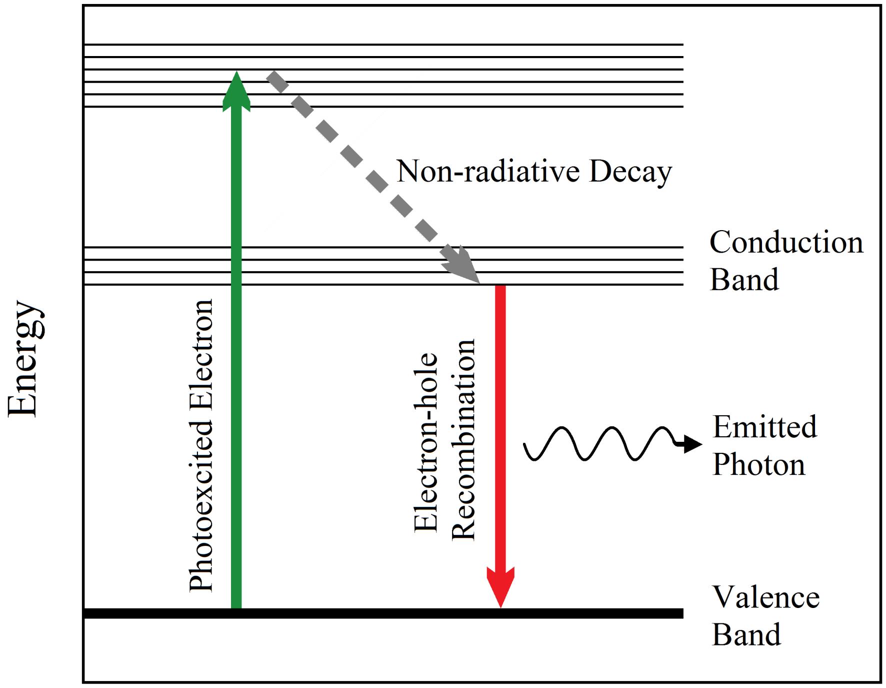

Figure 2.2: Schematic showing the most elementary PL emission process.

Radiative recombination typically occurs in semiconductors with direct band gaps. In a material with an indirect band gap, a change in momentum is required, thus causing inefficient radiative recombination. Thus semiconductors with indirect band gaps are less attractive for use in many applications and are more difficult to analyze with PL spectroscopy. Additionally, the long-lived traps described above can be non-radiative in nature [12]. If the recombination mechanisms are dominated by non-radiative transitions in a direct band gap semiconductor, very weak PL emission would result. Thus a decrease in PL intensity may indicate an increase in non-radiative traps and a decrease in semiconductor quality. A more extensive review of the mechanisms of PL can be found elsewhere [3,13].

2.2 Properties of ZnO

ZnO has attracted a great deal of attention in recent years, largely due to its wide direct band gap, large exciton binding energy (~60 meV), and high transparency in the visible range. ZnO nanoparticles have been shown to be a candidate for solar cells when implanted in PPV [14, 15]. Ultraviolet (UV) light emitting diodes (LED) have also been created using ZnO [16]. Table 2.1 lists some relevant properties of ZnO. Theoretical and experimental studies have focused on ZnO in many forms: single crystal bulk, epitaxial thin films, polycrystalline thin films, and a variety of nanostructures, including quantum dots, nanorods, nanotubes, and nanoribbons. Various synthesis techniques have been studied, and various materials have been doped or implanted in an attempt to alter some of the physical and electronic properties of ZnO.

Table 2.1: Wurtzite ZnO properties at 300 K.

Property	**Symbol**	**Value**	**Units**	**Reference**
Density	ρ	5.676	g cm^{-3}	[17]
Debye Temperature	θ_D	920	K	[18]
Energy Band Gap	E_g	3.437	eV	[19]
Hall Coefficient	R_H	-1.9×10^{-8}	$\text{m}^3\ \text{C}^{-1}$	[20]
Bulk Böhr Radius	a_B	1.4-2.2	nm	[21, 22]
Thermal Expansion Coef. [100]	da_0/dT	6.4×10^{-6}	K^{-1}	[23]
Thermal Expansion Coef. [001]	da_0/dT	4.3×10^{-6}	K^{-1}	[23]
LO phonon energy	$\hbar\omega_\text{LO}$	0.072	eV	[22]
TO phonon energy	$\hbar\omega_\text{TO}$	0.054	eV	[22]
Dielectric constant, x	ϵ_x	8.47		[22]
Dielectric constant, z	ϵ_z	8.84		[22]
Refractive index	n	2.0		[22]

2.2.1 Physical and Electrical Properties of ZnO

Most II-VI semiconductors crystallize in either a zinc-blende or wurtzite structure. ZnO is no exception, with the most common structure being wurtzite (space group $P6_3mc$), which forms at ambient thermodynamic conditions. ZnO will also crystallize with a rocksalt structure at high pressures and zinc-blende structure when grown on cubic substrates [24]. In the wurtzite structure, ZnO has been experimentally found to have lattice constants $a = 3.250$ Å and $c = 5.204$ Å [25], yielding a c/a ratio of 1.602.

ZnO naturally exhibits n-type conductivity, or in other words has an excess of negative charge carriers. The electrical properties of ZnO have a strong dependence on the quality of the semiconductor. The electrical conductivity of bulk single crystal ZnO has commonly been reported to be approximately 1 $\Omega^{-1}\text{m}^{-1}$ at room temperature [26–28]. Electron concentration has been reported in the range 1.1×10^{22} to 3.3×10^{26} m^{-3} with corresponding electron mobilities ranging from 6.4×10^{-5} to 3.0×10^{-2} $\text{m}^2\text{V}^{-1}\text{s}^{-1}$ [20, 29, 30].

2.2.2 Raman Spectrum of ZnO

Damen et al. [31] were amongst the first to observe the Raman spectrum of ZnO with the availability of the visible continuous gas laser. Raman and infrared-absorption (IR) experiments were performed along with a verification of the selection rules. Using group theory, it was predicted that there should be an A_1 branch, an E_1 branch, two E_2 branches, and two B branches. The E_1 and E_2 branches are doubly degenerate, meaning two states share each energy level. The E_2 modes are Raman active, and the A_1 and E_1 modes are both Raman and IR active. For the IR active A_1 and E_1 modes, electrostatic forces lift the degeneracy into two transverse optical (TO) branches and one longitudinal optical (LO) branch. The A_1 (TO), E_1 (TO), and E_1 (LO) modes are polarized in the xy-plane, whereas the A_1 (LO) mode is polarized parallel to the z-axis.

The E_2 peaks, denoted E_2^{low} and E_2^{high} based on phonon energy, exhibit very strong intensity relative to the other modes when polarized in the $x(yy)z$, $x(yx)z$, $z(xx)z'$, $z(xy)z'$, and $x(zz)x'$ directions, but have very low intensity in the other polarization directions [31, 32]. In the polarization convention used here, the directions inside the parenthesis denote the polarization directions of the incident (left) and scattered (right) light. The directions on the outside of the parenthesis denote the propagation directions of incident (left) and scattered (right) light. For example, $z(xy)z'$ refers to incident light propagating in the z-direction polarized in the x-direction, with scattered light being collected in the reverse z-direction polarized in the y-direction. This example is a backscattering configuration. Table 2.2 summarizes the expected Raman peak symmetries and corresponding wavenumber for ZnO.

Knowledge of the pressure dependence of the Raman modes of solids can be used to correlate an observed Raman shift with the approximate state of stress within the material. Sparks and Paesler [7]

Table 2.2: Raman peak symmetries and wavenumber expected for ZnO.

Common Name	**Mode Symmetry**	**Wavenumber ($\mathbf{cm^{-1}}$)**
E_2^{low}	E_2	101
A_1(TO)	A_1 (transverse)	380
E_1(TO)	E_1 (transverse)	407
E_2^{high}	E_2	437
A_1(LO)	A_1 (longitudinal)	574
E_1(LO)	E_1 (longitudinal)	583

estimated the residual stresses found in Ge and Si as a result of machining using Raman spectroscopy coupled with data for the hydrostatic pressure dependent shift of Raman peaks. For wurtzite single crystal bulk ZnO, Decremps et al. [33] analyzed the hydrostatic pressure dependence from atmospheric pressure up to the pressure at which ZnO shifts to the rocksalt structure (∼9 GPa). The Raman spectrum of bulk ZnO specimens with lateral dimensions of 30 μm by 20 μm and thickness 20 μm were analyzed in a diamond anvil cell (DAC). The 514.5 nm line of an Ar^+ laser focused to a spot diameter of 5 μm with power of about 500 mW at the DAC entrance was used as the light source. Scattered light was analyzed in backscattering configuration with a triple monochromator and CCD detector. The phonon energies of the A_1 (LO), A_1 (TO), E_1 (LO), E_1 (TO), and E_2^{high} modes increased with increasing pressure, whereas the phonon energy of the E_2^{low} peak decreased with increasing pressure. For each mode the phonon energy shift with pressure was small, thus Decremps et al. concluded that the bond ionicity has a weak dependence on pressure. Shifting of the E_2^{high} peak has also been observed as a result of As implantation, which was attributed to an increase in stress due to the incorporation of As [34]. Further correlations of Raman shifting to stress states were observed by Wermelinger and Spolenak [35] by analyzing the spatially resolved Raman spectrum below a Vickers microindentation. The same location was analyzed using atomic force microscopy (AFM). Shifts in the phonon energies of Raman peaks were observed around the indentation. The magnitude of the peak shifts at any given location correlated to the amount of plastic deformation as revealed by AFM.

2.2.3 Emission and Luminescence of ZnO

The optical properties and behavior of ZnO have made it very appealing to the scientific community. A summary of some key optical properties was shown in Table 2.1. A primary focus of research regarding ZnO has been on light emission and band gap analysis. The majority of research has either focused on the near band-edge emission near 3.4 eV or the defect emission in the visible part of the spectrum. A summary of studies on each follows.

Birman [36] analyzed the effects of polarization on the emission of zinc-blende and wurtzite structures, using experimental evidence from ZnS and CdS as examples. Figure 2.3 shows the band structure of zinc-blende and wurtzite structures as presented by Birman. The conduction band of wurtzite structures is *s*-like which leads to a symmetry at the center of the Brillouin zone of Γ_1. The valence band is *p*-like and is split into sub-bands as a result of crystal field splitting and spin orbit interaction [37]. Crystal field splitting originates from anisotropy of the static electric field due to the principal axis of the wurtzite structure. Neglecting crystal field splitting, wurtzite structures would have a valence band with Γ_4 symmetry, but due to crystal field splitting the Γ_4 band degeneracy is removed, which results in two bands of symmetry Γ_1 and Γ_5. The zinc-blende structure has an isotropic static electric field and thus does not exhibit crystal field splitting. The magnetic field generated by the orbit of an electron around the nucleus interacts with the electron's spin. For wurtzite structures, group theory predicts the spin orbit interaction to result in a splitting of the degenerate Γ_5 band into Γ_7 and Γ_9 bands, and Γ_1 symmetry transforms to Γ_7 symmetry [37]. This results in a conduction band with symmetry Γ_7 and valence sub-bands of symmetry Γ_9, Γ_7, and Γ_7. Using CdS as an example of the wurtzite structure, Birman [36] concluded that near band-edge polarization is a function of effective mass, matrix elements regarding structure, spin-orbit splitting, and temperature. It was also concluded that the excitation spectrum should be identical to that of the edge emission when using polarized light for excitation. Furthermore, the polarization of emitted light should be independent of the excitation polarization.

The near band-edge optical absorption and reflection spectra of ZnO were first systematically investigated experimentally in 1960 by Thomas [21]. Measurements were carried out at temperatures ranging from 4.2 K to 300 K. At 4.2 K, reflection peaks were observed at 3.377 eV, 3.3845 eV, and 3.4225 eV, designated the A, B, and C peaks, respectively, in accordance with the first, second, and third valence bands in Birman's model. Peaks from excited state transitions were also identified at 3.422 eV, 3.4275 eV, and 3.465 eV designated A′, B′, and C′, respectively. Thomas showed that the A and B peaks corresponded to excitons involving holes from bands polarized perpendicular to the

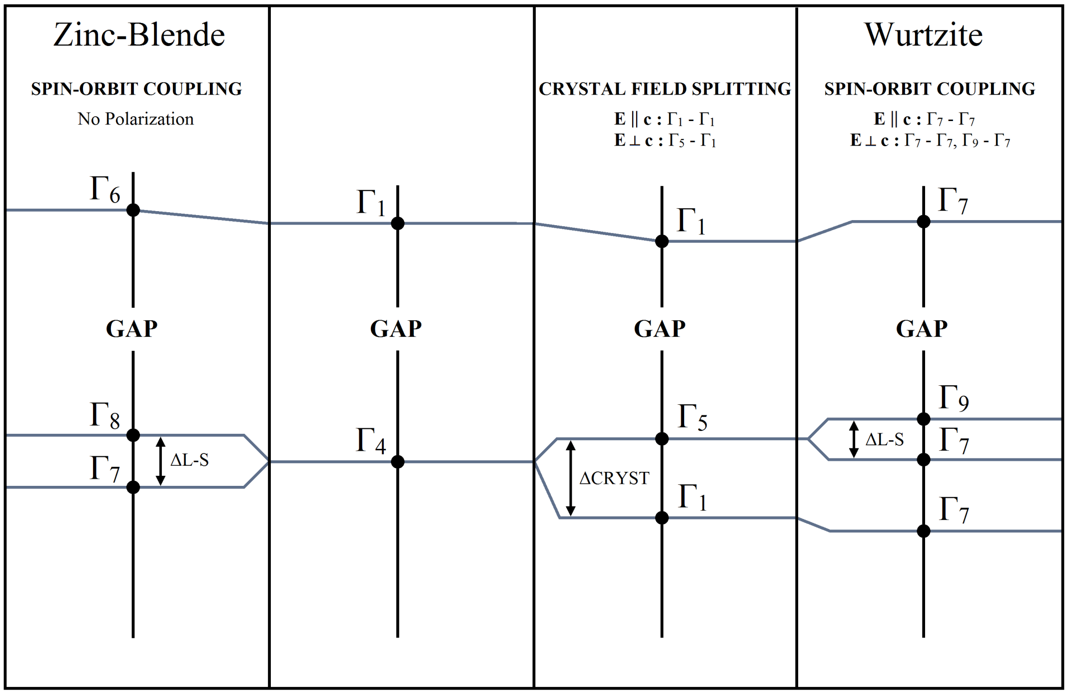

Figure 2.3: Band structure for zinc blende and wurtzite structures based on the Birman model.

c-axis, whereas the C peak corresponded to bands polarized parallel to the *c*-axis. It was concluded that the A, B, and C peaks originated from direct exciton transitions with energy n=1, one from each of the three valence bands. The designation of the A band as Γ_7 symmetry and the B band as Γ_9 symmetry, and thus an unsuccessful fit to Birman's model, were explained to be due to the reversing of the valence band symmetry ordering as a result of the mixing of the A and C hole bands.

Reynolds et al. [38] attempted to address this discrepancy from Birman's model by analyzing the Zeeman splitting effect from bound excitons. The study was based on a similar study of CdS [39], where it was shown that bound excitons split in a magnetic field. It was theorized that there should be significant differences in the behavior of the Zeeman splittings depending on whether a transition was $\Gamma_7 \leftrightarrow \Gamma_7$ or $\Gamma_7 \leftrightarrow \Gamma_9$. However, experimental results were inconclusive and the study was unable to definitively reveal the character of the band symmetries. Several bound exciton peaks were observed, designated $I_1 - I_{10}$, and detailed analyses were conducted on many of the peaks.

Park et al. [22] continued to study the exciton spectrum of ZnO, also utilizing optical absorption and reflection techniques. Similar to the results of Thomas, the three exciton bands A, B, and C were observed, although at slightly different energies. Additional associated excited states for the A band (n=1,2,3,4) were also observed. Several of the peaks attributed to bound excitons were also observed. It was found that the free exciton lines varied very little between specimens, whereas a great variability between specimens was observed for the bound exciton lines. As a result of differing assignments of certain peaks as compared to Thomas [21], Park et al. were able to obtain a better fit to the Birman model [36].

Further investigations were carried out by Liang and Yoffe [40] in a study utilizing optical transmission spectroscopy experiments on ZnO at various temperatures. The free exciton emission results were in agreement with those of Thomas, and the difference in the interpretation of the exciton structure by Park et al. was attributed to experimental problems. In more recent years, the availability of high quality ZnO crystals has enabled the observation of photoluminescence (PL) emission from free exciton transitions. Utilizing PL spectroscopy, Reynolds et al. [19] were able to address discrepancies with the symmetry states of the valence bands. PL measurements were taken with and without magnetic fields parallel to the *c*-axis, and with an electric field either parallel or perpendicular to the *c*-axis. Looking at the A-exciton transition, it was observed that the behavior of the line as a function of magnetic and electric field was consistent with the Γ_9 assignment, whereas the results could not be explained by a Γ_7 assignment. It was concluded that the A-exciton transition is of valence-band symmetry Γ_9, and the B- and C-exciton transitions are of symmetry Γ_7, which is the case for most II-VI wurtzite structures and the prediction of the Birman model [36]. In contrast to these results, Meyer et al. [41] suggested that the A-exciton assumed Γ_7 symmetry by analyzing a detailed magneto-optical study of the ionized donor bound exciton complex. However, the majority of recent research is in agreement with Reynolds et al. [19] and concludes that the symmetry follows the Birman model.

In addition to these studies of the free exciton transitions, several studies have focused on the bound excitons of ZnO. At low temperatures, very narrow bound exciton emission peaks become dominant and occur roughly in the spectral range of 3.35-3.37 eV. As temperature is increased, free exciton emission becomes dominant. Early observations of the bound exciton peaks showed significant variation in number, location, and intensities of the peaks. Thus an effort was put forth to identify the origins of these bound exciton peaks. Reynolds et al. [38] originally named the specific bound exciton peaks I_0 to I_{11}. The peaks I_3 through I_8 are commonly attributed to A-excitons bound to neutral donors [24,41,42]. However, there is disagreement in the literature as to the origin of the peaks I_9 through I_{11}, as they have recently been reported to be related to both acceptor [42] and donor [41] bound excitons.

Meyer et al. [41] attempted to identify the chemical nature of the impurities allowing bound exciton recombination in ZnO. Using magnetic resonance experiments, it was shown that the I_4 peak results from the inclusion of H. Electron nuclear double resonance (ENDOR) experiments were used to detect H in a specimen with a strong I_4 peak. Annealing at 800 °C effectively removed the I_4 peak, and simultaneously removed the H-related ENDOR signal. The peak I_6 was apparent in a specimen with high Al impurities. Similar to the conclusion of Schilling et al. [43], Meyer et al. attributed the I_6 peak to excitons bound to Al impurities.

The peaks I_5 to I_{11} were attributed to neutral acceptor bound excitons by Gutowski et al. [44] using high-density excitation spectroscopy in unison with high magnetic fields. However, the I_8 peak was observed [41] in a specimen that showed severe interdiffusion of Ga. Ko et al. [45] observed the same peak in Ga-doped ZnO specimens, which leads to the conclusion that I_8 is actually caused by recombination from an exciton bound to a neutral Ga donor. Meyer et al. [41] went on to describe I_9 (unintentional In contamination) and I_{10} as donor bound excitons based on the observed binding energies of the two electron satellites of each peak.

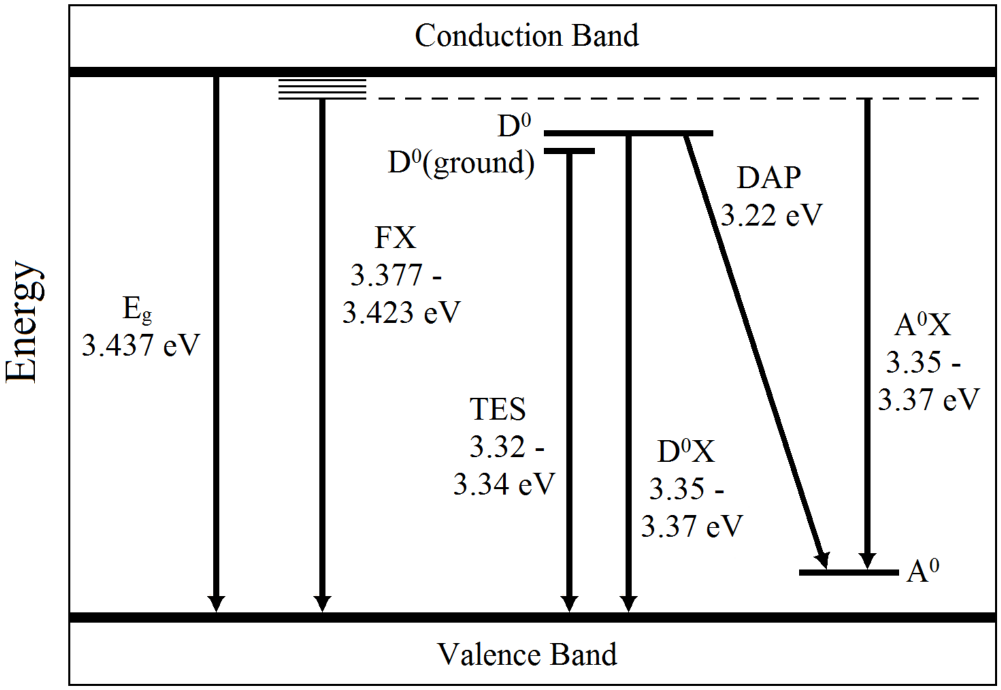

Figure 2.4: Energy level diagram showing the most commonly observed radiative recombination mechanisms of ZnO.

Donor acceptor pair (DAP) transitions are found near 3.22 eV for ZnO. In a DAP transition, an electron bound to a donor recombines with a hole bound to an acceptor [46]. Two electron satellite

(TES) transitions in ZnO are found in the spectral region 3.32-3.34 eV. These are a result of the radiative recombination of excitons that are bound to neutral donors. When recombination occurs, the donor remains in the excited state, which results in the creation of a photon with energy less than the D^0X emission by an amount equal to the difference in the excited and ground states of the donor [24]. Binding energies to the donor can be estimated using the effective-mass approximation, which states that the donor binding energy E_D equals the donor excitation energy difference between the ground and first excited state [24, 47]. This has been used to help identify contaminants and impurities in ZnO, such as that for the I_{10} peak described above. Figure 2.4 shows the energy level diagram for ZnO, depicting the process involved for D^0X, A^0X, DAP, and TES emission.

Another peak is sometimes observed at 3.333 eV. Meyer et al. [41] observed this peak near the range of the TES peaks. However, upon annealing a specimen with this feature, the intensity of the 3.333 eV peak increased by a factor of 100, whereas typical TES peaks are either unaffected or decrease in intensity, depending on the relevant donor. Due to this anomaly, further investigation was needed. Meyer et al. looked at the thermal activation quenching of both the 3.333 eV peak and a neutral donor bound exciton peak, and observed results similar to the Y-lines of ZnSe [48], ZnTe [49, 50], and GaN [51]. A model was proposed that suggested the Y-line originated from localized recombinations at extended defects, such as dislocations or grain boundaries [48]. Meyer et al. utilized spatially resolved cathodoluminescence (CL) spectroscopy to monitor the spatial variation of the peak and found that it was localized and spot-like. Because of the irregularity and localization of the peak, it was determined that the peak was in fact not a TES. Comparing SEM images to the CL data, it was observed that the peak was primarily located at areas of morphological irregularities. It was also observed that this peak was typically absent in high quality specimens with better morphologies. It was thus concluded that the 3.333 eV peak is related to excitons bound to structural defects, or defect bound excitons (DBX).

Analysis of the energy shifting of free and bound exciton emission peaks with temperature in ZnO can help determine various physical parameters and donor species. Typically emission is dominated by neutral donor bound exciton emission at low temperatures, but at higher temperatures free exciton emission dominates. PL of ZnO has been extensively investigated at low temperatures and room temperature, but more recently, a detailed study on the energy shifting of excitonic emission peaks as a function of temperature was reported by Hamby et al. [52]. Peaks from free and bound exciton emission were observed in the PL spectrum of a high quality ZnO single crystal bulk specimen and PL spectra were collected at temperatures ranging from 4.2 K to 300 K. The free exciton FX_A emission peak center as a function of temperature was observed to follow a model by Manoogian and Woolley (MW) [53]:

$$E = E_0 + UT^S + V\theta[\coth(\theta/2T) - 1].$$

The MW model was used because it was an improvement upon the commonly used Varshni equation [54], which failed to account for the case when the temperature range was less than the Debye temperature, θ_D [53]. The MW model has also previously been successfully applied to II-VI semiconductors such as CdTe [55] and CdS [56]. In the MW equation, E_0 represents the energy band gap at absolute zero, UT^S the lattice dilatation, and $V\theta[\coth(\theta/2T) - 1]$ electron-phonon interaction. Hamby et al. [52] also plotted the natural logarithm of the intensity of a neutral donor bound exciton peak at various temperatures against the inverse of the temperature. The thermal activation energy, E_A, was determined as the slope of the linear portion of this plot, which in the case for bulk single crystal ZnO in this study was 14 meV. Wang and Giles [57] also investigated the temperature dependent energy shift of ZnO. The $\mathrm{FX_A}$ peak center was plotted as a function of temperature. Expressions given by Varshni [54] and Cody [58] were used to attempt to fit the temperature dependent behavior of the ZnO free exciton peak. A reasonably good fit was obtained for the free exciton peak, but a poor fit was achieved for the phonon-assisted replica. Better fits for these peaks were achieved by Hamby et al. [52] using the MW model.

Another source of disagreement in the study of ZnO originates from green luminescence (GL), also referred to in the literature as deep-level emission, defect emission, and fluorescence. Early on Kröger and Vink [59] attempted to determine the origin of the GL, along with similar luminescence observed in ZnS and CdS. Expanding on previous models, it was assumed that a cation vacancy was responsible for this luminescence in these semiconductors. By observing the compensation of the resulting charge and backing with some experimental evidence, it was concluded that, for ZnO, the GL arose from Zn vacancies ($\mathrm{V_{Zn}}$) and oxygen vacancies ($\mathrm{V_O}$). A later study showed the GL to be linked to Cu impurities [60]. This Cu-related GL contained some fine structure, but the width was similar to other reports of GL. Liu et al. [61] observed that dry air sintering ZnO results in GL due to excess Zn, forming Zn interstitials ($\mathrm{Zn_i}$). They also observed that water vapor sintering yielded strong green surface emission and weak green and yellow emission. However, Mn, which was determined to be interstitial, quenched both the green and yellow emission, implying that the green and yellow luminescence were resultant of ($\mathrm{Zn_i}$) and ($\mathrm{O_i}$), respectively.

In more recent years, Vanheusden et al. [62] explored the relationship between the GL and free-carrier concentration along with paramagnetic oxygen-vacancy density by analyzing ZnO phosphor powders. Several experimental techniques were utilized and it was observed that the GL had a strong dependence on free-carrier depletion at the surface. It was concluded that the GL appearing from ZnO phosphor powders resulted from recombination of electrons in oxygen vacancies with photoexcited holes in the valence band.

Egelhaaf and Oelkrug [63] looked at ZnO sintered at 1600 K under air, argon, and oxygen at atmospheric pressure. Using diffuse reflection, steady state and time-resolved PL, and photoconductivity, efficient quenching of surface states was revealed. It was concluded that the GL is a result of an oxygen defect center (V_O) and the acceptor is a Zn defect center (V_{Zn}). Kohan et al. [64] used a first-principles pseudopotential method to obtain a similar conclusion: the GL originates from transitions between conduction band electrons and V_{Zn} in the valence band. Similar conclusions were also obtained experimentally by others [65–67]. Using external electric fields, Korsunska et al. [68] showed that GL intensity decreased near the anode but increased near the cathode, and thus concluded that Zn_i also played a role. Lin et al. [69] analyzed the PL of ZnO films deposited on Si substrates in combination with full-potential linear muffin-tin orbital defect level calculations, which yielded the conclusion that the GL arises from oxide antisite defects (O_{Zn}). It is clear that the origin of the GL remains debatable. However, the GL has been abundantly correlated to Zn- and O- related defects. Many studies have attempted to use various techniques to quench the GL, which has been reported to indicate high crystalline quality ZnO. Du et al. [70] embedded ZnO in polymethyl methacrylate (PMMA) in order to quench the GL, which was reported to signify the elimination of surface defects.

2.2.4 Synthesis and Properties of ZnO Films

ZnO films are commonly deposited on sapphire substrates due to its commercial availability and relatively close lattice match, 18% [71], which allows the growth of high quality ZnO films. In the last several years, most studies on ZnO films have focused on 0.25-3 μm thick films deposited on (0001) sapphire, or *c*-plane sapphire. Laser ablation was a common synthesis technique early on, which typically yielded polycrystalline ZnO films of relatively poor quality [72, 73].

Higher quality films have been created using pulsed laser deposition (PLD) [32, 73–77]. In PLD, the target material is placed in a vacuum chamber and a high power pulsed laser beam is focused on the target. This vaporizes the material, which acts to deposit it as a thin film on a substrate. The ability to grow epitaxial ZnO with PLD was reported by Muth et al. [73] in a study that utilized transmission spectroscopy and PL spectroscopy at temperatures down to 77 K. Strong UV emission was observed with low intensity GL, indicating high quality ZnO. Synthesis parameters such as laser power density, vacuum pressure, substrate temperature, and cooling rate play a significant role in the final quality of films created with PLD.

Molecular beam epitaxy (MBE) has also been used to synthesize epitaxial ZnO films [45, 78–81]. Chen et al. [78] observed strong near band-edge emission with minimal GL from 500 nm thick ZnO films synthesized with plasma-assisted MBE. Ko et al. [45] used a GaN buffer layer on the sapphire substrate to reduce the lattice mismatch, but observed few differences from Chen et al. [78] for undoped specimens. Ohtomo et al. [79] utilized laser MBE to create ZnO/$Mg_{0.2}Zn_{0.8}O$ superlattices, thus creating ZnO layers with thicknesses of 1.2-12 nm and entering the realm of quantum confinement.

Another common synthesis technique is radio frequency (rf) magnetron sputtering [82–85]. When deposited on *c*-plane sapphire, *r*-plane sapphire, or (001)GaAs, polycrystalline ZnO films form, but single crystal films have been reported when using (111)GaAs substrates [83]. High quality epitaxial films have also been synthesized using metalorganic chemical vapor deposition on *r*-plane sapphire [86, 87].

With a Bohr radius <5 nm, quantum confinement is difficult to achieve in films of ZnO due to synthesis constraints. The easiest way to achieve thin epitaxial ZnO films is by finding a better substrate lattice match [81] or by creating a superlattice [79]. Limited experimental observations have been reported regarding the excitonic band structure of ZnO thin films. However, variations in the PL of ZnO films have been observed as a function of film thickness, substrate type, synthesis parameters, doping material, and doping concentration and numerous results have been reported.

In two similar studies, epitaxial ZnO thin films of thickness ranging from 40 nm to 3.2 μm were deposited on *c*-plane sapphire using PLD [75, 77]. The crystalline quality and strain state of the films was determined using double-crystal X-ray diffractometry (DCXRD), and the band gap was characterized with room temperature PL. With decreasing film thickness, shifts of nearly 40 meV were observed in the near band-edge (NBE) PL emission peak due to an increase in residual tensile strain. These residual strain effects were observed for film thicknesses up to about 400 nm. The 40 nm thick ZnO specimen had low PL emission intensity, with the GL more intense than the NBE emission. As film thickness was increased, both the GL and NBE emission became more intense, although the NBE emission intensity increased with respect to the GL, up to a ratio of approximately 12:1.

Analysis of the biaxial stress-dependence of the band gap energy of polycrystalline thin films has also been investigated [88, 89]. Polycrystalline thin films were deposited on quartz using reactive rf magnetron sputtering. It was found by side-inclination XRD that the ZnO films were under a biaxial state of residual tensile stress due to both lattice and thermal mismatch. The absorption spectra of specimens in states of stress ranging from about 1.4-2.0 GPa indicated a blue-shift in the ZnO band gap with increasing stress. A fit to experimental data yielded the following equation, which was supported by *ab initio* calculations and suggested that the band gap of ZnO should increase linearly with increasing biaxial stress:

$$E_g = E_{g0} + \delta\sigma_{xx}.$$

In the equation, E_g is the band gap energy in eV, E_{g0} is the stress-free band gap energy of ZnO in eV, δ is the band gap shift due to biaxial strain in eV/GPa, and σ_{xx} is the biaxial stress in GPa. The stress level of the films was calculated to be different depending on which X-ray diffraction peak was being analyzed. When the (213) diffraction peak was used to evaluate stress, E_{g0} and δ were reported to be 3.160 eV and 48 meV/GPa [88]. When the (002) diffraction peak was used, E_{g0} and δ were reported to be 3.171 eV and 27 meV/GPa [89].

In another work [90], ZnO thin films were deposited by a sol-gel process on five different substrates: *c*-plane sapphire, GaN epilayer on *c*-plane sapphire, quartz glass, Si(111)/SiO$_2$, and glass. Residual strains in the thin films were estimated from lattice parameters as determined by XRD. The strain varied by substrate from -0.47% up to +0.1%. Scanning electron microscopy (SEM) and XRD results indicated good orientation of ZnO on the GaN and Si/SiO$_2$ substrates, but poor orientation along the *c*-axis for all others. PL was measured using a 325 nm excitation source. Only the NBE emission was observed on all specimens and a redshift of the NBE peak of up to about 20 meV was reported with increasing compressive strain.

Ong et al. [76] grew ZnO films of various stoichiometry and crystallinity on *c*-plane sapphire by PLD. X-ray diffraction (XRD) measurements were utilized to determine the *c*-axis lattice constant and ω-rocking curve for each ZnO film. The amount of strain in the specimens was determined by comparing the *c*-axis lattice constant of the thin film with that of ZnO powder. The mean crystallite size was estimated using the Scherrer formula, which uses the X-ray wavelength, Bragg diffraction angle, and FWHM of the diffraction peak. The long-range disorder of the films was determined by the FWHM of the ω-rocking curves and indicated relative tilting of grain columns. It was found that as the crystallite size decreased from about 85 nm to 12 nm, the associated strain increased linearly from about 0.2% to 1.5%. The long-range disorder was also found to increase as crystallite size decreased. Thus, for small crystallite sizes, strain and long-range disorder were high. The optical response of the films was measured with spectroscopic ellipsometry. The absorption spectra were deduced from the ellipsometric data for each film. In the absorption spectrum of the specimen with lowest strain (largest crystallite size), a free exciton peak was reported near 3.317 eV and an exciton-photon peak near 3.39 eV. With increased strain (decreased crystallite size), the free exciton peak shifted to a higher energy. At the highest strain, the free exciton peak split into two peaks near 3.2 eV and 3.32 eV, while the exciton-photon peak became very weak. The experimental data obtained from the absorption spectra was then compared to a computed band structure. Reasonable agreement was obtained, but values in calculating the band structure were approximate.

Ashkenov et al. [32] looked at the Raman and IR spectra of high quality ZnO films deposited by PLD on *c*-plane sapphire substrates. XRD and TEM were utilized to characterize the quality of the films, which were approximately 1.4 μm thick. The ZnO phonon mode frequencies observed from the films were consistent with results for bulk ZnO within about 1 cm^{-1} for the E_2^{high} peak. The small shift was explained by the existence of point defect vacancies in the ZnO.

2.3 Doping Semiconductor Materials

Doping semiconductor materials with foreign atoms or molecules can dramatically alter the mechanical and optical response of the material. Proper dopant selection, along with the proper concentration, can be utilized to fine-tune material properties such as conductivity, hardness, and optical band gap. Materials can be changed from *n*-type to *p*-type semiconductors, band gaps can change dramatically, and emission efficiencies can be enhanced greatly.

The doping of semiconductors is very useful in the field of optoelectric devices. In order to fully utilize a semiconductor material, both *n*- and *p*-type doping are necessary. *n*-type doping results in an overall excess of electrons in the material, whereas *p*-type doping results in an overall excess of holes. While *n*-type doping is easily achieved with ZnO, *p*-type doping has been an ongoing challenge. In a first principles study, Park et al. [91] reported that substitutional group-I elements such as Li, Na, and K are shallow acceptors but substitutional group-V elements such as P and As are deep acceptors. Problems with achieving *p*-type doping in ZnO were reported to originate from the formation of interstitials for group-I elements and antisites for group-V elements. ZnO in the wurtzite crystal structure is inherently an *n*-type semiconductor due to the presence of defects such as $\mathrm{V_O}$ and $\mathrm{Zn_i}$ which causes a deviation from stoichiometry [24]. In addition to focusing on altering the charge carrier type in ZnO, researchers have attempted to alter charge carrier concentration and mobility in an effort to increase conductivity. ZnO nanoparticles have also been doped with various elements and investigated by PL spectroscopy, which can give insight to the optical response of ZnO [92, 93].

2.3.1 Doping of ZnO with Group-III Elements

ZnO has been doped with ions of many different group III elements to achieve *n*-type doping, including In^{3+} [94,95], Ga^{3+} [45,95–98], Al^{3+} [43,84,95,99–101], and B^{3+} [95], which substitute for Zn^{2+} and thus introduce an extra electron. Doping of ZnO was initially prompted by the increased use of transparent conductors in opto-electronic devices, creating the need for highly conducting, high transparency semiconductors [94]. Major et al. [94] created In-doped ZnO polycrystalline films using spray pyrolysis and observed high transparency of 85% in the visible spectral range and conductivity of about $8 \times 10^{-4}\ \Omega\,\mathrm{cm}$. XRD revealed a diminished ZnO crystallinity at only 2 at.% In. Carrier concentration was observed to increase with increasing In content up to a saturation point of about $4 \times 10^{20}\ \mathrm{cm}^{-3}$, where it remained constant with further increased In concentration. Mobility initially decreased with increasing In concentration, then quickly increased until saturation at about $15\ \mathrm{cm}^2\,\mathrm{V}^{-1}\,\mathrm{s}^{-1}$. This behavior was described as the result of grain boundary trapping due to the small grain sized polycrystalline films.

Minami et al. [99] observed about a 4-fold decrease in resistivity as compared to the results reported for In doping [94] when doping ZnO with Al. Minami et al. [95] then went on to study the effects of doping ZnO with several group III elements: B, Al, Ga, and In. The powdered oxide form of each element was used as the dopant, and the specimens were created as polycrystalline films using rf magnetron sputtering. The resistivity was observed to decrease with increasing doping concentration, and the lowest resistivity was observed at about 2-3 at.% for Al, Ga, and In and at about 10 at.% for B doping. As a result of the decrease in resistivity, it was suggested that the dopants act as an effective donor in ZnO. High carrier concentration of the Al-, Ga-, and In-doped ZnO was attributed to ions, Al^{3+}, Ga^{3+}, and In^{3+}, substituting at Zn^{2+} sites or from these atoms at intersitial sites. It was also suggested that this could be a result of $\mathrm{V_O}$ or $\mathrm{Z_i}$. The ZnO films doped with B did not show an increase in carrier concentration like the others, although an increase in stability at high temperatures was observed from all dopants.

Schilling et al. [43] observed the PL of Al implanted ZnO in the NBE range at liquid He temperatures. To decipher the effects of damage caused by implanting, Ar implanted specimens were also created and compared. Specimens were created with concentrations ranging from 9×10^{15} to $9 \times 10^{18}\ \mathrm{cm}^{-3}$. Evidence of the $\mathrm{I}_{5/6}$, I_9, and I_{10} bound exciton peaks were observed. The $\mathrm{I}_{5/6}$ neutral donor-bound exciton peak was observed to increase in intensity with increasing doping concentration of Al, whereas it decreased slightly in intensity after doping with Ar, likely a result of recombination from excitons bound to Al related impurities. The trend was demonstrated by plotting the

PL intensity ratio of $I_{5/6}/I_9$ peaks against the implantation concentration, from which a roughly linear trend was observed. Schilling et al. suggested that the Al ions form a polycentric complex in ZnO, rather than a point defect. The strain created by co-doping ZnO films with Al and N has also been investigated using XRD [101]. As Al concentration was increased, the compressive strain in the films increased up to a concentration of 0.4 at.% and then decreased. The eventual decrease in compressive strain was attributed to Al occupying more substitional sites, thus relieving some of the compressive strain.

The first report of epitaxial Ga-doped ZnO films arose in the mid 1990's. Ataev et al. [96] created Ga-doped ZnO films on (1012) sapphire using a CVD technique and characterized the quality using XRD and Hall measurements. Results were in agreement with those of Minami et al. [95] and the high carrier density at high Ga doping concentrations was attributed to Ga^{3+} ions replacing Zn^{2+}, as suggested by Minami et al. Ko et al. [45] observed the PL of epitaxial Ga-doped ZnO films from specimens created by plasma-assisted MBE. PL measurements at 10 K revealed an additional peak within the range of bound exciton emission, which was attributed to the effects of Ga doping. It was also noted that the deep-level emission did not increase with increasing Ga concentrations, implying that Ga doping did not contribute to the defects responsible for this emission. Kato et al. [102] also investigated Ga-doped ZnO films created on *c*-plane sapphire by MBE. It was observed that the activation ratio, estimated by dividing the concentration of carriers by the concentration of Ga, was about unity once Ga content exceeded 3×10^{17} cm^{-3}. This fact was used to suggest that Ga atoms are substituted at the Zn sites, which agrees with the previous suggestions that Ga^{3+} ions substitute for Zn^{2+} ions and act as donors [95].

2.3.2 Transition Metal Doping of Semiconductor Materials

The behavior of ZnO when doped with group III elements has been extensively reported. However, for the purposes of this study, there is an interest in the behavior of ZnO when doped with transition metals, specifically those similar to Re. When CdS is doped with small amounts of Mn a broad yellow emission appears centered near 565 nm, and a peak attributed to a zero phonon line (ZPL) is observed near 537 nm [103]. Ehrlich et al. [104] investigated the effects of a higher range of Mn doping concentrations in CdS and used time resolved spectroscopy to determine differences between emission due to Mn and emission from DAP transitions. The decay rate of the ZPL peak was observed to be exponential with time constant $\tau = 0.65$ ms, whereas the decay rate of DAP transitions would follow a hyperbolic rate with a much faster decay. The ZPL was also observed to split in a magnetic field, which is characteristic of a ZPL. With increased Mn doping concentrations, the ZPL was no longer observed and only the broad yellow emission was observed, with the addition of a peak near 901 nm.

Kanemitsu et al. [105] later studied Mn-doped CdS nanocrystals created by sequential ion implantation into Al_2O_3. Undoped CdS nanocrystals were also created with sequential ion implantation for comparison. Very similar PL spectra at 8 K were observed between the Mn-doped and undoped specimens. However, when the phase between the excitation and emission was varied with a phase shifter built into a lock-in amplifier, a new band was observed near 570 nm for the Mn-doped specimens. This was attributed to the intra-*d*-*d* transition of Mn^{2+} in agreement with previous reports. Mn was implanted into Al_2O_3 to create a new set of specimens, and the 570 nm band was not observed, indicating that this emission was a result of interactions between the Mn and CdS.

An effort to create ferromagnetic semiconductors, or diluted magnetic semiconductors (DMS), has driven researchers to dope II-VI and III-V semiconductors with transition metal ions. This has been possible only in more recent years by enhanced synthesis techniques [106]. In this field, researchers have investigated the physical and optical properties of ZnO when doped with high concentrations of Mn [107–112], Co [108, 109, 111, 113], Cr [108, 109], Ni [109, 111], and Fe [108]. Although ferromagnetism is not the focus of the present study, relevant information such as typical defect type or band gap modification can be acquired from these studies.

Fukumura et al. [107] created DMS out of ZnO films doped with Mn using PLD. The $Zn_{1-x}Mn_xO$ films were created with Mn concentrations up to $x = 0.35$. Using XRD and electron spin resonance measurements, it was suggested that the dopant Mn ions substitute at Zn sites without altering the wurtzite structure significantly, even at Mn concentrations well above the thermal equilibrium limit ($x \approx 0.13$). The ability to achieve this was attributed to the nonequilibrium nature of PLD. As doping concentration increased from $x = 0$ to $x = 0.35$, the band gap was observed to shift from about 3.28 eV to about 3.75 eV as determined by optical transmittance spectroscopy.

In a related study, Jin et al. [108] investigated the effects of doping ZnO with a wide range of transition metals. As determined by XRD, the ZnO doping solubility limits for Sc, Ti, V, Cr, Mn, Fe, Co, Ni, and Cu were found to range from close to 0 mol % (Cu) to about 20 mol % (Mn), with Co showing the next highest at about 16 mol %. Below these solubility limits, the ZnO wurtzite structure is not significantly altered but the lattice constants increase linearly with increasing doping concentration as dopant ions occupy Zn sites. Beyond this threshold, the formation of precipitated phases occurs such as Cr_2O_3, $ZnMn_2O_4$, Fe_2O_3, and CoO when doping with Cr, Mn, Fe, and Co, respectively. Similar observations were made by others for the doping of ZnO with various transition metals [107, 109, 111, 113]. Using CL spectroscopy, Jin et al. [108] reported that Mn quenched the luminescence of ZnO at 3.25 eV, whereas the addition of Cr created new peaks at 2.97 and 3.71 eV. Less substantial changes were reported in the CL spectra after doping with Fe or Cr.

Ngom et al. [114, 115] created W-doped ZnO nanorods using PLD at W concentrations of 1 and 2 wt. %. It was observed that the addition of W affected the orientation of the nanorods. Room temperature PL spectroscopy revealed several additional peaks throughout the spectrum, which were attributed to various defects caused by W doping. Gao et al. [93] created Y-doped nanoparticles using a sol-gel method and investigated Y doping effects using XRD, SEM, PL spectroscopy, Raman spectroscopy, and X-ray photoelectron spectroscopy (XPS). Two types of ZnO nanoparticle specimens were created in this study: undoped and 5 at. % Y-doped. XRD revealed an increased lattice constant for the Y-doped specimen, suggesting that the Y^{3+} partially substitutes at Zn^{2+} sites. The Raman spectra revealed a blue-shift in the E_2^{high} mode from 434 to 431 cm^{-1}, which was attributed to a decrease in compressive stress or increase in tensile stress as a result of the lattice mismatch originating from the addition of Y. Room temperature PL revealed an increase in the intensity of the NBE emission of Y-doped ZnO as compared to undoped ZnO by a factor of 300. XPS results suggested that Y^{3+} substituting for Zn^{2+} can reduce V_{Zn}, which could explain the relative decrease in GL and increase in NBE emission.

The effects on the Raman spectrum of ZnO after doping with various elements has been the subject of multiple studies. Jeong et al. [34] created wafers of (0001) ZnO which were implanted with As ions to a fluence of 1×10^{15} cm^{-2}. After implantation, some of the specimens were annealed at temperatures between 700 and 900 °C for 1 h in an oxygen atmosphere. Raman spectroscopy was performed on all specimens at room temperature before and after As-implantation. After implantation, the E_2^{high} peak shifted 0.55 cm^{-1} to a lower wavenumber and the FWHM increased by 0.7 cm^{-1}. After annealing for each temperature, this peak shifted back near its original location before implantation, and the FWHM decreased 0.4 cm^{-1} as compared to the implanted specimen.

Bundesmann et al. [116] investigated the Raman spectrum of ZnO doped with Fe, Sb, Al, Ga, and Li grown on *c*-plane sapphire using PLD in a N-free environment. An additional Raman mode for Fe-, Sb-, Al-, and Ga-doped specimens was observed near 277 cm^{-1}, which was attributed to host lattice defects, as this mode was also observed for N-doped ZnO. The Li-doped specimens exhibited no additional Raman peaks even at concentrations up to 17 mol %. This lack of additional modes was attributed to higher film quality as compared to the other specimens, or possibly to the screening of defect complexes by the high mobility Li ions.

2.4 Properties of Rhenium

Rhenium found its way into the scientific community late in the 1920's as the availability increased and costs decreased by a factor greater than 3,000 in a matter of 2 years [117]. Re has atomic number 75 and a silvery-white appearance as a metal.

2.4.1 Physical and Electrical Properties of Rhenium

Various physical and electrical properties of Re at room temperature are shown in Table 2.3. Re has several oxides, initially referred to as white oxide (Re_2O_8), yellow oxide (Re_3O_7), red oxide (ReO_3), blue oxide (Re_3O_8), and black oxide (ReO_2) [118]. ReO_2 has an orthorhombic structure, space group *Pbcn*, with lattice constants $a = 0.4808$, $b = 0.5643$, and $c = 0.4600$ Å [119]. ReO_2 has an activation energy of 49 kJ g at^{-1} and an electrical conductivity of $7.4 \times 10^2\ \Omega^{-1}\,\text{m}^{-1}$ [120]. Re(I) complexes of ligands have been observed to have enhanced photoluminescence compared to those without Re [121]. Wang et al. [122] created 800 nm diameter composite fibers containing $Re(CO)_3(Bphen)Br$ by electrospinning and observed strong photoluminescence and high stability.

Table 2.3: Metallic Re properties at 300 K.

Property	**Symbol**	**Value**	**Units**	**Reference**
Density	ρ	21.03	g cm^{-3}	[123]
Debye Temperature	θ_D	449.3	K	[123]
Energy Gap	E_g	8.7	eV	[124]
Electrical Resistivity	ρ	1.88×10^{-7}	$\Omega\,\text{m}$	[125]
Thermal Expansion	α	1.0×10^{-5}	K^{-1}	[126]
Poisson Ratio	ν	0.29		[127]
Bulk Modulus	B_T	3.00×10^2	GPa	[128]

2.4.2 Doping Material Systems with Rhenium

A limited number of studies have investigated the effects of doping semiconductors with Re. The effects of doping ZnO with Re have not been investigated to date. Nanocrystalline ZnO films have been grown on Re substrates using PLD, however the focus was primarily morphological, and optical studies were not conducted [129]. Theoretical investigations have indicated that in Re-doped

Si clusters ReSi_n, Re should occupy surface sites for n = 1-7, but should occupy a center site for n = 8-12 [130].

Andreev et al. [131] investigated the effects of doping $\mathrm{In}_{0.53}\mathrm{Ga}_{0.47}\mathrm{As}$ with Re. The InGaAs was grown using liquid phase epitaxy on InP substrates, and Re was introduced to the molten solution prior to deposition. The Re-doped films demonstrated n-type conductivity and an order of magnitude increase in the free electron density was observed in the doped films when grown on (111)A InP (topmost layer In) substrates. Mobility was also observed to increase for Re-doped specimens by a factor of about 1.6. PL measurements were performed at specimen temperatures of 1.6, 77, and 300 K in a backscattering geometry. Peak widths were comparable between doped and undoped specimens, attributed to high structural order in the doped specimens. PL intensity was observed to increase an order of magnitude after Re doping. Re doping of specimens grown on (111)B InP (topmost layer P) acted to quench an impurity band, resulting in an edge band. Andreev et al. suggested that deep local levels were not created by the Re atoms in InGaAs as some may think, but the modification to the properties of InGaAs was a result of chemical activity during crystallization of the films.

A similar study was soon thereafter reported in which GaAs films were doped with Re [132]. Liquid phase epitaxy was used to grow GaAs films of thickness less than 5 μm on n-type and p-type GaAs substrates. Some films were doped with Re at concentrations in the range $0.002 - 0.005$ wt.%. As was the case for InGaAs, n-type conductivity was observed for the GaAs films. A decrease in density of free carriers was reported but an increase in mobility was observed after doping with Re. PL spectroscopy revealed no deep radiative recombination centers associated with Re, and Re-doped specimens showed enhanced free exciton emission. The changes of the properties of GaAs were attributed to chemical activity when Re was introduced to GaAs in the liquid state. No suggestions as to the type of point defect created by Re were given.

Agarwal et al. [133] investigated the effects of doping MoSe_2 with Re. Bulk single crystal specimens of $\mathrm{Mo}_{0.995}\mathrm{Re}_{0.005}\mathrm{Se}_2$ were created using a direct vapor transport method. Few differences were observed in the doped specimens, although a slight expansion of the c parameter was seen and carrier concentration increased. Later Vora et al. [134] conducted a similar study in which direct vapor transport was utilized to grow $\mathrm{MoRe}_{0.005}\mathrm{Se}_{1.995}$ single crystals. A slight increase in the c parameter with little change to the a parameter after Re doping suggested that Re was introduced between layers. In addition to changed lattice size parameters, a remarkable decrease was observed in room temperature resistivity, along with an increase in mobility and carrier concentration. UV-VIS-NIR spectrometry revealed that Re doping decreased the direct band gap slightly. The Re-doped specimen also exhibited p-type conductivity as indicated by Hall measurements.

Small doping concentrations of Re (0.2 wt. %) were not observed to significantly affect the absorption spectrum of $Bi_{12}SiO_{20}$ (BSO) crystals [135]. The near band-edge transitions of WS_2 were investigated by Yen et al. [136] with piezoreflectance for both undoped and Re-doped (0.1-0.2 wt. % Re) specimens. This small amount of Re caused red shifts in the A and B free exciton transitions and impurity scattering was observed to increase. After doping TiO_2 with concentrations of Re up to 6 wt. %, Zhang et al. [137] observed increased photocatalytic performance as compared to undoped specimens.

Larger Re doping concentrations were pursued by Reder et al. [138] by synthesizing specimens of $Hg_{1-x}Re_xBa_2Ca_2Cu_3O_8$ with x as large as 0.30. A maximum Re solubility for this material system was found to be $x = 0.15$. The maximum solubility was described to be a result of the Re causing variation of grain connectivity.

Leem et al. [139] investigated the effects of doping the hole transporting layer (HTL) of N, N'-diphenyl-N, N'-bis (1,1′-biphenyl)-4,4′-diamin (NPB) with ReO_3 at concentrations ranging from 0 to 25 wt. %. Specimens were grown on indium tin oxide (ITO) substrates using thermal deposition to create organic light-emitting diodes (OLEDs). UV-Vis absorption spectroscopy suggested that Re doping formed charge transfer complexes in the NPB. After Re doping, driving voltage decreased from about 7.1 V to about 5.3 V and power efficiency increased from 2.0 lm/W to about 2.3 lm/W. The increased efficiency after Re doping was described to be a result of the creation of free holes in the HTL.

In summary, the crystalline quality of ZnO films can be evaluated using Raman spectroscopy. As described in Section 2.2.2, the spectral shift of the Raman peaks has been shown to indicate the amount of residual stress in semiconductor films [7, 34, 35]. A review of the PL spectrum of ZnO was given in Section 2.2.3. High crystalline quality ZnO exhibits characteristic PL emission resulting from free excitons and excitons bound to neutral donors or acceptors. Analysis of the bound exciton peaks can be used to identify types of defects or certain doping species. TES and DAP peaks are commonly observed and can be used as indication of whether excitons are bound to neutral donors or acceptors. DBX emission has been reported as a result of excitons bound to structural defects. Temperature dependent behavior of free exciton PL peaks can be used to estimate lattice dilatation and electron-phonon interaction using the MW model. The localization energy of bound excitons can be estimated using the temperature dependent behavior of the D^0X peak. ZnO has been doped with many group III and transition metal ions, as reviewed in Sections 2.3.1 and 2.3.2. A decrease in resistivity was reported as a result of doping ZnO with Al, Ga, and In up to a certain concentration threshold, after which resistivity increased [95]. The decrease in resistivity was attributed to the doped ions substituting at Zn sites. Solubility limits were reported for Sc, Ti, V, Cr, Mn, Fe, Co, Ni, and Cu in ZnO [108]. At doping concentrations below solubility limits, doping ions were reported to substitute at Zn sites. At doping concentrations above solubility limits, precipitated oxide phases were reported for each. Few studies have investigated the effects of doping semiconductors with Re, and the properties of Re-doped ZnO have not been reported. Re doping was reported to increase the free electron density and mobility of InGaAs, while crystal structure order was maintained [131]. Decreased free electron density, increased mobility, and increased PL emission intensity were observed for GaAs after doping with Re [132]. In $Hg_{1-x}Re_xBa_2Ca_2Cu_3O_8$, a maximum Re solubility of $x = 0.15$ was reported. Based on the reported behavior of ZnO when doped with group III and transition metal ions, a maximum solubility limit of Re in ZnO is expected. XRD can be used to identify precipitated phases at doping concentrations greater than the solubility limit. Raman spectroscopy and PL spectroscopy can be used to characterize the optical behavior of the Re-doped ZnO films and can give insight to residual stress levels, crystalline quality, lattice dilatation, and electron-phonon interaction.

Chapter 3

Experimental Approach

The objective of the present study, as previously described, was to investigate the effects of doping ZnO thin films with Re. ZnO was doped with ReO_2 at concentrations ranging from 0 to 50 wt.%, which was then used to create films of nominal thickness 100 nm on *c*-plane (0001) and *r*-plane $(1\bar{1}02)$ sapphire. The films were characterized by X-Ray diffraction (XRD), photoluminescence (PL) spectroscopy, and Raman spectroscopy.

3.1 Synthesis of ReO_2-Doped ZnO Films

ReO_2-doped ZnO specimens were created at Los Alamos National Laboratory. The ZnO specimens were deposited on either *c*-plane (0001) or *r*-plane $(1\bar{1}02)$ sapphire substrates using pulsed laser deposition (PLD). A background on PLD and other film synthesis techniques was given in Section 2.2.4. For each of the two substrates used, both undoped as well as ReO_2-doped ZnO specimens were created with concentrations of 5, 10, 20, and 50 wt.%.

Specimens were created with a KrF excimer laser (248 nm wavelength) at 2 Hz in a chamber with an initial maximum pressure of 1×10^{-5} Torr. Substrates were brought to a temperature of $650\,^{\circ}C$ during deposition and an oxygen pressure of 350 mTorr was used. The thermal coefficients of expansion of ZnO were listed in Section 2.2 as 6.4×10^{-6} K^{-1} along [1000] and 4.3×10^{-6} K^{-1} along [0001] [23]. Al_2O_3 has thermal coefficients of expansion of 4.78×10^{-6} K^{-1} along [1000] and 5.31×10^{-6} K^{-1} along [0001] [140], resulting in anisotropic thermal expansion for the *r*-plane of sapphire. Specimens were deposited with a target incidence angle of 45 degrees with a target to substrate distance of about 5 cm. The undoped and ReO_2-doped ZnO specimens were created with a nominal thickness of 100 nm. Specimens were cooled after deposition at a rate of about $15\,^{\circ}C\,min^{-1}$.

Proper film oxygenation was achieved during cooling using an oxygen pressure of 250 Torr.

3.2 Instrumentation

3.2.1 Photoluminescence Setup

Two systems were used in this study to characterize the optical response of the Re-doped ZnO films. The first system was used to analyze PL at temperatures ranging from 4.2 K (using liquid He) to 300 K. Specimens were analyzed in a cryostat with an initial maximum pressure of 2×10^{-5} Torr. Temperatures were lowered using liquid He flow. Intermediate temperatures were maintained by varying the flow of liquid He and using a proportional-integral-derivative (PID) controlled heater. Light from a Kimmon IK3151R-E HeCd laser (325 nm wavelength, 3.82 eV) rated at 17 mW was used to excite PL, with a power intensity at the specimen of about 50-66% of the maximum rated power. Incident light was directed to the specimens at a low grazing angle, which lowered the power density and increased the film sampling volume. Emitted light was dispersed by a 0.5 m monochromator utilizing a 2400 g/mm grating (Spex 500M) and detected with a LN_2-cooled charge-coupled device (CCD) camera (SpectrumOne Model: CCD-1024X128-BIUV-1LS). This resulted in a spectral resolution of about 0.5 meV at 3.37 eV. The monochromator was calibrated prior to use by centering the Hg emission peaks from a Hg lamp using the system computer. The computer was used to select the position of the grating and spectral scans were done to collect spectra ranging from 345 nm to 625 nm, or about 2.0 eV to 3.6 eV. The computer was also used to control the shutter on the monochromator. For each measurement taken, an extra measurement was taken with the shutter closed, and this background signal was subtracted from each collected spectrum to eliminate ambient noise in the system.

For the measurements taken in this study, 1 s integration times were used. This was done to achieve consistency in the measurements of specimens with strong emission and weak emission. Specimens with strong emission must have a reduced integration time to avoid flooding and potentially damaging the CCD camera. Conversely, specimens with weak PL emission require longer integration times to achieve a large enough signal to noise ratio. For the specimens used in this study and this experimental setup, the 1 s integration time allowed the best balance between the two.

3.2.2 Confocal PL and Raman System

The second system used in this study was a commercially available confocal microscope setup (WITec, GmbH). This system was utilized for confocal room temperature photoluminescence (PL) spectroscopy and confocal Raman spectroscopy. This system combines a high resolution confocal optical microscope, a spectrometer, and a scanning near-field optical microscope (SNOM). PL was excited with 325 nm (3.82 eV) wavelength light from a HeCd laser and Raman scattering was probed with 532 nm (2.33 eV) wavelength light from a frequency doubled Nd:YAG laser. The emitted or scattered light was directed in a backscattering configuration to an optical fiber, which acted as the confocal pinhole. Light was then dispersed with a 0.3 m monochromator through either a 150 g/mm, 600 g/mm, or 1800 g/mm grating and detected with a thermoelectrically cooled CCD camera. For 532 nm wavelength light, the 150 g/mm, 600 g/mm, and 1800 g/mm gratings resulted in a spectral resolution of about 20.4 cm^{-1}, 5.1 cm^{-1}, and 1.7 cm^{-1} (0.578 nm, 0.144 nm, and 0.048 nm), respectively. Specimens were placed on a piezoelectrically controlled three-axis stage, allowing both area scans and depth-resolved measurements. A schematic of the complete beam path can be seen in Fig. 3.1. More details on the components of this system are described in the following sections.

Laser

Several continuous wave (cw) excitation sources were used in conjunction with the confocal spectroscopy system. The same Kimmon IK3151R-E HeCd laser from the PL setup was primarily used for PL excitation at 325 nm (3.82 eV). The 532 nm (2.33 eV) line of a frequency doubled Nd:YAG laser was primarily used for Raman measurements. The maximum fiber output power from the Nd:YAG laser was approximately 50 mW. The 488 nm and 514.5 nm lines of a Beamlok 2065-7S Ar ion laser from Spectra-Physics were also used for Raman and PL measurements. An optical fiber output power of about 2 mW and 10 mW were achieved for the 488 nm and 514.5 nm lines, respectively. The Ar ion laser was cooled by a closed-loop water heat exchanger.

Optical Fibers/Confocal Pin-hole

Optical fibers were utilized to direct the beam from the laser output to the microscope; different fibers from OZ Optics Limited were used depending on the laser. For the 532 nm line of the Nd:YAG laser and the 488 nm line of the Ar ion laser, a 3.5 μm core diameter pure fused silica core high power polarization maintaining patch cord was used. This fiber was optimized for 488 nm wavelength light and was not able to transmit UV light efficiently. Therefore, for the 325 nm line of the HeCd laser,

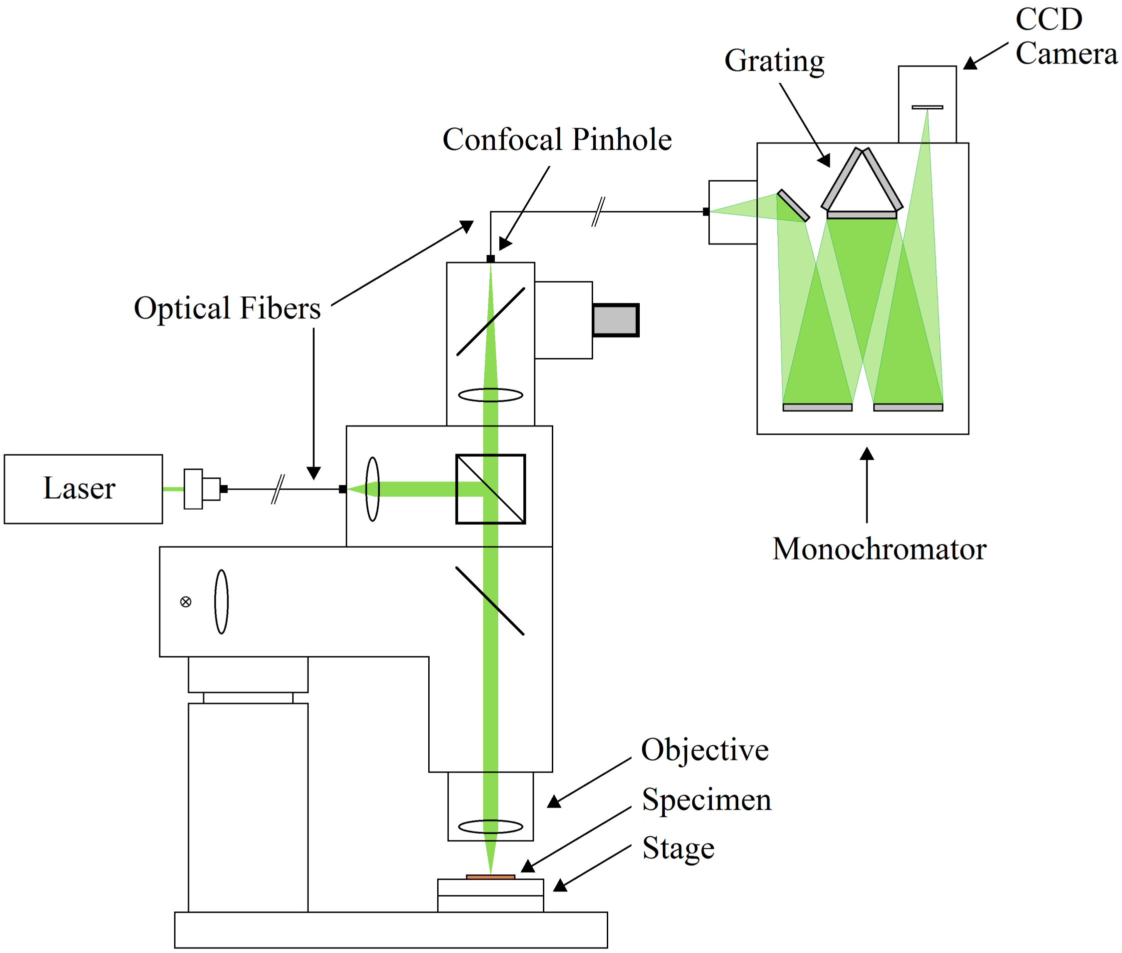

Figure 3.1: Schematic of the beam path for the WITec, GmbH confocal system.

a UV high power single mode fiber with 2 μm diameter core was used. Maintaining polarization of the incident light was not crucial for the PL experiments in this study.

An optical fiber was also used to simultaneously act as a confocal pinhole and to direct the emitted or scattered light to the monochromator. For this application, a high power multi-mode IR-visible (400-2000 nm) fiber with core diameter of either 100, 50, or 25 μm, depending on the desired pinhole size, was used. Decreasing the core diameter of the fiber, and thus decreasing the pinhole size, caused an increase in depth resolution but a decrease in light throughput.

Microscope

Standard microscope objectives were utilized both to obtain optical images of specimens and to focus laser light onto the surfaces and then subsequently recollect scattered or emitted light. Focusing the laser light with the microscope objectives allowed a simple method to maximize the laser power density. For visible light, either a 10X 0.25NA Nikon objective or a 100X 0.9NA Nikon objective were used. When analyzing UV light, either a 10X UV objective or a 52X mirror objective were utilized.

Monochromator

A 0.3 m spectrometer was used in conjunction with the confocal microscope system. Three gratings were available depending on the desired spectral range and resolution: 1800, 600, and 150 g/mm, which allowed a spectral resolution of 0.5, 1.0, and 2.0 cm^{-1}, respectively. The three gratings were selected using the computer system of the setup. A thermo-electrically cooled CCD was used to detect the dispersed light, which was then analyzed on the computer.

Stage

The system utilized a piezoelectrically driven three-axis flexure stage on which fine spatial adjustments could be made to specimens while under the microscope. This enabled the ability to perform depth scans up to 20 μm below a surface and area scans up to 100 × 100 μm. The spatial resolution was controlled by selecting the number of points per scan. The spot size using the 10X 0.25NA Nikon objective was $\sim$1 μm, so the lateral scan resolution was typically set near this value.

Chapter 4

Results and Discussion

This chapter presents the results obtained from the investigation of the effects of doping ZnO thin films deposited on sapphire with various concentrations of ReO_2. In the first section, the experimental results obtained from undoped ZnO films deposited on c- and r-plane sapphire are presented and compared to bulk single crystal ZnO. These results show that the ZnO films used in this study exhibit high crystalline quality with minimal defects and the results are used as a baseline for Re-doped specimens. The next section presents the results obtained from Re-doped specimens, which are compared to the results of the undoped specimens. Finally, a plausible explanation of the behavior observed for Re-doped ZnO is presented.

4.1 Undoped ZnO Films

In this study, the effects of doping Re into ZnO thin films was investigated. Prior to presenting the behavior of the Re-doped ZnO films, the results of the undoped ZnO films are described. In this section, the behavior of the undoped films is described and compared to results of bulk ZnO and similar studies found in the literature.

4.1.1 X-ray Diffraction of Undoped ZnO Films

X-ray diffraction (XRD) was performed at Los Alamos National Laboratory. XRD results were utilized to characterize the crystallinity of the as-grown films. Undoped ZnO specimens deposited on c-plane sapphire showed strong (0002)ZnO and (0002)Al_2O_3 peaks. This indicates that the preferred growth direction was with the c axis perpendicular to the substrate surface. Specimens of ZnO deposited on r-plane sapphire substrates exhibited $(11\bar{2}0)$ZnO and $(02\bar{2}4)$$Al_2O_3$ peaks. This indicates that these specimens had a preferred growth direction with the c axis parallel to the substrate surface, consistent with other reports of ZnO grown on r-plane sapphire [83, 141].

4.1.2 Raman Spectroscopy of Undoped ZnO Films

Confocal Raman measurements were carried out in a backscattering configuration using the commercial microscope setup (WITec, GmbH) described in Section 3.2.2. The 532 nm wavelength line of a frequency doubled Nd:YAG laser was used for the Raman experiments. Scattered light was collected with a 0.3 m monochromator and dispersed with a 1800 g/mm grating. A single crystal bulk ZnO specimen was also investigated for comparison. Typical Raman spectra of the undoped ZnO film deposited on c-plane sapphire and the bulk ZnO specimen are shown in Fig. 4.1. Peak center, full width at half maximum (FWHM), and intensity of all resolvable peaks were determined using Gaussian peak fits. There are six Raman active vibration modes in ZnO as first reported by Damen et al. [31]: E_2^{low} at 101 cm^{-1}, A_1 (TO) at 380 cm^{-1}, E_1 (TO) at 407 cm^{-1}, E_2^{high} at 437 cm^{-1}, A_1 (LO) at 574 cm^{-1}, and E_1 (LO) at 583 cm^{-1}. The Raman spectrum of ZnO was more extensively described in Section 2.2.2.

For bulk single crystal ZnO a well-resolved E_2^{high} mode was observed. Less intense E_1 (TO) and E_1 (LO) peaks were detected for bulk ZnO as well as several peaks arising from multiple phonon processes. The E_2^{low} and A_1 peaks were not observed. The experimental setup used incident light polarized in the x-direction with propagation occurring in the z-direction, and the collected light was not selectively filtered for polarization. As described in Section 2.2.2, the A_1 peak is polarized parallel to the z-axis and therefore should have weak intensity in the Raman spectrum when propagated in the z-direction. Likewise, the E_1 (TO) peak is polarized in the xy-plane and should not be intense in z-direction propagation. Additionally, Damen et al. [31] observed an intense E_2^{high} peak from bulk single crystal ZnO when scattered light was collected in the z-direction and no other peaks were clearly observed.

For the ZnO film deposited on c-plane sapphire, an intense peak from the E_2^{high} mode was observed. This was the only ZnO related peak observed from the ZnO film. Ashkenov et al. [32] also observed an intense E_2^{high} peak from ZnO films deposited on sapphire substrates with little evidence of any other ZnO related peaks when incident and collected light were parallel to the z-axis. For the backscattering configuration used in this study, the primary observation of the E_2^{high} peak was expected.

Additional peaks were observed in the Raman spectrum of the ZnO film specimen at 381.2 cm^{-1},

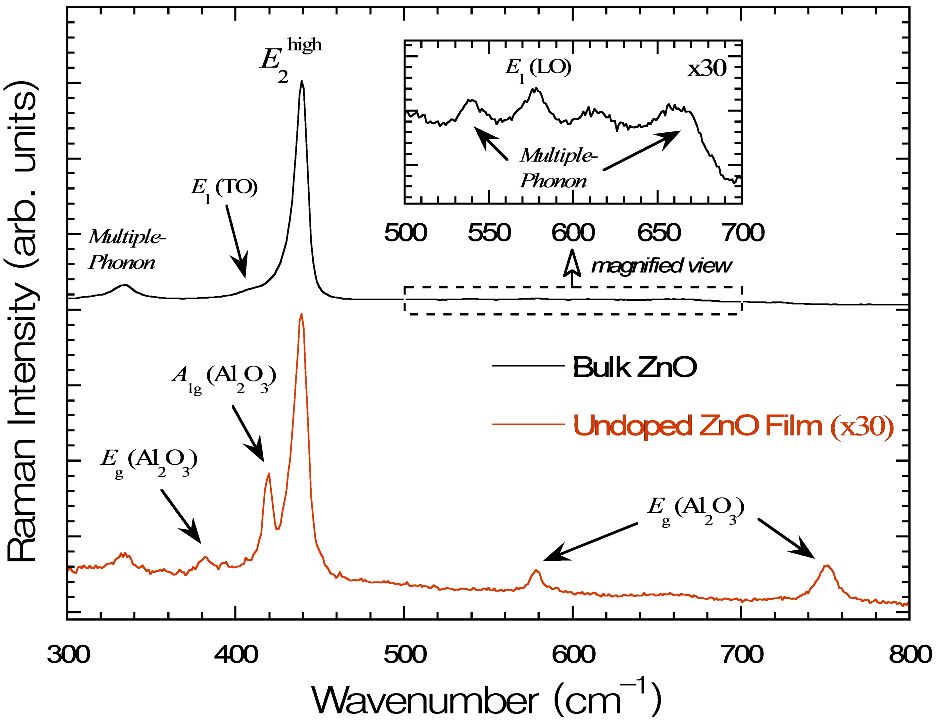

Figure 4.1: Raman spectra of bulk ZnO and undoped ZnO film deposited on *c*-plane sapphire. ZnO Raman modes are indicated on the bulk ZnO spectrum, and sapphire Raman modes are indicated on the ZnO film spectrum. The ZnO film spectrum is scaled in intensity, and the spectra are offset for clarity.

419.1 cm^{-1}, 578.0 cm^{-1}, and 751.0 cm^{-1}. Ashkenov et al. [32] attributed peaks at the same spectral locations to Raman active modes of Al_2O_3 in a study of the Raman spectrum of ZnO films deposited on sapphire substrates. Krishnan [142] reported Al_2O_3 to have seven Raman active modes: five E_g modes and two A_{1g} modes. Porto et al. [143] reported these Al_2O_3 Raman peaks at 378 cm^{-1}, 418 cm^{-1}, 578 cm^{-1}, and 751 cm^{-1}. Therefore, the additional peaks are attributed to Al_2O_3 Raman active modes of the sapphire substrate. Table 4.1 summarizes all of the Raman active modes of ZnO and Al_2O_3 reported in the literature, as well as the observed peak centers for the bulk ZnO specimen and the undoped ZnO films deposited on *c*-plane sapphire in this study. The observed phonon mode frequencies of the E_2^{high} peak for the bulk ZnO specimen and the ZnO film deposited on *c*-plane sapphire agree well with reported values [31] as seen in Table 4.1. The observed E_2^{high} peak center of the bulk ZnO specimen and the undoped ZnO film also agree well with each other, which suggests that small amounts of strain are present in the ZnO film. Table 4.1 shows that the other observed ZnO and Al_2O_3 mode frequencies also agree with reported values [31, 143].

Table 4.1: Raman peak symmetries and frequencies observed for the undoped ZnO film deposited on c-plane sapphire. Cells marked with '—' indicate the mode was not clearly observed.

Material	**Mode**	**Bulk ZnO Observed Center ($\mathbf{cm^{-1}}$)**	**Undoped ZnO Film Observed Center ($\mathbf{cm^{-1}}$)**	**Reported Peak Center ($\mathbf{cm^{-1}}$)**
ZnO	E_2^{low}	—	—	101 [31]
	A_1(TO)	—	—	380 [31]
	E_1(TO)	411.7	—	407 [31]
	E_2^{high}	439.0	438.7	437 [31]
	A_1(LO)	—	—	574 [31]
	E_1(LO)	579.0	—	583 [31]
Al_2O_3	E_g	—	381.2	378 [143]
	A_{1g}	—	419.1	418 [143]
	E_g	—	—	432 [143]
	E_g	—	—	451 [143]
	E_g	—	578.0	578 [143]
	A_{1g}	—	—	645 [143]
	E_g	—	751.0	751 [143]

The A_1 (TO) and A_1 (LO) modes were not observed in the Raman spectra of the undoped ZnO films for the same reasons described above for bulk ZnO. The E_1 (TO) and E_1 (LO) peaks were not observed in the Raman spectra of the undoped ZnO films for two reasons. First, a low laser power density was utilized in these experiments to avoid altering or damaging the specimens with heat. This resulted in a spectrum with a lower signal to noise ratio, which made it difficult to resolve low intensity peaks. Second, the Al_2O_3 A_{1g} mode at 419 cm^{-1} was in the same spectral region as the ZnO E_1 (TO) peak and the Al_2O_3 E_g mode at 578 cm^{-1} was near the ZnO E_1 (LO) mode thus making it difficult to resolve these low intensity ZnO modes.

The intensity of light below a surface follows the Beer-Lambert-Bouguer law, $I(z)/I_0 = e^{-\alpha z}$, where z is the depth below the surface and α is the absorption coefficient of the material at the wavelength of the probing light. For 532 nm wavelength light, the absorption coefficients of ZnO and Al_2O_3 are $\sim$5000 cm^{-1} [144] and $\sim$0.0007 cm^{-1} [145], respectively. The probing depth is estimated to be the depth below the surface at which 63.2% of light is absorbed by the material ($I/I_0 = 1/e$), which gives a probing depth of $1/\alpha$ [146]. For a backscattering configuration, both incident and propagated light travel through the material, so the probing depth is $1/2\alpha$ [147]. This gives probing depths of about 10 μm and 6.7 m for ZnO and Al_2O_3, respectively. A 100 μm optical fiber was used in this study as the pinhole of the confocal microscope. Harriman [147] reported the depth resolution of the experimental setup used in this study using the 100 μm fiber to be 1.21 μm. Therefore, the actual probing depth was determined by the depth resolution of the confocal microscope, 1.21 μm. When focused on the surface of a 100 nm thick film, up to 90% of the probing volume is located in the substrate. The Raman spectra were collected from a small sampling volume of ZnO relative to the Al_2O_3 substrates, and therefore Raman peaks originating from the Al_2O_3 substrate were more intense than the low intensity ZnO Raman peaks.

The E_2^{high} peak was observed to be well resolved and consistent with the literature. The E_2^{high} peak has also been extensively studied [33] and was used for comparisons between different specimens in this study because it was the only ZnO peak observed from the thin film specimens. Decremps et al. [33] investigated the ZnO Raman peak shifting with pressure and reported the A_1 (TO), E_1 (TO), E_2^{high}, and E_1 (LO) peaks to shift about 5 cm^{-1}/GPa and the E_2^{low} peak to shift about -1 cm^{-1}/GPa. Wermelinger et al. [35] investigated the stress field around a Vickers microindentation as indicated by Raman peak shifting and observed the same spectral shifting behavior of the A_1 (TO), E_1 (TO), and E_2^{high} peaks. Therefore, the E_2^{high} peak should be representative of the other Raman peaks for the purposes of this study.

Figure 4.2 shows the Raman spectra of undoped ZnO films deposited on *c*-plane sapphire and *r*-plane sapphire. The *r*-plane sapphire substrate specimen exhibited the same peaks as the *c*-plane sapphire substrate specimen: the ZnO E_2^{high} peak and four Al_2O_3 peaks. Sparks and Paesler [7] utilized Raman peak spectral shifting to quantify the residual stress of milled Ge and Si using the hydrostatic stress dependence of the Raman peaks. For the case of milled Ge and Si, the stress state was likely close to hydrostatic. Although further investigation would be required to definitively characterize the state of stress of the ZnO films analyzed in this study, a biaxial state of stress is expected. The spectral shift of the ZnO E_2^{high} peak as a function of in-plane strain was recently reported by Liu et al. [148] to be about -6.67 cm^{-1}/%. The peak center of the E_2^{high} peak for the film deposited on *r*-plane sapphire shifted 1.3 cm^{-1} to a higher wavenumber, which correlates to increased residual compressive in-plane strain of about 0.2 % using the reported spectral shift of the

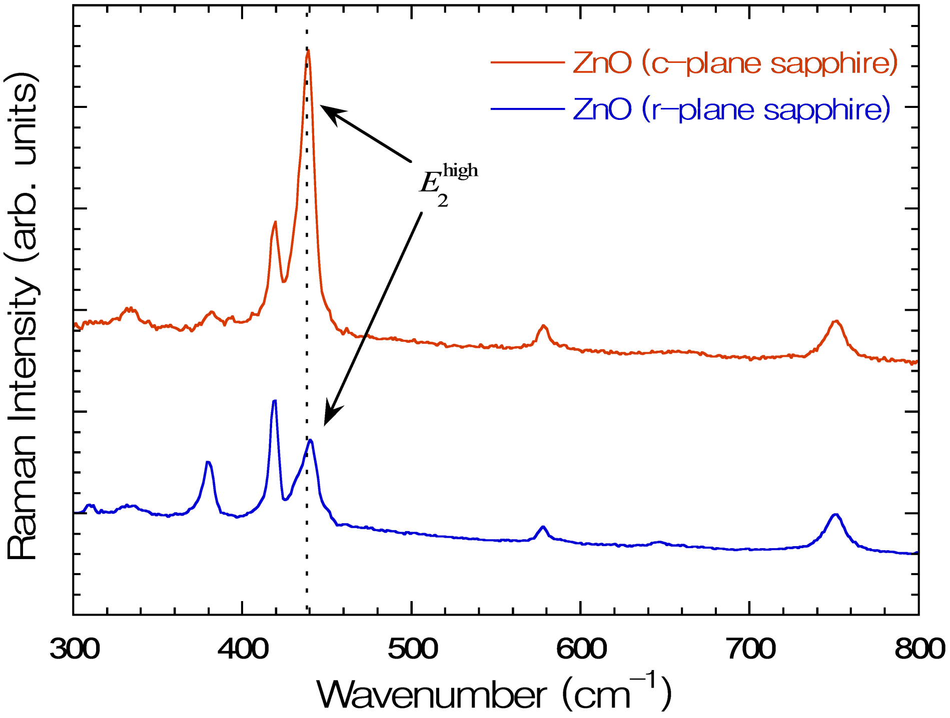

Figure 4.2: Raman spectra of ZnO films deposited on *c*-plane and *r*-plane sapphire. Plots are on the same intensity scale, but have been offset for clarity.

E_2^{high} peak with strain. In Section 3.2.2, the spectral resolution of the setup used was reported to be 1.7 cm^{-1}, which indicates the ability to resolve multiple peaks from one another. Typically peak center identification accuracy for a single peak is reported to be 3 or 4 times better than the spectral resolution of the instrument [149, 150], in this case about 0.5 cm^{-1}. The residual strain of ZnO grown on *c*-plane sapphire results from a lattice mismatch of 18% and thermal expansion coefficient of -2.4% [83]. For ZnO grown on *r*-plane sapphire, a lattice mismatch of 18% along ZnO[$\bar{1}$100] and 1.5% along ZnO[0001] causes the residual strain [83]. Therefore, differences in the residual strain levels of the films deposited on *c*-plane and *r*-plane sapphire substrates are expected when using the same deposition parameters.

Variation of film thickness has potential of affecting the Raman E_2^{high} peak center for the different specimens. Myoung et al. [75] investigated the effects of film thickness on the optical properties of ZnO films. It was reported that the effects of strain from lattice mismatch were completely relaxed for film thickness greater than 400 nm, which indicates that the 100 nm nominal thickness ZnO films of this study may be sensitive to film thickness. A quantitative measure of the residual stress of ZnO films as a function of film thickness has not been reported, so the effect of variation in film thickness on Raman peak shifting is difficult to quantify. Measurement of the film thickness and quantitative investigations of the effects of film thickness would be useful to validate the peak shifting behavior presented in this study. Relative intensities of the Al_2O_3 related peaks were different between the two specimens as a result of the different crystallographic orientations of the substrates. The FWHM of the ZnO E_2^{high} peak was slightly larger for the r-plane sapphire substrate specimen at approximately 11 cm^{-1} as compared to about 9.5 cm^{-1} for the c-plane sapphire substrate specimen. Lattice vibrations are sensitive to lattice distortion, and spatial variation of strain within the Raman probing volume results in peaks with a larger FWHM. A difference in the relative intensity of the E_2^{high} peak and Al_2O_3 peaks was observed between the two specimens. The relative intensity of the E_2^{high} peak was observed to decrease by about 70% for the r-plane sapphire substrate specimen. This may partly be due to the different crystallographic orientations of the films. However, specimens of poor crystalline quality also exhibit low intensity Raman peaks. Therefore, a plausible explanation of the higher FWHM and lower relative intensity of the r-plane sapphire substrate specimen E_2^{high} peak is increased disorder, such as that caused by an increased number of point defects. Raman peak intensity also fluctuates as a function of film thickness. Investigations of the effects of film thickness on Raman peak intensity have revealed relatively small changes in intensity as a function of thickness: for a 5% change in thickness, Raman peak intensities were reported to vary by about 3% for NaS [151] and 4% for an active pharmaceutical ingredient polymer coating [152]. These values were obtained by interpolating the reported results from each publication. Assuming that film thickness variation in this study is no greater than 5%, the 70% decrease in Raman peak intensity cannot be attributed solely to film thickness variaton.

4.1.3 Photoluminescence of Undoped ZnO Films

Photoluminescence (PL) measurements of ZnO films deposited on both c-plane and r-plane sapphire substrates were carried out using the setup described in Section 3.2.1 with the 325 nm wavelength line of a HeCd laser. Measurements were taken at specimen temperatures ranging from 4.2 K to 300 K. Emitted light was directed into a 0.5 m monochromator, dispersed by a 2400 g/mm grating, and detected with a LN_2-cooled charge-couple device (CCD) camera.

Wurtzite structures typically exhibit three free exciton radiative recombinations, referred to as the FX_A, FX_B, and FX_C transitions, consistent with the Birman model [36] and described in Section 2.2.3. Reflection, absorption, and PL techniques have revealed these transitions to occur for ZnO at 3.377 eV, 3.39 eV, and 3.42 eV for FX_A, FX_B, and FX_C, respectively, and excited state transitions have been observed at 3.422 eV, 3.43 eV, and 3.47 eV for $\mathrm{FX}_\mathrm{A}^{n=2}$, $\mathrm{FX}_\mathrm{B}^{n=2}$, and $\mathrm{FX}_\mathrm{C}^{n=2}$, respectively [42]. Reynolds et al. [19] estimated the binding energy of ZnO by taking the difference in the energies of the ground and excited state transitions with the assumption that the excited state is hydrogen-like, or using the Rydberg formula:

$$E_\mathrm{photon} = E_0 \left(\frac{1}{{n_1}^2} - \frac{1}{{n_2}^2}\right).$$

For example, the difference between the ground and excited states of the A-exciton transition, $\mathrm{FX}_\mathrm{A}^{n=2} - \mathrm{FX}_\mathrm{A}^{n=1}$, is 45 meV. This yields a binding energy of $45/0.75 = 60$ meV.

Excitons bound to dopants or lattice defects can also lead to radiative recombination in ZnO. In high quality bulk ZnO, emission is typically dominated by neutral donor bound exciton ($\mathrm{D}^0\mathrm{X}$) emission as a result of unintentional impurities, which are typically observed in the range of 3.348 eV to 3.374 eV with FWHM less than 1 meV [24]. In one naming convention, the bound exciton peaks are labeled I_1 to I_{11} and for simplicity this nomenclature is used here. The origin of many of these peaks has been controversial over the years, and whether some of the peaks result from neutral donor or acceptor bound excitons has been a subject of debate [24, 38, 41]. The peaks I_3 through I_8 are commonly attributed to A-excitons bound to neutral donors and are typically the most prominent [24]. The I_9 through I_{11} peaks have been identified both as neutral acceptor [24] and neutral donor [41] related. The binding energy, or localization energy, of the donor bound excitons to the related donors has been found to range from about 10 to 20 meV [24].

Two electron satellites (TES) are commonly observed for ZnO in the range of 3.32 to 3.34 eV and are a result of the donor remaining in the excited state when radiative recombination of neutral donor bound excitons occurs [24]. Donor acceptor pair (DAP) transitions have also been observed for ZnO near 3.22 eV. LO-phonon replicas are expected to appear in the PL spectra of ZnO. The reported LO-phonon energy of ZnO is 72 meV [22], and thus LO-phonon replicas of ZnO appear with a separation of about 72 meV from the related transition energy.

The near band-edge PL spectrum at 20 K obtained from the film deposited on *c*-plane sapphire is shown in Fig. 4.3. Also shown in Fig. 4.3 is the PL spectrum of bulk single crystal ZnO as presented by Hamby et al. [52]. The absolute intensities of the spectra of the bulk ZnO and the ZnO film were scaled for viewing clarity and cannot be compared because different experimental setups were used. The magnified scale shown for bulk ZnO was maintained as originally presented by Hamby et al. [52] to better show the FX_A peak. Several intense donor bound exciton peaks were reported in the spectrum of bulk ZnO at 20 K in the spectral region of 3.360 to 3.368 eV. In addition to $\mathrm{D}^0\mathrm{X}$ emission, Hamby et al. reported a broad TES peak at about 3.332 eV [153] and free exciton

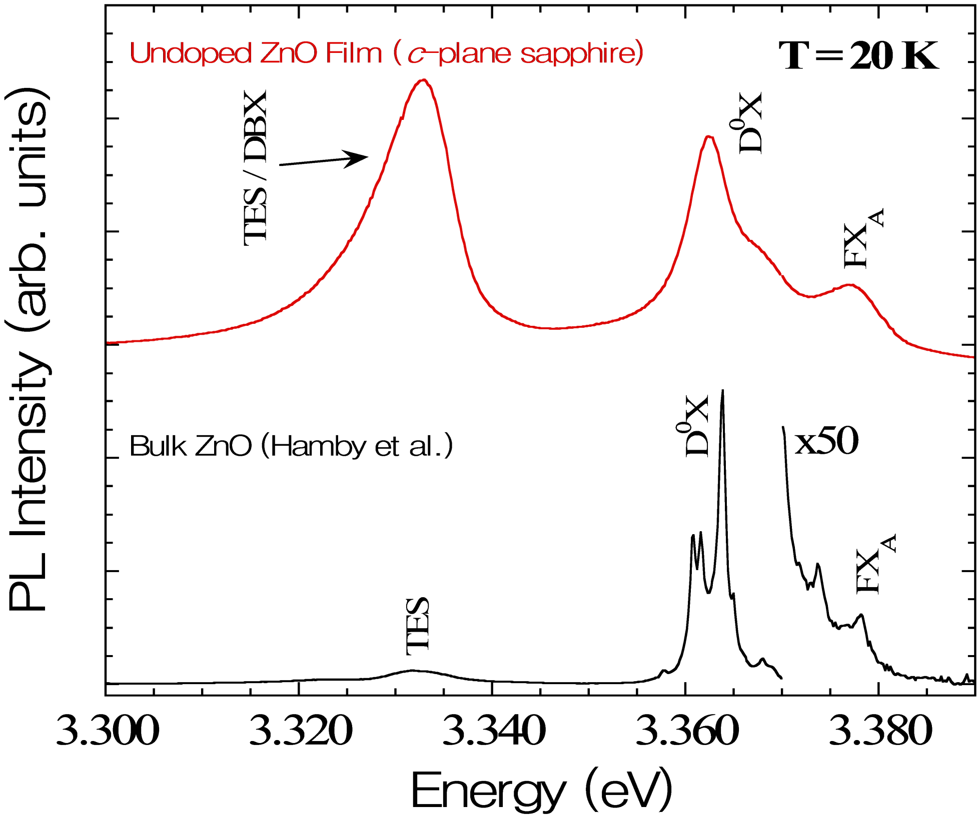

Figure 4.3: Comparison between the PL spectra of the undoped ZnO film on a *c*-plane sapphire substrate and bulk ZnO as presented by Hamby et al. [52].

emission FX_A at 3.378 eV [52]. The undoped ZnO film exhibited peaks at similar spectral locations as bulk ZnO but with some distinct differences. In general, peaks were observed to be wider for the ZnO film, ranging from about 6 to 10 meV. Increased PL peak widths are typically observed for thin films of semiconductor materials as compared to bulk as a result of lower crystalline quality.

For the ZnO film deposited on *c*-plane sapphire, a resolvable FX_A peak was observed near 3.377 eV consistent with reported values in the literature [19, 42, 52]. Compared to reported results for bulk single crystal ZnO, the intensity of the FX_A peak was higher relative to the other observed peaks. This is likely a result of a lower absolute intensity of the donor bound exciton peaks compared to the reported results for bulk ZnO rather than an increase in the absolute intensity of the FX_A peak. The intensity of the peaks related to excitons bound to donors or acceptors depends on the donor or acceptor species and the amount of contaminant present. Therefore, the different contaminants present and different quantities of the contaminants in the undoped film as compared to the bulk specimen investigated by Hamby et al. [52] may be responsible for this relative intensity difference. The temperature dependent behavior of the PL was investigated similar to the work of Hamby et al. [52]. The behavior of the PL spectrum of the ZnO film deposited on *c*-plane sapphire with temperature is shown in Fig. 4.4. At low temperatures, ZnO PL is typically dominated by emission from excitons bound to neutral donors, whereas at higher temperatures free exciton emission dominates. The $\mathrm{FX_A}$ peak was well-resolved when the specimen temperature was increased above 10 K, and became the most intense peak at temperatures greater than 50 K. At temperatures above 150 K, it became difficult to resolve individual peaks due to peak broadening. Analysis of the energy shift of the $\mathrm{FX_A}$ peak as a function of temperature can be used to characterize the behavior of a material, such as the lattice dilatation and electron-phonon interaction [53]. Similar to Hamby et al. [52], a least squares routine was used to fit the temperature dependent behavior of the $\mathrm{FX_A}$ peak to the Manoogian-Woolley (MW) model:

$$E = E_0 + UT^S + V\theta[\coth(\theta/2T) - 1].$$

The MW model is an improvement upon the commonly used Varshni equation [54], which fails to account for the case when the temperature range is less than the Debye temperature (θ_D) [53]. The MW model has previously been applied to II-VI semiconductors such as CdTe [55], CdS [56], and ZnO [52]. In the MW equation, E_0 represents the theoretical band gap at $T = 0$ K, UT^S is the lattice dilatation, and $V\theta[\coth(\theta/2T) - 1]$ is the electron-phonon interaction. Hamby et al. [52] achieved reasonable agreement between the value obtained for U and the theoretical estimate, $U = -3B(\partial E_g/\partial P)\alpha_L$ [55], using reported properties of ZnO: $B = 157$ GPa, $\partial E_g/\partial P = 2.7 \times 10^{-6}$ eV/bar, and $\alpha_L = 4.3 \times 10^{-6}$ K^{-1}. Hamby et al. [52] found V to fall within an order of magnitude of the reported temperature shift for ZnO, -8×10^{-4} eV/K [154].

The temperature dependent shift of the transition energy of several of the observed peaks, as well as the MW fit for the $\mathrm{FX_A}$ peak, for the ZnO film deposited on *c*-plane sapphire is shown in Fig. 4.5. The coefficients obtained for the ZnO film deposited on *c*-plane sapphire were: $E_0 = 3.378$ eV, $U = -9.8 \times 10^{-6}$ eV/K$^{1.01}$, $S = 1.39$, $V = -2.0 \times 10^{-4}$ eV/K, and $\theta = 574.6$ K. These values agree with those reported by Hamby et al. [52] for bulk ZnO, which will be described in more detail in Section 4.2. A comparison between the temperature dependent behavior of the $\mathrm{FX_A}$ peak for the undoped ZnO specimen deposited on *c*-plane sapphire and the reported results of Hamby et al. [52] is shown in Fig. 4.6. The Debye temperature (θ_D) is part of the Debye model, which approximates the lattice contribution to the specific heat of a material [13]. θ_D represents the highest temperature achievable by a single normal vibrational mode, and quantum effects can be observed at temperatures lower than θ_D. θ_D can be estimated using θ from the MW model as $\theta_\mathrm{D} = 4\theta/3$ [53]. This yields a

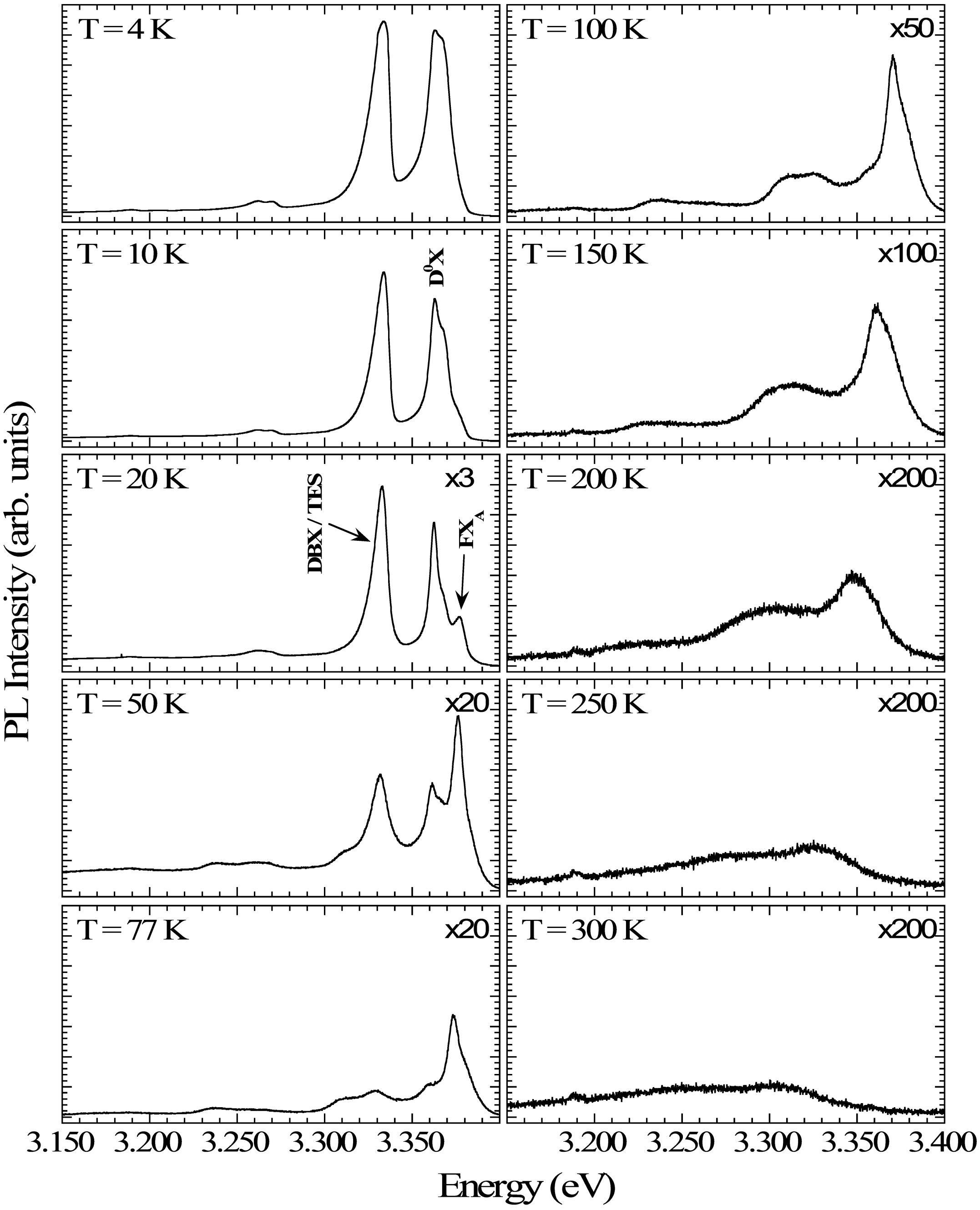

Figure 4.4: Typical temperature dependent PL spectra observed from the undoped ZnO films deposited on *c*-plane sapphire. The plots have been scaled in intensity relative to the spectrum collected at 4 K to the value in the top right corner of each plot.

Debye temperature of about 766 K for the undoped film on *c*-plane sapphire, which is comparable to the reported value for ZnO, 920 K [18]. For bulk single crystal ZnO, Hamby et al. [52] obtained a Debye temperature of 531 K.

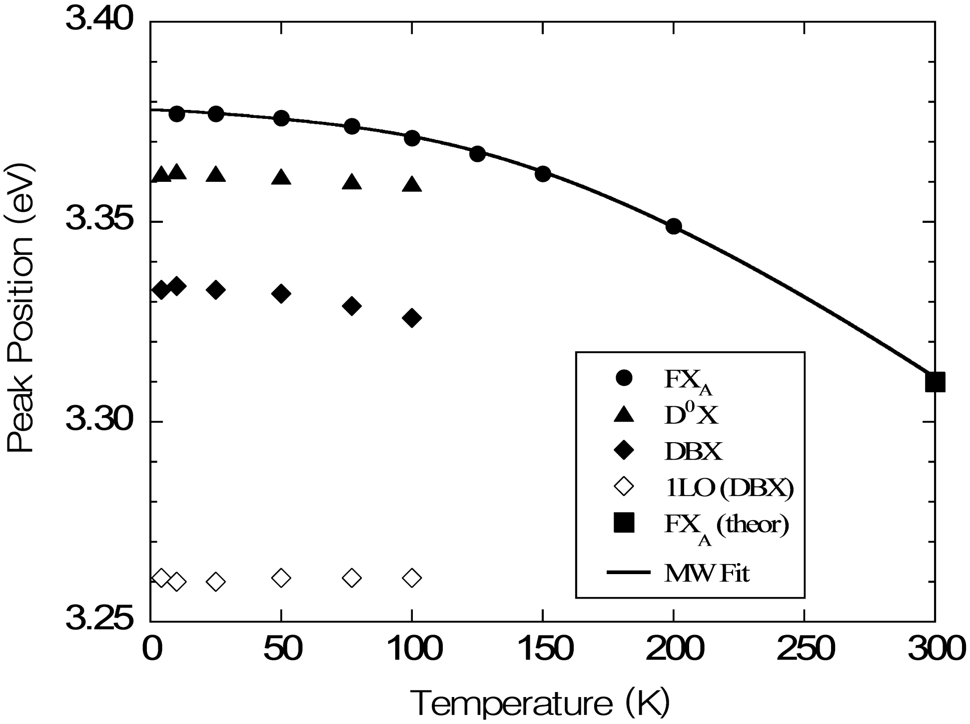

Figure 4.5: Temperature dependent behavior of several different near band-edge emission lines from the undoped ZnO film deposited on *c*-plane sapphire. All peak centers were determined using Gaussian curve fits. FX_A (theoretical) was calculated using the band gap energy of ZnO minus the exciton binding energy.

At temperatures lower than 50 K, strong emission was observed from the undoped ZnO film near 3.364 eV with a resolvable shoulder on the high energy side of the peak. This peak falls within the spectral range of the D^0X peaks reported by Hamby et al. [52] for bulk single crystal ZnO. A good fit to the experimental data was achieved using two Gaussian peak fits: one for the strong peak and one for the shoulder. The stronger peak was found to have a peak center at 3.362 eV. The localization energy, or the exciton binding energy to the donor, can be approximated by subtracting the peak energy from the transversal free A-exciton energy (reported at 3.3759 eV) [41]. For this peak, this method yields a localization energy of 13 meV. The temperature dependent behavior of

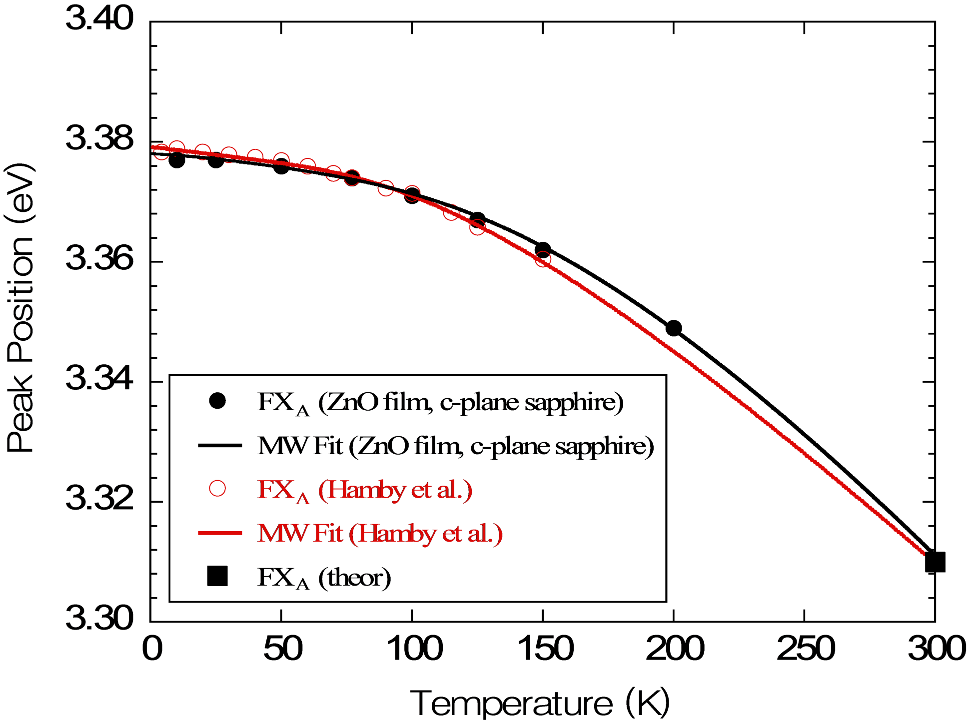

Figure 4.6: Comparison of the MW fit between the ZnO film deposited on *c*-plane sapphire and bulk single crystal ZnO as reported by Hamby et al. [52].

the peak can also be used to approximate localization energy [52]. The localization energy in turn gives evidence to the type of recombination occurring. By plotting the natural logarithm of the normalized total intensity (FWHM×intensity) of the D^0X peak as a function of the inverse of the temperature, the slope of the linear portion of the curve gives an approximation of the localization energy in K. The Boltzmann constant, k, can then be used to convert the localization energy to meV, $E_{\mathrm{loc}}(\mathrm{meV}) = 8.61733 \times 10^{-2} E_{\mathrm{loc}}(\mathrm{K})$. Figure 4.7 shows this plot for the strongest peak in the D^0X region for the ZnO film deposited on *c*-plane sapphire. The slope of the linear portion of the curve gives a localization energy of 10 meV. Thermal quenching, or the reduction in luminescence efficiency, typically occurs as non-radiative relaxation pathways are created by thermal mechanisms and the probability of non-radiative recombination increases [155, 156]. The linear fit in Fig. 4.7 is only an approximation: the total normalized intensity will go to zero (or the natural logarithm of the total normalized intensity approaches minus infinity) as temperature is increased and the PL emission is completely quenched.

Meyer et al. [41] reported the I_4 peak at 3.3628 eV with localization energy of 13.1 meV. Zheng

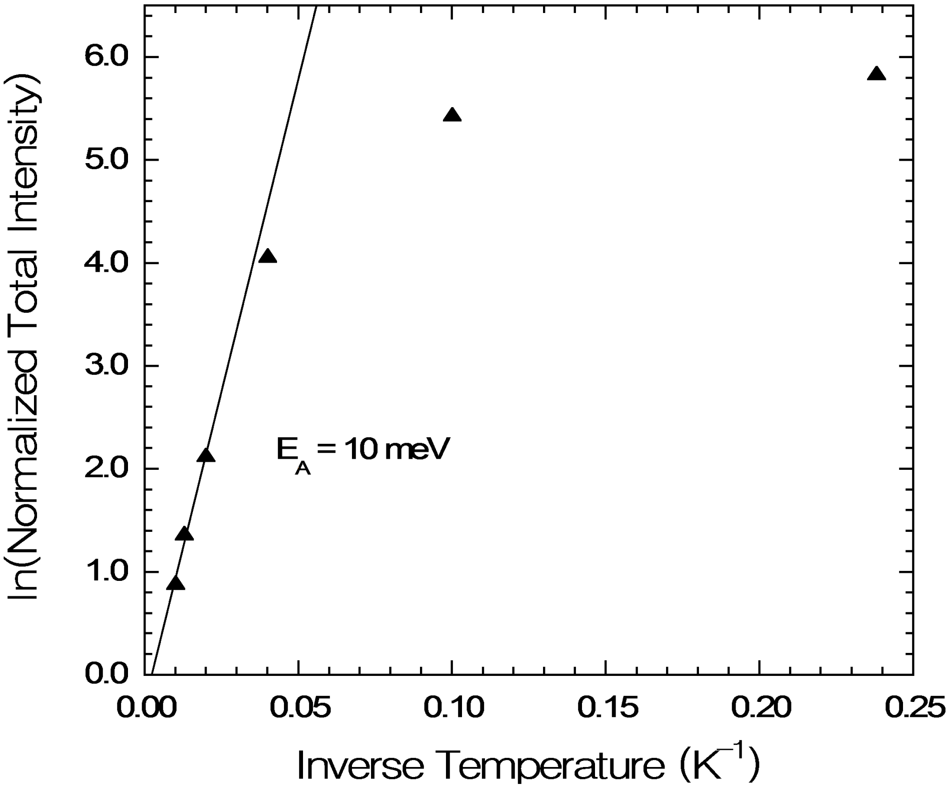

Figure 4.7: Natural logarithm of the normalized total intensity of the ZnO deposited on *c*-plane sapphire D^0X peak plotted against the inverse of temperature. The slope of the linear portion approximates a localization energy of 10 meV.

et al. [141] reported the I_4 peak as the most intense emission at low temperatures from ZnO epitaxial films grown on *r*-plane sapphire. Therefore, in the present study, the peak centered at 3.364 eV with an estimated localization energy of 10 meV is being attributed to the I_4 peak. Meyer et al. [41] utilized magnetic resonance techniques to attribute this peak to H shallow donors. Additionally, they reported that this peak was often observed in specimens prior to annealing. After annealing, the peak was reported to decrease substantially in intensity, potentially a result of the removal of H at high temperatures.

The shoulder on the I_4 peak was centered at 3.369 eV and was only resolvable at temperatures below 20 K. Meyer et al. [41] reported the I_1, I_2, and I_3 peaks to be centered at 3.3718 eV, 3.3674 eV and 3.3665 eV, respectively. Based on the spectral location of the shoulder, this could be the I_1, I_2, or I_3 peak. Reynolds et al. [38] attributed the I_2 and I_3 peaks to ionized donor bound exciton complexes. Further studies would be required to determine the origin of this peak.

A difference between the undoped ZnO film specimen deposited on *c*-plane sapphire and reported results for bulk ZnO was observed near 3.33 eV. While both specimens showed a peak near this location, the intensities relative to the neutral donor bound exciton emission were different. For bulk ZnO, Hamby et al. [153] attributed this peak to two electron satellites (TES) of the neutral donor bound exciton emission.

Each of the neutral donor bound exciton emission peaks I_4 through I_9 has been shown to have a corresponding TES peak [41]. Using effective mass theory, Thonke et al. [47] showed that the TES peaks should be separated from the corresponding donor bound exciton peaks by 3/4 of the donor binding energy. The intensity of the TES emission is typically orders of magnitude less than the neutral donor bound exciton emission. Teke et al. [42] reported the TES of the I_4 peak at 3.3268 eV. However, the intensity being stronger than that of the I_4 peak suggests that another recombination mechanism exists in addition to a TES.

Peaks have been observed in the PL spectra of ZnSe [48, 50] and ZnTe [49] that were the result of localized recombination at extended defects. Meyer et al. [41] reported a peak at 3.333 eV in a bulk ZnO specimen, and by analyzing the activation energy of the emission, theorized that the peak was similar to those observed for ZnSe and ZnTe. Using spatially resolved cathodoluminescence (CL) spectroscopy on a bulk ZnO specimen with this feature, Meyer et al. [41] reported that the 3.333 eV band was localized and appeared to correlate with structural irregularities in the specimen. It was concluded that the 3.333 eV line, named DBX, was related to excitons bound to structural defects. The peak near 3.33 eV observed in the ZnO film in this study is probably a combination of a TES of the I_4 peak and DBX emission. The peak is skewed toward the low energy side of center, which indicates a more intense DBX line near 3.333 eV and less intense TES peak near 3.327 eV. The observation of the DBX peak may indicate that the ZnO film has a relatively large number of structural defects as compared to bulk ZnO. These structural defects may be related to extended defects, such as grain boundaries. In this case, the lack of grain boundaries in the bulk single crystal ZnO describes the lack of the DBX peak in the PL spectrum. The ability to resolve neutral donor bound exciton emission and free exciton emission is consistent with ZnO films with relatively high crystalline quality, but when compared to high quality bulk ZnO a relative decrease in crystalline quality is expected.

Less intense peaks were observed in the PL spectra of both bulk and film ZnO specimens at lower energies corresponding to LO-assisted recombination associated with the more intense peaks, with a spacing approximately equal to the LO phonon energy of ZnO (72 meV [22]). Teke et al. [42] observed first-, second-, and third-order LO-assisted peaks from D^0X, TES, and DAP emission separated in intervals of 71-73 meV from the related peak. Figure 4.8 identifies the 1LO (DBX) and 2LO (DBX)

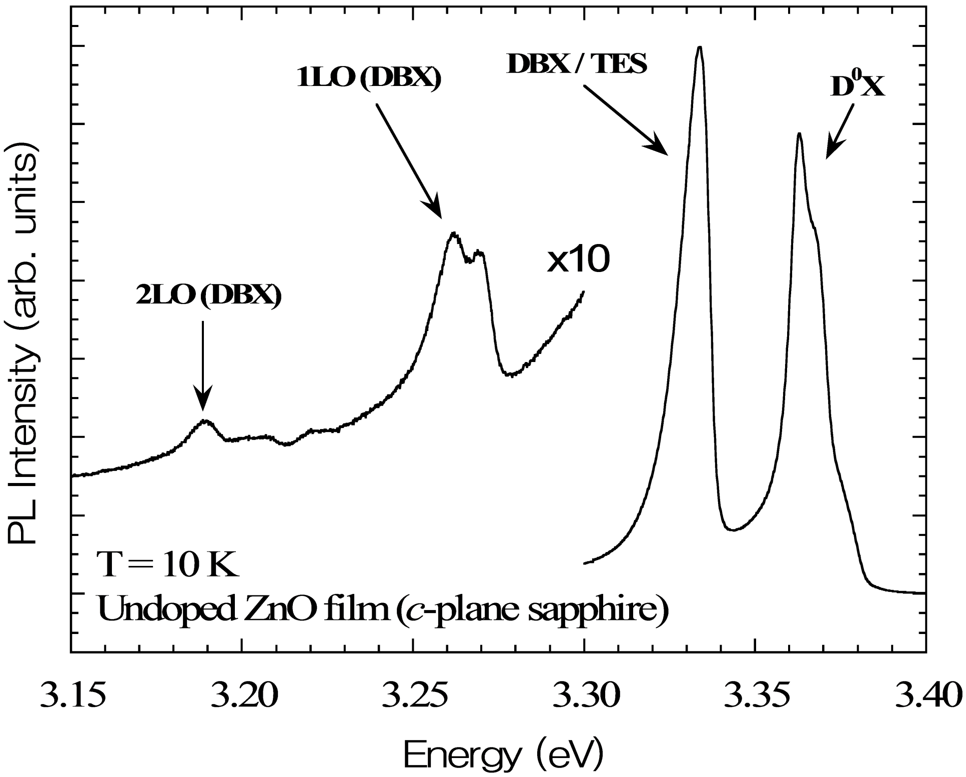

Figure 4.8: PL spectrum of the undoped ZnO film deposited on *c*-plane sapphire showing the LO-phonon replicas of the DBX peak at 10 K.

peaks, which were observed at energies 72 meV and 144 meV below the DBX line, respectively. The origin of the additional peak on the high energy side of the 1LO (DBX) peak is unclear. Based on spectral location, this could be a LO-phonon replica of a TES peak. The first-order LO-assisted replica of the D^0X peak was not observed from this specimen, possibly a result of being overwhelmed by the DBX/TES peak. A very low intensity peak near 3.22 eV was observed, which may be the second-order LO assisted D^0X peak. For measurements taken at temperatures below 100 K the most intense peak in the PL spectrum, whether DBX or D^0X, exhibited evidence of LO-phonon replicas. At higher temperatures where free exciton emission became dominant, LO-assisted peaks were not observed.

Overall, the ZnO films deposited on *c*-plane sapphire exhibited more intense emission than films deposited on *r*-plane sapphire, as shown in Fig. 4.9. The FWHMs of the resolvable peaks were comparable between the two sets of specimens. The FX_A peak was more resolvable in the spectrum of the film deposited on *c*-plane sapphire. The more intense overall emission and resolvable FX_A peak indicated that the specimen deposited on *c*-plane sapphire was of higher crystalline quality.

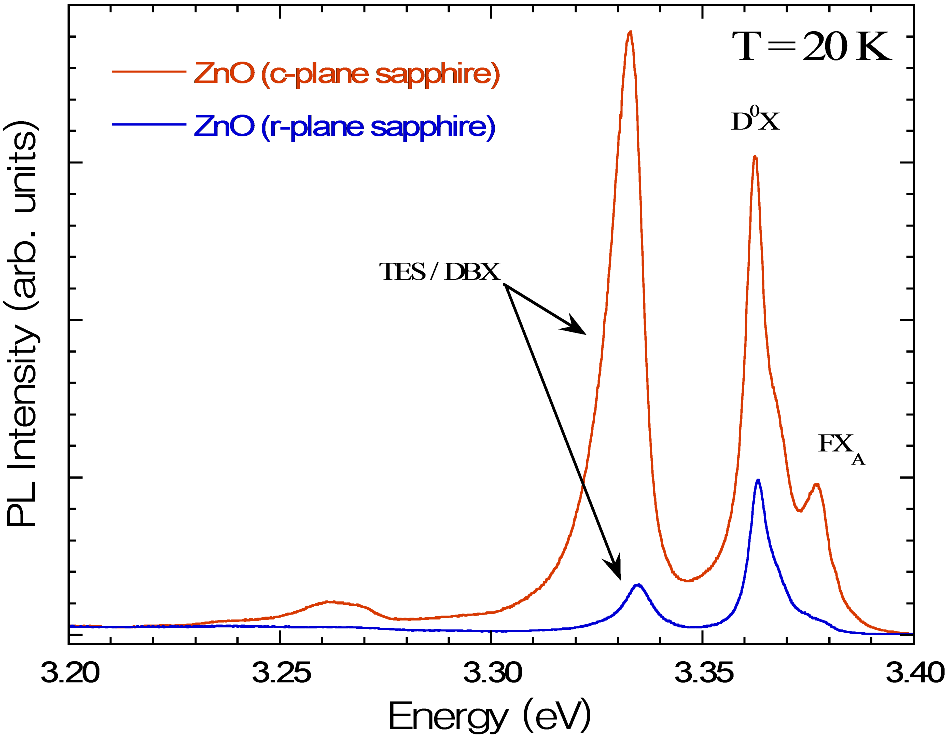

Figure 4.9: PL spectra of ZnO films deposited on *c*-plane sapphire and *r*-plane sapphire at 20 K. The spectra are plotted on the same absolute intensity scale.

The optical response of ZnO films deposited on *r*-plane sapphire has been reported to depend strongly on growth parameters. Zheng et al. [141] observed differences in the PL spectra of ZnO films deposited on *r*-plane sapphire when grown at different temperatures. At growth temperatures of 500 °C and 550 °C strong near band-edge emission was observed, similar to the spectrum of bulk ZnO. However, at 450 °C the spectrum was dominated by a broader peak centered near 3.37 eV. Stronger emission from ZnO deposited on *r*-plane sapphire as compared to *c*-plane sapphire has also been reported [157]. The optical response of ZnO films is sensitive to growth parameters and film thickness, and thus direct comparisons to the literature are difficult.

The origin of the visible emission of ZnO has been a subject of controversy for many years. The emission has been attributed to Cu impurities [60], oxygen defect centers $\mathrm{V_O}$ with Zn defect centers $\mathrm{V_{Zn}}$ [63,64], Zn interstitial defects $\mathrm{Zn_i}$ [68], oxide antisite defects $\mathrm{O_{Zn}}$ [69], and free carrier depletion at the surface [62]. The visible emission is likely a result of several of these defects. The visible emission has been used as indication of quality of ZnO films, where a higher near band-edge emission to visible emission intensity ratio indicates that fewer point defects exist. Du et al. [70] reported intense NBE emission with no resolvable visible emission from ZnO nanoparticles encapsulated in a

PMMA matrix. The quenched visible emission was attributed to defects being eliminated from the surface of the nanoparticles.

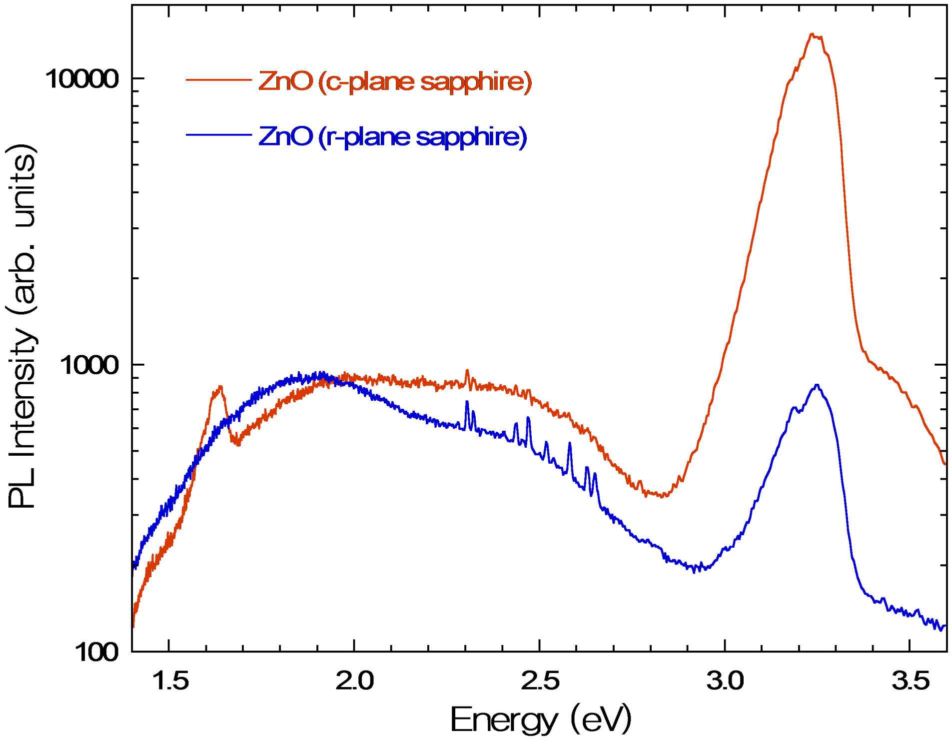

Figure 4.10: Room temperature PL of ZnO films deposited on *c*-plane and *r*-plane sapphire. The spectra are plotted on the same absolute intensity scale.

Room temperature PL spectra of the ZnO films deposited on *c*- and *r*-plane sapphire were collected in a backscattering configuration using the commercial confocal microscope system (WITec, GmbH) described in Section 3.2.2. Figure 4.10 shows visible emission similar in intensity between the specimens deposited on *c*-plane and *r*-plane sapphire. However, the near band-edge emission observed was an order of magnitude greater in intensity for the specimen deposited on *c*-plane sapphire. The intense near band-edge emission suggests that fewer point defects exist, as does the increased near band-edge to visible emission ratio. A low intensity peak centered near 3.4 eV was observed in the PL spectrum of the undoped film deposited on *c*-plane sapphire, which was not observed for the undoped film deposited on *r*-plane sapphire. Muth et al. [73] reported optical transmission peaks at 295 K from ZnO films deposited on *c*-plane sapphire related to free exciton emission FX_A, FX_B, and FX_C centered at 3.40 eV, 3.45 eV, and 3.55 eV, respectively. The higher intensity of the PL emission of the film deposited on *c*-plane sapphire near 3.4 eV may be a result of weak free exciton emission from this specimen.

In this section, the Raman and PL spectra of ZnO deposited on *c*- and *r*-plane sapphire substrates were compared to measured and reported results for bulk single crystal ZnO. The results suggested that the ZnO deposited on *c*-plane sapphire exhibit higher crystalline quality than ZnO deposited on *r*-plane sapphire, possibly a result of fewer point defects. The ZnO films were shown to exhibit donor bound exciton emission and free exciton emission similar to that reported for bulk ZnO. The DBX peak was also observed for the ZnO films, which Meyer et al. [41] attributed to excitons bound to structural defects.

4.2 ReO$_2$-Doped ZnO Films

In Section 4.1, the undoped ZnO films deposited on *c*- and *r*-plane sapphire substrates were shown to have Raman and PL spectra that were consistent with results for bulk single crystal ZnO. The effects of doping ReO$_2$ in ZnO films is presented below using the results for the undoped ZnO films as a baseline.

4.2.1 X-ray Diffraction of ReO$_2$-Doped ZnO Films

As described in Section 4.1.1, XRD peaks were observed from ZnO and Al$_2$O$_3$ for ZnO grown on both *c*- and *r*-plane sapphire substrates. XRD patterns of the doped specimens were very similar with the exception of the 50 wt. % ReO$_2$-doped film on *c*-plane sapphire, which showed a decrease in intensity of the (0002)ZnO peak and the appearance of a well resolved (0002)ReO$_2$ peak.

The lack of the ReO$_2$ peak at doping concentrations as high as 20 wt. % may give some indication of the Re doping saturation concentration in ZnO. Jin et al. [108] investigated the solubility limits of Sc, Ti, V, Cr, Mn, Fe, Co, Ni, and Cu ions in ZnO. Solubility limits were determined by the appearance of impurity peaks in the XRD pattern. For each transition metal ion, it was reported that below solubility limits, the wurtzite structure of ZnO was maintained. Jin et al. attributed the appearance of impurity peaks to the existance of precipitated phases. Therefore, a plausible explanation of the XRD results of the present study is that at low concentrations of Re, the ZnO wurtzite structure is maintained, and at doping concentrations greater than saturation, a precipitated phase of ReO$_2$ forms. This would explain the appearance of the ReO$_2$ peak in the diffraction pattern from the 50 wt. % ReO$_2$ specimen. At lower doping concentrations, the amount of ReO$_2$ may be too low to be detected by XRD if it exists.

4.2.2 Raman Spectroscopy of ReO_2-Doped ZnO Films

Figure 4.11 shows typical Raman spectra for ZnO films doped with varying concentrations of ReO_2 deposited on *c*- and *r*-plane sapphire. For each of the specimens, the E_g and A_{1g} peaks attributed to Al_2O_3 were observed as a result of the substrate. The ZnO E_2^{high} peak was observed in the spectrum of each specimen near 438 cm^{-1}, and no other ZnO related peaks appeared. The Raman peaks related to Al_2O_3 and ZnO were described in more detail in Section 4.1.2. No additional peaks were observed as a result of doping the films with ReO_2. The Raman spectrum of crystalline ReO_2 has not been extensively studied. Kuzmin et al. [158] investigated the Raman spectrum of $(1-x)\text{WO}_{3-y} \cdot x\text{ReO}_2$ mixtures with x as large as 0.81, and no ReO_2 related peaks were reported. Kuzmin et al. attributed the lack of a ReO_2 related peak to the high symmetry and metallic conductivity of ReO_2, both of which reduce Raman activity. If precipitated phases of ReO_2 are forming in the films, the amounts are too small to create a resolvable Raman peak. The apparent slope of the background in the plots is a result of the visible PL background, which is emphasized more on the plots with larger intensity scaling.

The E_2^{high} mode was the only ZnO-related peak observed for the undoped and doped ZnO specimens as described in Section 4.1.2. A Gaussian curve was fit to the E_2^{high} peak for each of the specimens, from which the peak center and FWHM were determined. An increase in the intensity of the E_2^{high} peak at low ReO_2 concentrations relative to the intensity of the Al_2O_3 peaks was observed. Figure 4.12 shows the intensity ratio of the ZnO E_2^{high} peak to the Al_2O_3 A_{1g} peak for the ZnO films deposited on *c*- and *r*-plane sapphire as a function of ReO_2 concentration. For the films deposited on *c*-plane sapphire, the 5 wt. % ReO_2 specimen showed the strongest relative E_2^{high} intensity, and for the films deposited on *r*-plane sapphire the 5 wt. % and 10 wt. % ReO_2 specimens showed the strongest relative intensity. Above these ReO_2 concentrations a decrease in the relative intensity was observed for both *c*- and *r*-plane sapphire substrate specimens. The 50 wt. % ReO_2 specimen deposited on *r*-plane sapphire exhibited no distinguishable E_2^{high} peak. The low intensity peaks observed in the Raman spectrum of this specimen in the region of the E_2^{high} peak are centered at 431.5 cm^{-1} and 450.2 cm^{-1} and are attributed to Al_2O_3 E_g modes that have been reported at 432 cm^{-1} and 451 cm^{-1}, respectively [143]. As described in Section 4.1.2, specimens of poor crystalline quality exhibit low intensity Raman peaks. The behavior shown in Fig. 4.12 may indicate that small doping concentrations (5 to 10 wt. %) of ReO_2 increase the crystalline quality of the ZnO films, but higher doping concentrations decrease the crystalline quality.

The peak center position determined from the peak fit of the E_2^{high} mode for each specimen is

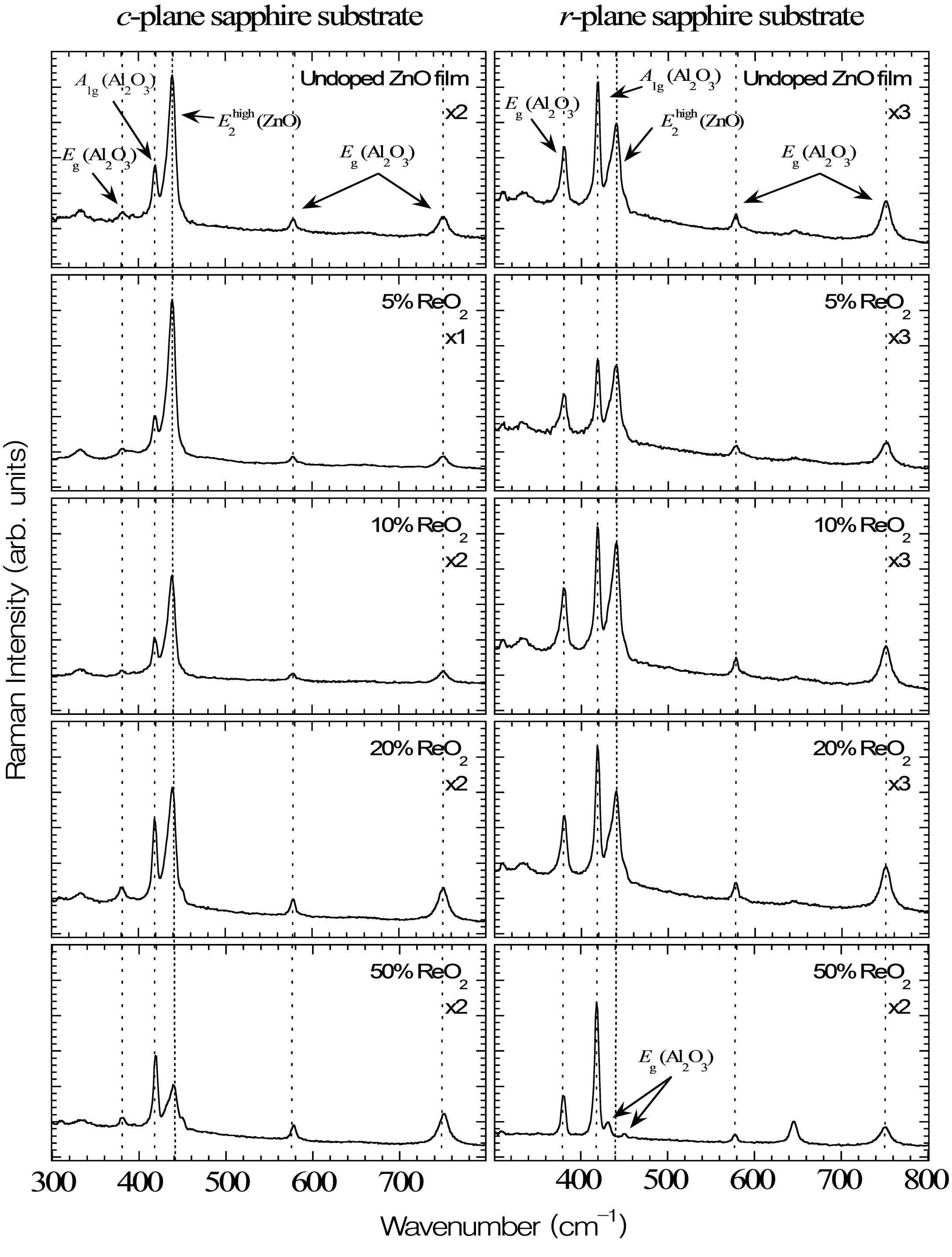

Figure 4.11: Typical Raman spectra of ZnO thin films doped with varying concentrations of ReO$_2$ deposited on c- and r-plane sapphire. The plots have been scaled in intensity to the value in the top right corner of each plot.

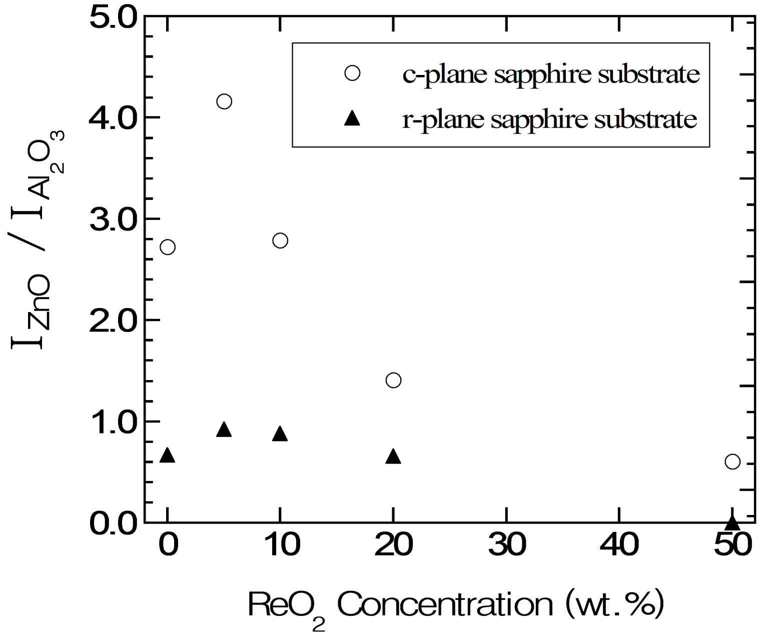

Figure 4.12: Intensity ratio of the ZnO E_2^{high} peak to the Al_2O_3 A_{1g} peak as a function of ReO_2 concentration for ZnO films deposited on *c*- and *r*-plane sapphire.

shown plotted as a function of ReO_2 doping concentration in Fig 4.13. In Section 4.1.2 the peak center identification accuracy was reported to be about 0.5 cm^{-1}. Most of the spectral shifts observed were greater than the estimated accuracy of the instrument. The strain scale in Fig. 4.13 is based on the documented shift of the E_2^{high} peak with in-plane strain from the literature, -6.67 $cm^{-1}/\%$ [33], and the assumption that the unstrained peak is centered at 438 cm^{-1}. Zheng et al. [141] observed positive shifts in the E_2^{high} mode spectral position with increasing compressive strain as characterized by XRD. The ZnO Raman mode from the specimen doped with 50 wt. % ReO_2 on *r*-plane sapphire was too weak to be detected, and does not appear in the plots. The behavior of the E_2^{high} peak center as a function of ReO_2 doping concentration are similar to the relative intensity behavior shown in Fig. 4.12. This indicates that low ReO_2 concentrations relieve the compressive strain in the films, but higher doping concentrations increase the compressive strain.

Figure 4.14 shows the FWHM of the E_2^{high} peak as a function of ReO_2 concentration. At concentrations up to 20 wt. % ReO_2, the FWHM exhibited little variation. However, an increase in the FWHM of the E_2^{high} peak was observed for the 50 wt. % ReO_2 film on the *c*-plane sapphire substrate. The E_2^{high} peak was not observed for the 50 wt. % ReO_2 film on the *r*-plane sapphire substrate and thus cannot be compared. In general, a larger FWHM of the E_2^{high} peak of films deposited on *r*-plane sapphire was observed compared to films deposited on *c*-plane sapphire. A plausible explanation for this behavior was presented in Section 4.1, which is that the film deposited on *r*-plane sapphire exhibited more disorder, such as that caused by an increased number of point defects. Extending this explanation to ReO_2-doped specimens, it is implied that the 50 wt. % ReO_2 specimen deposited on *c*-plane sapphire exhibits structural disorder similar to the undoped specimen deposited on *r*-plane sapphire.

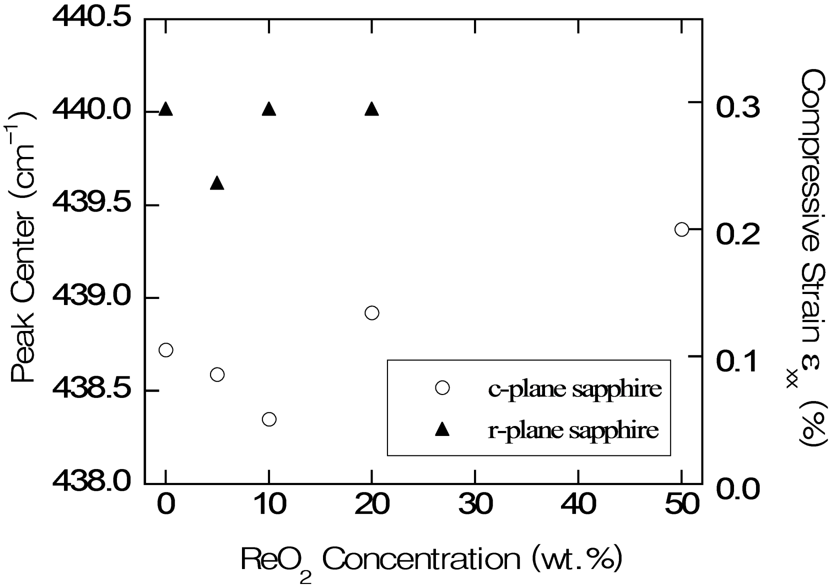

Figure 4.13: Raman peak center of the ZnO E_2^{high} peak and correlating in-plane compressive strain as a function of ReO_2 doping concentration for ZnO films deposited on *c*- and *r*-plane sapphire.

A possible explanation of the XRD results was presented in Section 4.2.1: the wurtzite structure of ZnO may be maintained for small Re doping concentrations, but at larger concentrations precipitated ReO_2 may form. At doping concentrations of 5-10 wt. % ReO_2, the Raman peak shifting results showed that residual compressive stress levels in the films decreased, and the relative intensity ratios of the ZnO and Al_2O_3 Raman peaks suggested that crystalline quality increased. At higher doping concentrations, Raman peak shifting indicated increased compressive stress levels and relative intensities suggested decreased crystalline quality. Shannon [159] reported the ionic radius of Re to range from 0.67-0.77 Å depending on the charge, as compared to 0.88 Å for Zn^{2+}. A plausible explanation for the decrease in compressive stress in the films at low Re doping concentrations is that Re ions are substituting at Zn sites, as the smaller ionic radius of Re would relieve strain.

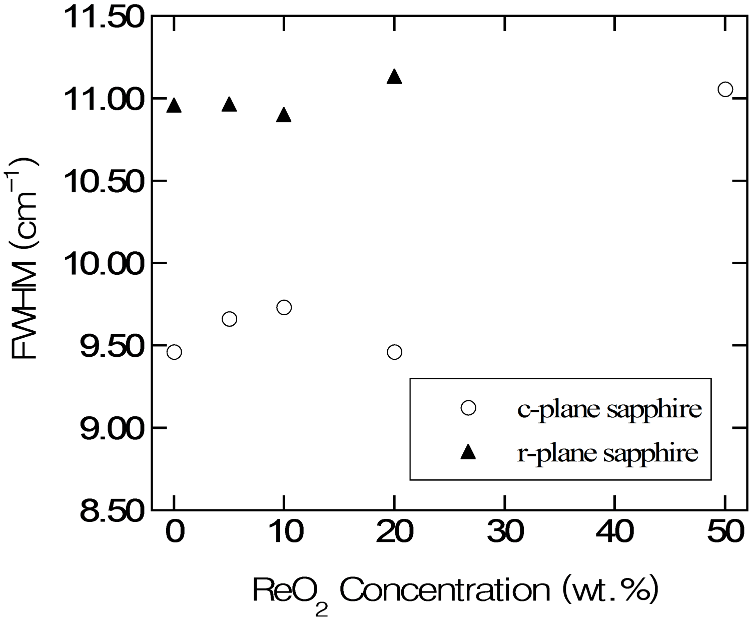

Figure 4.14: ZnO E_2^{high} peak FWHM as a function of ReO_2 doping concentration for ZnO films deposited on *c*- and *r*-plane sapphire.

4.2.3 Photoluminescence of ReO_2-Doped ZnO Films

The effect of doping ZnO with ReO_2 was further investigated by analyzing the near band-edge PL spectra of each of the specimens. Figures 4.15, 4.16, and 4.17 show the PL spectra of both *c*- and *r*-plane sapphire substrate specimens for each ReO_2 concentration at temperatures of 10 K, 20 K, and 77 K, respectively. At 10 K, the D^0X peak was observed in the spectra of all specimens. At doping concentrations of 5 wt. % ReO_2, the absolute intensity of the D^0X peak increased by a factor of about 2 compared to the undoped specimens. Figure 4.16 shows that at concentrations higher than 5 wt. % ReO_2, D^0X peak intensity decreased with increasing doping concentration. This behavior is similar to the Raman spectroscopy results presented in Section 4.2.2, which showed that the relative intensity of the ZnO Raman peak compared to the sapphire substrate Raman peak increased at doping concentrations of 5 wt. % ReO_2, then decreased with increasing doping concentration. A discrepancy was observed in this behavior for the 20 wt. % ReO_2-doped ZnO film deposited on *c*-plane sapphire at 10 K. For this specimen, an increase in the intensity of the D^0X peak was observed compared to the 10 wt. % ReO_2 specimen. The DBX peak for this specimen was of very low intensity. This behavior may be a result of the quenching of the DBX emission mechanism for the 20 wt. % ReO_2 film, which allowed an increased efficiency of the D^0X recombination mechanism. As temperature was increased, quenching of the DBX mechanism for the other specimens started to occur, and therefore this discrepancy was no longer observed for the 20 wt. % ReO_2 film at higher temperatures.

The peak designated to be a combination of TES and DBX emission for the undoped specimens in Section 4.1.3 decreased in intensity for the Re-doped specimens. As described in Section 2.2.3, the DBX peak is attributed to excitons bound to structural defects, possibly extended defects such as grain boundaries. The decrease in intensity of this peak with increasing Re doping concentration may suggest that the Re ions reduce the number of these extended defects in the ZnO films. The spectra at 20 K show low intensity FX_A peaks for *c*-plane sapphire substrate specimens doped with up to 20 wt. % ReO_2. At 77 K, FX_A emission was observed from all specimens except those doped with 50 wt. % ReO_2. Reynolds et al. [19] were the first to observe free exciton emission from bulk ZnO only after high quality bulk ZnO specimens became available. The ability to resolve the FX_A peak suggests that the ZnO films are of high crystalline quality. The less intense FX_A peak observed from the *r*-plane sapphire substrate specimens and the specimens doped with high Re concentrations may be the result of an increased number of point defects. The type of defect caused by the Re ions when incorporated into the ZnO lattice structure may explain this behavior. One possibility is that at low Re doping concentrations, Re ions substitute at Zn sites, but with an increasing number of Re ions, a higher percentage of the Re ions are forced into interstitial sites. The feasible explanation first presented in Section 4.2.1 was that ReO_2 phases precipitate at high Re doping concentrations. This could also explain the decrease in overall emission intensity at high Re doping concentrations.

The natural logarithm of the normalized total intensity (FWHM×intensity) of the D^0X peak was plotted as a function of inverse temperature for each of the Re-doped specimens to approximate the localization energies. Figure 4.18 shows the plots for the undoped, 5 wt. % ReO_2, and 50 wt. % ReO_2 specimens on *c*-plane sapphire, and the undoped and 5 wt. % ReO_2 specimens on *r*-plane sapphire. For the *r*-plane sapphire substrate specimens, the D^0X peak was not resolvable at a wide range of temperatures for high doping concentrations. Therefore, only the 5 wt. % ReO_2 specimen is shown. Table 4.2 shows the localization energies of the D^0X transition for all specimens. Each of the localization energies were calculated to be near the 10-20 meV range expected for D^0X emission. Within experimental uncertainty, these results agree with results for bulk ZnO [52]. Therefore, the peaks observed near 3.36 eV for the Re-doped specimens are also being attributed to D^0X emission. Low doping concentrations appear to increase the localization energy of the D^0X peak slightly, but the cause of this is currently unknown.

As shown in Fig. 4.17, free exciton emission FX_A was observed from all of the specimens at 77 K except those doped with 50 wt. % ReO_2. The undoped, 5 wt. % ReO_2, 10 wt. % ReO_2,

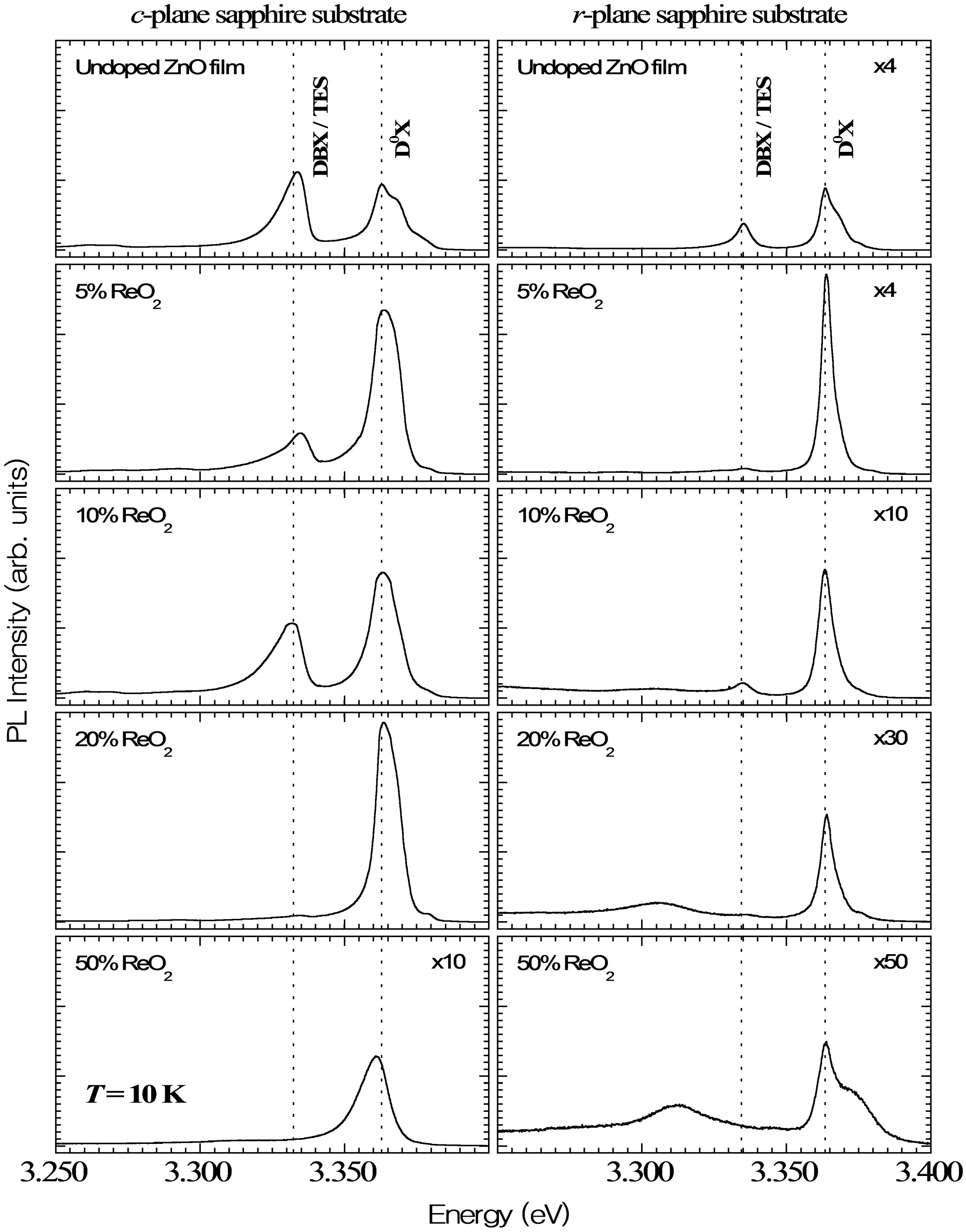

Figure 4.15: Near band-edge emission at 10 K from ZnO deposited on *c*- and *r*-plane sapphire doped with various concentrations of ReO_2. The plots have been scaled in intensity relative to the undoped *c*-sapphire substrate specimen to the value in the top right corner of each plot.

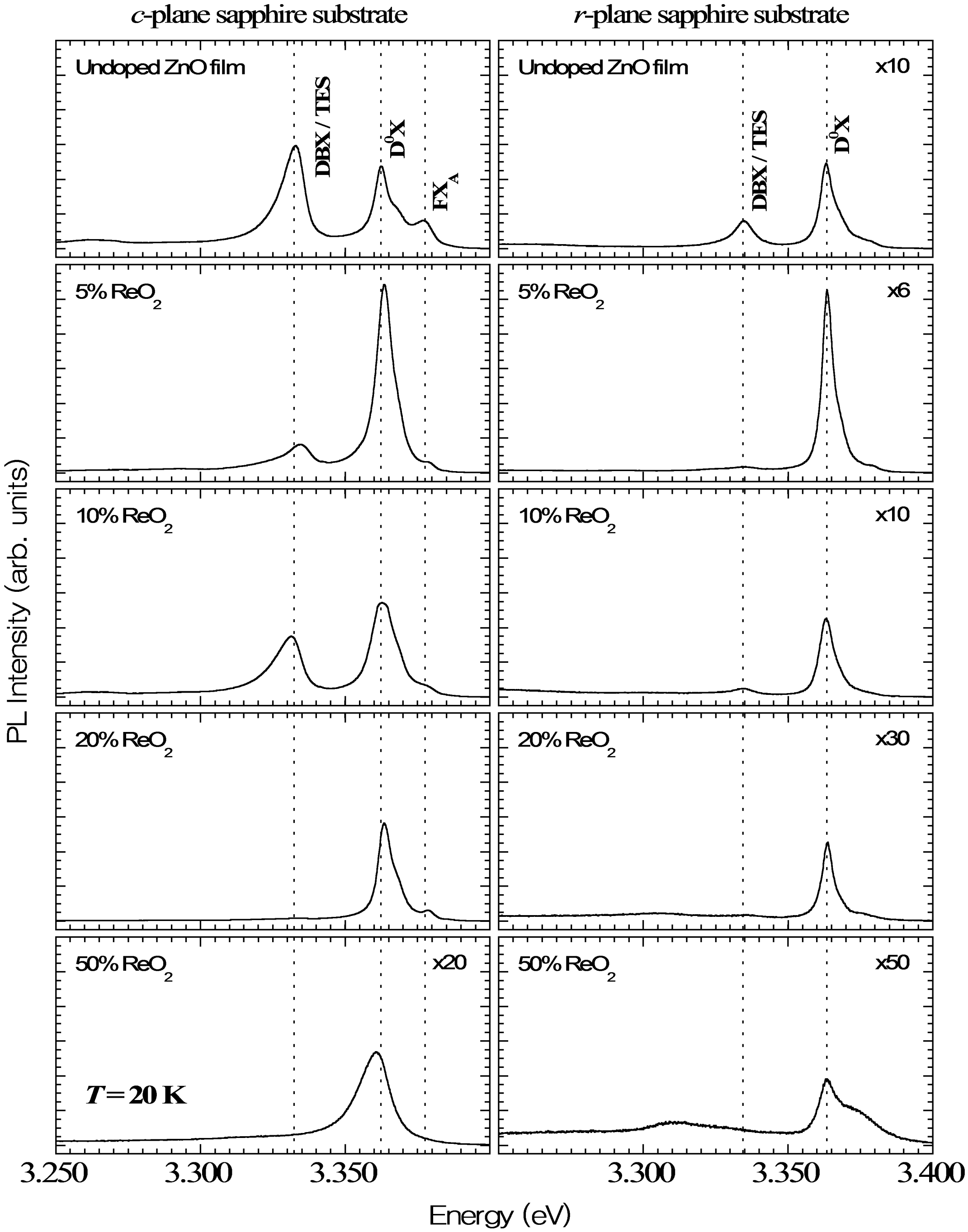

Figure 4.16: Near band-edge emission at 20 K from ZnO deposited on *c*- and *r*-plane sapphire doped with various concentrations of ReO_2. The plots have been scaled in intensity relative to the undoped *c*-sapphire substrate specimen to the value in the top right corner of each plot.

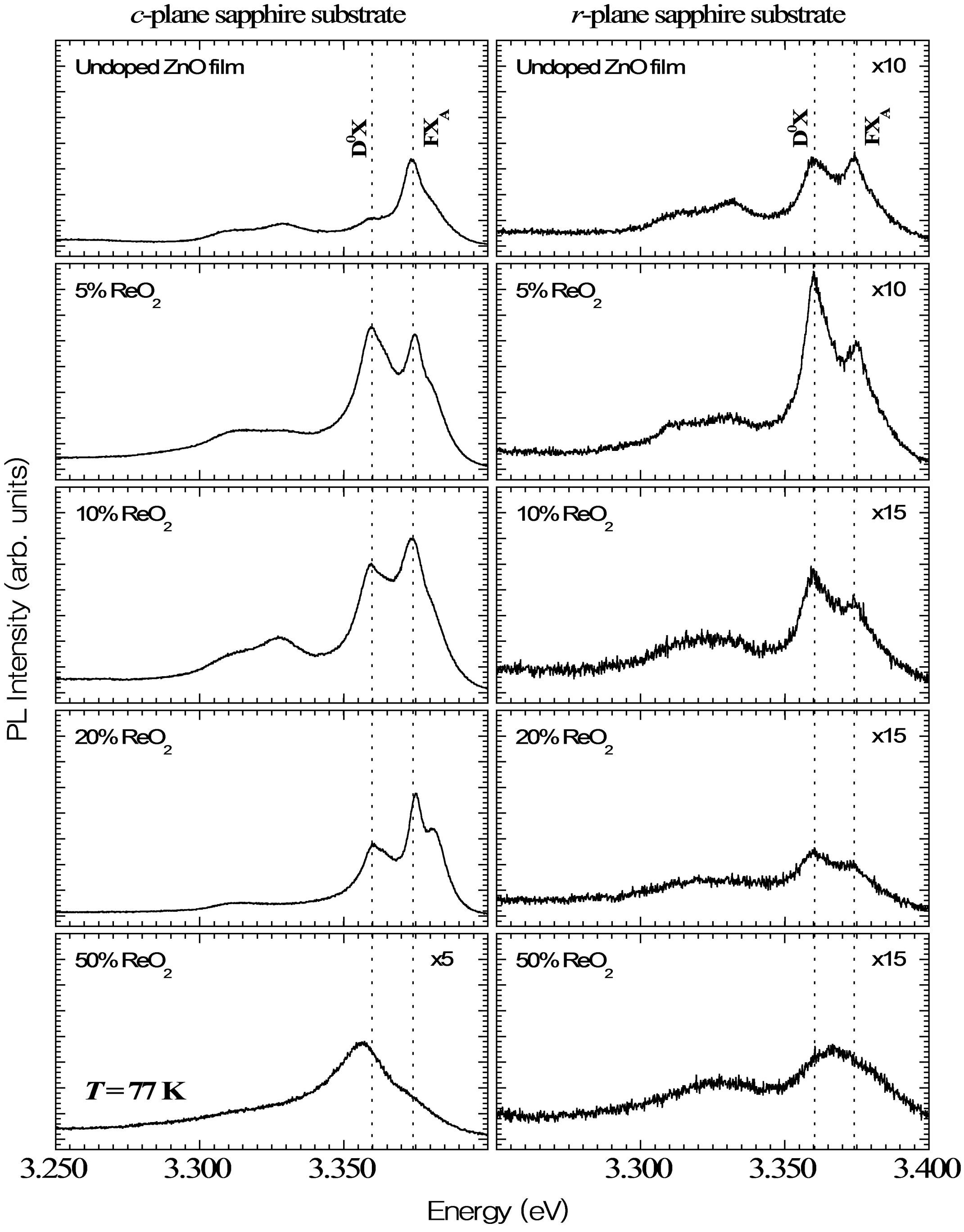

Figure 4.17: Near band-edge emission at 77 K from ZnO deposited on *c*- and *r*-plane sapphire doped with various concentrations of ReO_2. The plots have been scaled in intensity relative to the undoped *c*-sapphire substrate specimen to the value in the top right corner of each plot.

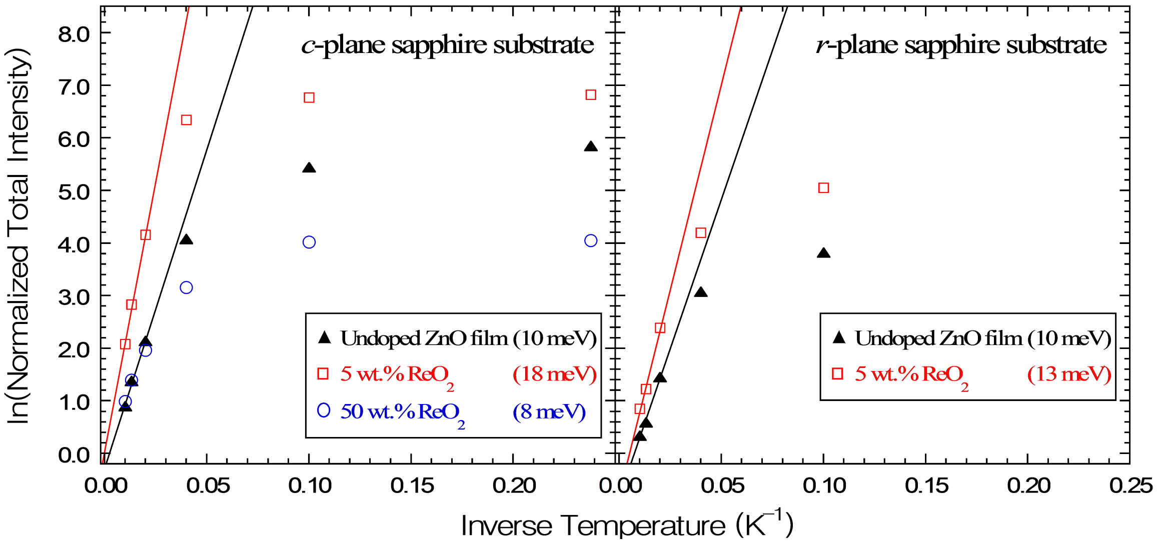

Figure 4.18: Natural logarithm of the normalized total intensity of the D^0X peak for ZnO deposited on *c*- and *r*-plane sapphire doped with various concentrations of ReO$_2$. The slope of the linear fit, or localization energy, of each specimen is shown in parenthesis in the legend.

Table 4.2: Localization energies determined from the slope of the linear portion of the plot of the natural logarithm of the normalized total intensity as a function of inverse temperature. Cells marked with '—' indicate insufficient peaks were resolvable to approximate the slope.

	Localization Energies		
	ZnO film, *c*-plane sapphire	**ZnO film, *r*-plane sapphire**	**Bulk ZnO (Hamby et al. [52])**
Undoped ZnO	10 meV	10 meV	14 meV
5% ReO$_2$	18 meV	13 meV	
10% ReO$_2$	14 meV	13 meV	
20% ReO$_2$	16 meV	—	
50% ReO$_2$	8 meV	—	

and 20 wt. % ReO_2 specimens deposited on c-plane sapphire exhibited the FX_A peak at 20 K. At 10 K, the FX_A peak was observed only as a shoulder with relatively low intensity. Similar to Section 4.1.3 for undoped specimens, the MW model was applied to the Re-doped specimens, the results of which can be seen in Fig. 4.19. Table 4.3 shows the constants obtained for the MW fits ($E = E_0 + UT^S + V\theta[\coth(\theta/2T) - 1]$) for each of the specimens. The T=0 intercept, E_0, was observed to range from 3.376 eV to 3.380 eV, which is consistent with the value reported for bulk ZnO, 3.379 eV [52]. The constant S was observed to range from 1.15-1.40, which agrees with reported values near unity [52]. The calculated values of V ranged from -1.5×10^{-4} to -2.2×10^{-4} eV/K, which were consistent with results reported for bulk ZnO, -1.8×10^{-4} eV/K [52].

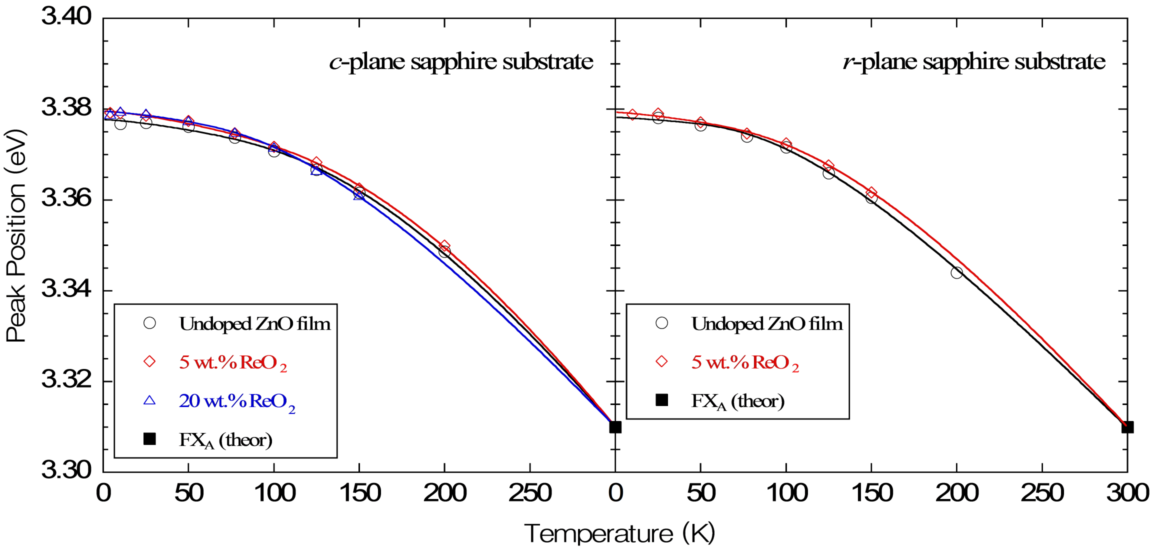

Figure 4.19: Temperature shift of the FX_A peak as a function of temperature for ZnO films deposited on c- and r-plane sapphire doped with various concentrations of ReO_2. Solid lines represent the Manoogian-Woolley (MW) fit for each specimen.

The parameters U, S, and θ_D were observed to vary the most from the reported results for bulk ZnO. U depends on several parameters, including the band gap shift with pressure, mean thermal expansion coefficient, and bulk modulus [55]. All observed values of U for the ZnO films were lower than the value reported for bulk ZnO. The smaller values of U observed for the ZnO films may be a result of changes in any of the parameters listed above. Cao and Chen [160] predicted that the elastic properties of ZnO films are close to those of bulk ZnO for nanofilms with thicknesses greater than 30 nm. However, the residual compressive strain in the ZnO films as indicated by Raman peak

Table 4.3: Parameters of the Manoogian-Woolley model for bulk and film ZnO specimens determined using a least squares routine. Cells marked with '—' indicate the results were insufficient to perform a reasonable fit of the data.

		E_0**(eV)**	U**(eV/K**$^{1.01}$**)**	S	V**(eV/K)**	θ**(K)**	θ_{D}**(K)**
Bulk ZnO (Hamby et al.)		3.379	-5.0×10^{-5}	1.01	$-1.8{\times}10^{-4}$	398	531
ZnO film, *c*-plane sapphire	Undoped	3.378	-9.8×10^{-6}	1.39	$-2.0{\times}10^{-4}$	575	766
	5% ReO_2	3.380	-1.2×10^{-5}	1.40	$-2.2{\times}10^{-4}$	671	894
	10% ReO_2	3.379	-1.6×10^{-5}	1.32	$-1.9{\times}10^{-4}$	557	742
	20% ReO_2	3.380	-9.9×10^{-6}	1.39	$-1.5{\times}10^{-4}$	417	557
	50% ReO_2	—	—	—	—	—	—
ZnO film, *r*-plane sapphire	Undoped	3.378	-1.3×10^{-5}	1.20	$-1.8{\times}10^{-4}$	354	471
	5% ReO_2	3.379	-1.3×10^{-5}	1.32	$-1.8{\times}10^{-4}$	457	609
	10% ReO_2	3.376	-2.2×10^{-6}	1.15	$-2.0{\times}10^{-4}$	341	455
	20% ReO_2	—	—	—	—	—	—
	50% ReO_2	—	—	—	—	—	—

shifting may alter the mechanical properties. Differences in the thermal expansion coefficients of the films and substrates could cause changes in strain levels as a function of temperature, which could also be responsible for changes in calculated value of U. The value of S was observed to be higher for the ZnO films, and is also related to the lattice dilatation term of the MW model. The films and substrates had a difference in thermal expansion coefficient of about -2.4% [83]. Therefore, the amount of residual compressive strain in the ZnO films should remain relatively constant as a function of temperature. However, some interaction between the film and substrate may be responsible for the differences obtained for these constants. The values obtained for U and S did not vary much as a function of ReO_2 concentration.

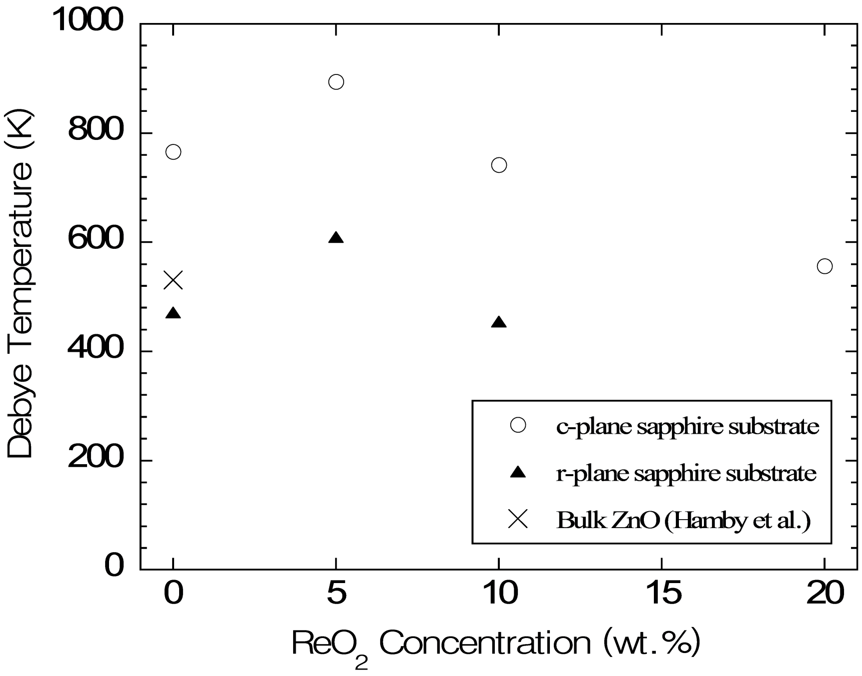

Figure 4.20: Estimated Debye temperature of bulk ZnO and ZnO films deposited on *c*- and *r*-plane sapphire backed out from the Manoogian-Woolley model.

The Debye temperature, θ_D, was observed to range from about 450 K to 900 K for all specimens. These values are all within about a factor of two of the reported value of the Debye temperature, 920 K [18]. Figure 4.20 shows the variation of the estimated Debye temperature as a function of ReO_2 concentration for all specimens. ZnO deposited on both *c*- and *r*-plane sapphire exhibit a higher Debye temperature with small Re doping concentrations. A maximum Debye temperature was observed from the 5 wt. % ReO_2 doped specimens for both *c*- and *r*-plane sapphire substrates. At ReO_2 concentrations above 5 wt. %, the Debye temperature decreased with increasing doping concentration. For a given doping concentration, the Debye temperature of the specimens deposited on *c*-plane sapphire was consistently about 300 K higher than the Debye temperature of specimens deposited on *r*-plane sapphire. The Debye temperature has been reported to depend on thermal transport dynamic properties and depends on various parameters, such as the nature of chemical bonding or crystallite size [161]. The higher Debye temperature observed from specimens deposited on *c*-plane sapphire may indicate higher crystalline quality ZnO with better thermal transport efficiency. Additionally, the high Debye temperature observed at low Re doping concentrations may indicate that the Re ions improve the crystalline quality and thermal transport efficiency in ZnO at low doping concentrations.

4.3 Behavior of Re in ReO_2-Doped ZnO Films

The experimental results of the ReO_2-doped ZnO films deposited on *c*- and *r*-plane sapphire presented in Section 4.2 indicated that a doping concentration of about 5-10 wt. % increased the crystalline quality of the ZnO films. At low doping concentrations, Raman spectroscopy revealed that the intensity of the ZnO E_2^{high} peak increased relative to the Al_2O_3 A_{1g} peak, which indicated an increase in crystalline quality. Spectral shifting of the ZnO Raman peak indicated that small Re doping concentrations decreased the amount of compressive strain in the ZnO films. The ionic radius of Re is reported to range from 0.67-0.77 Å depending on the charge, compared to 0.88 Å for Zn^{2+} [159]. Therefore, a plausible explanation for the decrease in strain is that at low doping concentrations, the Re ions substitute at Zn sites and relieve compressive strain in the film. PL spectroscopy revealed an increase in D^0X peak intensity and a decrease in DBX peak intensity for specimens with low Re doping concentrations. The DBX peak was reported to be a result of excitons bound to structural defects [41]. This was further indication that low Re doping concentrations increased the crystalline quality of the ZnO films. Finally, a fit of the data to the MW model indicated that the Debye temperature increased by about 150 K for low Re doping concentrations. The Debye temperature has been reported to depend on thermal transport properties, chemical bonding properties, and crystallite size [161]. If the Re ions substitute at Zn sites, chemical bonding will be altered, and an increase in thermal transport efficiency is possible. The increased PL emission intensity may be a result of the same mechanism in the ZnO films with low Re doping concentrations.

As ReO_2 doping concentrations were increased above 5-10 wt. %, changes were observed in the behavior of the optical response of the ZnO films. The intensity of the ZnO E_2^{high} peak decreased relative to the Al_2O_3 A_{1g} peak with increasing Re doping concentration. As ReO_2 doping concentrations were increased above 5 wt. %, PL emission intensity decreased. The Debye temperature, as estimated by the MW model, decreased with increasing doping concentration for specimens doped with concentrations greater than 5 wt. %. In the doping concentration range of 5-20 wt. %, two feasible mechanisms could be taking place that can explain this behavior. First, the number of Re ions being incorporated into the ZnO lattice structure at interstitial sites could be increasing with increasing Re concentration. Increasing the number of Re atoms at interstitial sites would increase strain and decrease the crystalline quality of the ZnO films. Second, a precipitated phase of ReO_2 could be forming in the ZnO films. This would also increase the compressive strain and decrease the crystalline quality. XRD revealed a well-resolved ReO_2 peak in the diffraction pattern of the 50 wt. % ReO_2 film deposited on *c*-plane sapphire, but for specimens with 5-20 wt. % ReO_2, this peak was not observed. This could indicate either that the concentration of the ReO_2 phase was too low to detect with XRD, or that no precipitated phase existed in these specimens.

In addition to the appearance of the ReO_2 peak in the diffraction pattern of the 50 wt. % ReO_2 specimens, the FWHM of the E_2^{high} peak increased. Wang et al. [162] characterized the compositional disorder of Mn-doped ZnO nanoparticles using the linewidth of the E_2^{high} peak, in which peak broadening was attributed to confined phonons as a result of lattice disorder. Šćepanović et al. [163] attributed peak broadening of the E_2^{high} peak of milled ZnO powders to lattice disorder and extended defects in the wurtzite structure. The PL spectrum of the 50 wt. % ReO_2 film deposited on *c*-plane sapphire showed a 20× decrease in D^0X emission intensity as compared to the undoped specimen. At 77 K, free exciton emission was observed in the spectra of all specimens except the 50 wt. % ReO_2 specimens. Re has been reported to cause variation in grain connectivity in a $Hg_{1-x}Re_xBa_2Ca_2Cu_3O_8$ material system with large Re concentrations [138]. A plausible explanation for the observed results in this study is that at a doping concentration of 50 wt. % ReO_2, a precipitated phase of ReO_2 exists at high concentrations, which could act to confine phonons, inhibit thermal transport, and possibly disrupt grain connectivity.

Chapter 5

Conclusions and Future Work

5.1 Conclusions

A study of the effects of Re doping on the optical response of ZnO films has been performed. Undoped and Re-doped ZnO films were deposited on *c*- an *r*-plane sapphire substrates using pulsed laser deposition (PLD). The films where characterized using X-ray diffraction (XRD), Raman spectroscopy, and photoluminescence (PL) spectroscopy. The undoped ZnO films were compared to bulk single crystal ZnO, and were then used as a baseline in the investigation of Re-doped ZnO films. Changes in the Raman and PL behavior as a function of Re doping suggested that a change in the physical incorporation of Re ions was taking place at relatively low doping concentrations. A list of specific conclusions are summarized as follows:

1. The XRD patterns for the ZnO films deposited on *c*-plane sapphire exhibited (0002)ZnO and (0002)Al_2O_3 peaks, and the ZnO films deposited on *r*-plane sapphire showed $(11\bar{2}0)$ZnO and $(02\bar{2}4)Al_2O_3$ peaks. For the 50 wt. % ReO_2 film deposited on *c*-plane sapphire, the (0002)ReO_2 peak appeared in the XRD pattern, which revealed that a precipitated phase of ReO_2 existed in this specimen.

2. The ZnO films doped with 5-10 wt. % ReO_2 exhibited an increase in intensity of the ZnO E_2^{high} Raman peak relative to the Al_2O_3 substrate, which suggested an increase in crystalline quality compared to undoped specimens. A spectral shift of the ZnO E_2^{high} peak to a lower wavenumber was also observed for these specimens, indicating a decrease in residual compressive strain. The behavior of the ZnO E_2^{high} peak reversed for the ZnO films doped with 20 and 50 wt. % ReO_2, which indicated a decrease in crystalline quality and an increase in residual compressive strain.

Additionally, the E_2^{high} peak of the ZnO film doped with 50 wt. % ReO_2 increased in width by about 15%, indicating increased lattice disorder.

3. PL measurements revealed an increase in the intensity of the D^0X peak for the 5 wt. % ReO_2 specimens as compared to undoped specimens. A decrease in the intensity of the DBX peak with increasing Re doping concentration suggested that low Re doping concentrations decrease the number of structural defects in the ZnO films. The Debye temperature, calculated using the Manoogian-Woolley (MW) model, increased for the ZnO films doped with 5 wt. % ReO_2, which may be the result of increased thermal transport efficiency. For specimens doped with more than 5 wt. % ReO_2, the overall intensity of the PL emission decreased and the Debye temperature decreased with increasing doping concentration, which suggested a decrease in crystalline quality and thermal transport efficiency.

4. A plausible explanation for the observed behavior was presented. At low doping concentrations, 5-10 wt. % ReO_2, Re ions primarily substitute at Zn sites. The smaller ionic radius of Re compared to Zn relieves he residual compressive strain in the films, and the crystalline quality increases. As doping concentration is increased above saturation, the number of Re ions found at interstitial sites increases, and the formation of a precipitated phase of ReO_2 may begin to form, which increases the residual compressive strain and disorder in the films. Finally, at concentrations as high as 50 wt. % ReO_2, a large amount of precipitated ReO_2 forms, as indicated by XRD.

5.2 Future Work

1. Using a technique such as side inclination XRD, investigate the lattice constants of the Re-doped ZnO films. This can be used to further characterize the behavior of the Re ions when incorporated into the ZnO lattice.

2. Investigate the Re doping saturation concentration in ZnO. High resolution XRD can be used to detect the first formation of ReO_2 in the ZnO films.

3. The effects of film thickness in combination with the results of this study should be investigated as film thickness has a major impact on the properties of thin films. Strain levels can be varied by changing film thickness, and the effect of Re doping of ZnO films of different thicknesses could enhance the fundamental understanding of the behavior of Re in ZnO.

4. Investigate the electrical properties of Re-doped ZnO. This could be used in conjunction with the increase in PL emission efficiency and thermal transport efficiency for specimens doped with small amounts of Re in this study to better understand the physics of Re-doped ZnO.

Bibliography

[1] C.V. Raman and K.S. Krishnan. A new type of secondary radiation. *Nature*, 121:501–502, 1928.

[2] J.G. Grasselli and B.J. Bulkin. *Analytical Raman Spectroscopy.* John Wiley & Sons, Inc., 1991.

[3] N.W. Ashcroft and N.D. Mermin. *Solid State Physics.* Brooks/Cole, 1st edition, 1976.

[4] S.M. Sze and K.N. Kwok. *Physics of Semiconductor Devices.* John Wiley & Sons, Inc., 3rd edition, 2007.

[5] M.S. Dresselhaus, D. Dresselhaus, and A. Jorio. *Group Theory: Application to the Physics of Condensed Matter.* Springer, 2008.

[6] M. Kitajima. Defects in crystals studied by Raman scattering. *Critical Reviews in Solid State and Materials Sciences*, 22:275–349, 1997.

[7] R.G. Sparks and M.A. Paesler. Micro-Raman analysis of stress in machined silicon and germanium. *Precision Engineering-Journal of the American Society for Precision Engineering*, 10:191–198, 1988.

[8] R.G. Sparks, W.S. Enloe, and M.A. Paesler. Micro-Raman depth analysis of residual stress in machined germanium. *Precision Engineering*, 13:189–195, 1991.

[9] S.B. Cronin, A.K. Swan, M.S. Unlu, B.B. Goldberg, M.S. Dresselhaus, and M. Tinkham. Measuring the uniaxial strain of individual single-wall carbon nanotubes: Resonance Raman spectra of atomic-force-microscope modified single-wall nanotubes. *Physical Review Letters*, 93, 2004.

[10] G. Gouadec and P. Colomban. Raman Spectroscopy of nanomaterials: How spectra relate to disorder, particle size and mechanical properties. *Progress in Crystal Growth and Characterization of Materials*, 53:1–56, 2007.

[11] G. Gouadec and P. Colomban. Raman spectroscopy of nanostructures and nanosized materials. *Journal of Raman Spectroscopy*, 38:598–603, 2007.

[12] T.H. Gfroerer. *Photoluminescence in analysis of surfaces and interfaces*. John Wiley & Sons, Inc., 2000.

[13] C. Kittel. *Introduction to Solid State Physics*. John Wiley & Sons, Inc., 8th edition.

[14] W.J.E. Beek, M.M. Wienk, and R.A.J. Janssen. Efficient hybrid solar cells from zinc oxide nanoparticles and a conjugated polymer. *Advanced Materials*, 16:1009–1013, 2004.

[15] W.J.E. Beek, M.M. Wienk, M. Kemerink, X.N. Yang, and R.A.J. Janssen. Hybrid zinc oxide conjugated polymer bulk heterojunction solar cells. *Journal of Physical Chemistry B*, 109:9505–9516, 2005.

[16] Y. Ryu, T.-S. Lee, J.A. Lubguban, H.W. White, B.-J. Kim, Y.-S. Park, and C.-J. Youn. Next generation of oxide photonic devices: ZnO-based ultraviolet light emitting diodes. *Applied Physics Letters*, 88:241108, 2006.

[17] C.F. Cline and D.R. Stephens. Volume compressibility of BeO and other II-VI compounds. *Journal of Applied Physics*, 36:2869, 1965.

[18] A.R. Hutson. Electronic properties of ZnO. *Journal of Physics and Chemistry of Solids*, 8:467–472, 1959.

[19] D.C. Reynolds, D.C. Look, B. Jogai, C.W. Litton, G. Cantwell, and W.C. Harsch. Valence-band ordering in ZnO. *Physical Review B*, 60:2340–2344, 1999.

[20] M.J. Brett and R.R. Parsons. Properties of transparent, conducting ZnO films deposited by reactive bias sputtering. *Solid State Communications*, 54:603–606, 1985.

[21] D.G. Thomas. The exciton spectrum of zinc oxide. *Journal of Physics and Chemistry of Solids*, 15:86–96, 1960.

[22] Y.S. Park, C.W. Litton, T.C. Collins, and D.C. Reynolds. Exciton spectrum of ZnO. *Physical Review*, 143:512–519, 1966.

[23] K. Kihara and G. Donnay. Anharmonic thermal vibrations in ZnO. *Canadian Mineralogist*, 23:647–654, 1985.

[24] Ü. Özgür, Y.I. Alivov, C. Liu, A. Teke, M.A. Reshchikov, S. Doğan, V. Avrutin, S.J. Cho, and H. Morkoc. A comprehensive review of ZnO materials and devices. *Journal of Applied Physics*, 98:041301, 2005.

[25] H. Karzel, W. Potzel, M. Köfferlein, W. Schiessl, M. Steiner, U. Hiller, G.M. Kalvius, D.W. Mitchell, T.P. Das, P. Blaha, K. Schwarz, and M.P. Pasternak. Lattice dynamics and hyperfine interactions in ZnO and ZnSe at high external pressures. *Physical Review B*, 53:11425–11438, 1996.

[26] N.I. Meyer, M.H. Jørgensen, and I. Balslev. Electroluminescence and current oscillations in ZnO single crystals excited by short pulses. *Solid State Communications*, 3:393–396, 1965.

[27] K. Saermark, V. Tarnow, N.Z. Heidam, and J. Lebech. Attenuation of 3 GHz sound waves in ZnO. *Solid State Communications*, 4:261, 1966.

[28] H. Lüth. Surface Phonons in the oscillatory photoconductivity of zinc oxide. *Physical Review Letters*, 29:1377–1379, 1972.

[29] K.I. Hagemark and L.C. Chacka. Electrical transport properties of Zn doped ZnO. *Journal of Solid State Chemistry*, 15:261–270, 1975.

[30] M. Jakani, G. Campet, J. Claverie, D. Fichou, J. Pouliquen, and J. Kossanyi. Photoelectrochemical properties of zinc oxide doped with 3d elements. *Journal of Solid State Chemistry*, 56:269–277, 1985.

[31] T.C. Damen, S.P.S. Porto, and B. Tell. Raman effect in zinc oxide. *Physical Review*, 142:570–574, 1966.

[32] N. Ashkenov, B.N. Mbenkum, C. Bundesmann, V. Riede, M. Lorenz, D. Spemann, E.M. Kaidashev, A. Kasic, M. Schubert, M. Grundmann, G. Wagner, H. Neumann, V. Darakchieva, H. Arwin, and B. Monemar. Infrared dielectric functions and phonon modes of high-quality ZnO films. *Journal of Applied Physics*, 93:126–133, 2003.

[33] F. Decremps, J. Pellicer-Porres, A.M. Saitta, J.C. Chervin, and A. Polian. High-pressure Raman spectroscopy study of wurtzite ZnO. *Physical Review B*, 65:092101, 2002.

[34] T.S. Jeong, M.S. Han, C.J. Youn, and Y.S. Park. Raman scattering and photoluminescence of As ion-implanted ZnO single crystal. *Journal of Applied Physics*, 96:175–179, 2004.

[35] T. Wermelinger and R. Spolenak. Symmetry of residual stress fields of ZnO below an indent measured by three-dimensional Raman spectroscopy. *Journal of Applied Physics*, 106:064907, 2009.

[36] J.L. Birman. Polarization of fluorescence in CdS and ZnS single crystals. *Physical Review Letters*, 2:157–159, 1959.

[37] M.R. Wagner. *Optical spectroscopy of defects and impurites in ZnO*. Diploma thesis, Technical University Berlin, 2005.

[38] D.C. Reynolds, C.W. Litton, and T.C. Collins. Zeeman effects in the edge emission and absorption of ZnO. *Physical Review*, 140:A1726, 1965.

[39] D.G. Thomas and J.J. Hopfield. Optical properties of bound exciton complexes in cadmium sulfide. *Physical Review*, 128:2135, 1962.

[40] W.Y. Liang and A.D. Yoffe. Transmission spectra of ZnO single crystals. *Physical Review Letters*, 20:59–62, 1968.

[41] B.K. Meyer, H. Alves, D.M. Hofmann, W. Kriegseis, D. Forster, F. Bertram, J. Christen, A. Hoffmann, M. Straβburg, M. Dworzak, U. Haboeck, and A.V. Rodina. Bound exciton and donor-acceptor pair recombinations in ZnO. *physica status solidi (b)*, 241:231–260, 2004.

[42] A. Teke, Ü. Özgür, S. Doğan, X. Gu, H. Morkoç, B. Nemeth, J. Nause, and H.O. Everitt. Excitonic fine structure and recombination dynamics in single-crystalline ZnO. *Physical Review B*, 70:195207, 2004.

[43] M. Schilling, R. Helbig, and G. Pensl. Bound exciton luminescence of Ar- and Al-implanted ZnO. *Journal of Luminescence*, 33:201–212, 1985.

[44] J. Gutowski, N. Presser, and I. Broser. Acceptor-exciton complexes in ZnO: A comprehensive analysis of their electronic states by high-resolution magnetooptics and excitation spectroscopy. *Physical Review B*, 38:9746–9758, 1988.

[45] H.J. Ko, Y.F. Chen, S.K. Hong, H. Wenisch, T. Yao, and D.C. Look. Ga-doped ZnO films grown on GaN templates by plasma-assisted molecular-beam epitaxy. *Applied Physics Letters*, 77:3761–3763, 2000.

[46] F. Williams. Donor-acceptor pairs in semiconductors. *physica status solidi*, 25:493, 1968.

[47] K. Thonke, T. Gruber, N. Teofilov, R. Schnfelder, A. Waag, and R. Sauer. Donoracceptor pair transitions in ZnO substrate material. *Physica B: Condensed Matter*, 308310:945–948, 2001.

[48] P.J. Dean. Comparison of MOCVD-grown with conventional II-VI materials parameters for EL thin-films. *physical status solidus (a)*, 81:625, 1984.

[49] S. Fujii, T. Terada, Y. Fujta, and T. Tuchi. New deep-level photoluminescence bands of homoepitaxial CdTe-films grown by metalorganic chemical vapor-deposition. *Japanese Journal of Applied Physics*, 28:L1712, 1989.

[50] A. Naumov, K. Wolf, T. Reisinger, H. Stanzl, and W. Gebhardt. Luminescence due to lattice-mismatch defects in ZnTe layers grown by metalorganic vapor phase epitaxy. *Journal of Applied Physics*, 73:2581, 1993.

[51] S. Fischer, G. Steude, D.M. Hofmann, F. Kurth, F. Anders, M. Topf, B.K. Meyer, F. Bertram, M. Schmidt, J. Christen, L. Eckey, J. Holst, A. Hoffmann, B. Mensching, and B. Rauschenbach. On the nature of the 3.41 eV luminescence in hexagonal GaN. *Journal of Crystal Growth*, 189:556–560, 1998.

[52] D.W. Hamby, D.A. Lucca, M.J. Klopfstein, and G. Cantwell. Temperature dependent exciton photoluminescence of bulk ZnO. *Journal of Applied Physics*, 93:3214–3217, 2003.

[53] A. Manoogian and J.C. Woolley. Temperature-dependence of the energy-gap in semiconductors. *Canadian Journal of Physics*, 62:285–287, 1984.

[54] Y.P. Varshni. Temperature dependence of the energy gap in semiconductors. *Physica (Amsterdam)*, 34:149, 1967.

[55] G. Fonthal, L. Tirado-Mejia, J.I. Marin-Hurtado, H. Ariza-Calderon, and J.G. Mendoza-Alvarez. *Journal of Physics and Chemistry of Solids*, 61:579, 2000.

[56] A. Manoogian. Determination of the dilation and vibrational contributions to the temperature shift of excitons in CdS: melting of semiconductors. *Canadian Journal of Physics*, 60:1490, 1982.

[57] L.J. Wang and N.C. Giles. Temperature dependence of the free-exciton transition energy in zinc oxide by photoluminescence excitation spectroscopy. *Journal of Applied Physics*, 94:973–978, 2003.

[58] G.D. Cody. Chapter 2: The Optical Absorption Edge of a-Si: H. *Semiconductors and Semimetals*, Volume 21, Part B, 1984.

[59] F.A. Kröger and H.J. Vink. The origin of the fluorescence in self-activated ZnS, CdS, and ZnO. *Journal of Chemical Physics*, 22:250–252, 1954.

[60] R. Dingle. Luminescent transitions associated with divalent copper impurities and the green emission from semiconducting zinc oxide. *Physical Review Letters*, 23:579–581, 1969.

[61] M. Liu, A.H. Kitai, and P. Mascher. Point-defects and luminescence-centers in zinc-oxide and zinc-oxide doped with manganese. *Journal of Luminescence*, 54:35–42, 1992.

[62] K. Vanheusden, W.L. Warren, C.H. Seager, D.R. Tallant, J.A. Voigt, and B.E. Gnade. Mechanisms behind green photoluminescence in ZnO phosphor powders. *Journal of Applied Physics*, 79:7983–7990, 1996.

[63] H.-J. Egelhaaf and D. Oelkrug. Luminescence and nonradiative deactivation of excited states involving oxygen defect centers in polycrystalline ZnO. *Journal of Crystal Growth*, 161:190–194, 1996.

[64] A.F. Kohan, G. Ceder, D. Morgan, and C.G. Van de Walle. First-principles study of native point defects in ZnO. *Physical Review B*, 61:15019–15027, 2000.

[65] S.A. Studenikin, N. Golego, and M. Cocivera. Fabrication of green and orange photoluminescent,undoped ZnO films using spray pyrolysis. *Journal of Applied Physics*, 84:2287–2294, 1998.

[66] B. Guo, Z.R. Qiu, and K.S. Wong. Intensity dependence and transient dynamics of donor-acceptor pair recombination in ZnO thin films grown on (001) silicon. *Applied Physics Letters*, 82:2290–2292, 2003.

[67] Y.W. Heo, D.P. Norton, and S.J. Pearton. Origin of green luminescence in ZnO thin film grown by molecular-beam epitaxy. *Journal of Applied Physics*, 98:073502, 2005.

[68] N.O. Korsunska, L.V. Borkovska, B.M. Bulakh, L.Y. Khomenkova, V.I. Kushnirenko, and I.V. Markevich. The influence of defect drift in external electric field on green luminescence of ZnO single crystals. *Journal of Luminescence*, 102103:733–736, 2003.

[69] B. Lin, Z. Fu, and Y. Jia. Green luminescent center in undoped zinc oxide films deposited on silicon substrates. *Applied Physics Letters*, 79:943–945, 2001.

[70] X.W. Du, Y.S. Fu, J. Sun, X. Han, and J. Liu. Complete UV emission of ZnO nanoparticles in a PMMA matrix. *Semiconductor Science and Technology*, 21:1202–1206, 2006.

[71] X. Liu, X.H. Wu, H. Cao, and R.P.H. Chang. Growth mechanism and properties of ZnO nanorods synthesized by plasma-enhanced chemical vapor deposition. *Journal of Applied Physics*, 95:3141–3147, 2004.

[72] V. Srikant and D.R. Clarke. Optical absorption edge of ZnO thin films: The effect of substrate. *Journal of Applied Physics*, 81:6357–6364, 1997.

[73] J.F. Muth, R.M. Kolbas, A.K. Sharma, S. Oktyabrsky, and J. Narayan. Excitonic structure and absorption coefficient measurements of ZnO single crystal epitaxial films deposited by pulsed laser deposition. *Journal of Applied Physics*, 85:7884–7887, 1999.

[74] X.L. Wu, G.G. Siu, C.L. Fu, and H.C. Ong. Photoluminescence and cathodoluminescence studies of stoichiometric and oxygen-deficient ZnO films. *Applied Physics Letters*, 78:2285–2287, 2001.

[75] J.M. Myoung, W.H. Yoon, D.H. Lee, I. Yun, S.H. Bae, and S.Y. Lee. Effects of thickness variation on properties of ZnO thin films grown by pulsed laser deposition. *Japanese Journal of Applied Physics*, 41:28–31, 2002.

[76] H.C. Ong, A.X.E. Zhu, and G.T. Du. Dependence of the excitonic transition energies and mosaicity on residual strain in ZnO thin films. *Applied Physics Letters*, 80:941–943, 2002.

[77] E.S. Shim, H.S. Kang, J.S. Kang, J.H. Kim, and S.Y. Lee. Effect of the variation of film thickness on the structural and optical properties of ZnO thin films deposited on sapphire substrate using PLD. *Applied Surface Science*, 186:474–476, 2002.

[78] Y.F. Chen, D.M. Bagnall, H.J. Koh, K.T. Park, K. Hiraga, Z.Q. Zhu, and T. Yao. Plasma assisted molecular beam epitaxy of ZnO on c-plane sapphire: Growth and characterization. *Journal of Applied Physics*, 84:3912–3918, 1998.

[79] A. Ohtomo, M. Kawasaki, I. Ohkubo, H. Koinuma, T. Yasuda, and Y. Segawa. Structure and optical properties of ZnO/$Mg_{0.2}Zn_{0.8}O$ superlattices. *Applied Physics Letters*, 75:980–982, 1999.

[80] T. Makino, T. Yasuda, Y. Segawa, A. Ohtomo, K. Tamura, M. Kawasaki, and H. Koinuma. Strain effects on exciton resonance energies of ZnO epitaxial layers. *Applied Physics Letters*, 79:1282–1284, 2001.

[81] A. Tsukazaki, A. Ohtomo, T. Onuma, M. Ohtani, T. Makino, M. Sumiya, K. Ohtani, S.F. Chichibu, S. Fuke, Y. Segawa, H. Ohno, H. Koinuma, and M. Kawasaki. Repeated temperature modulation epitaxy for p-type doping and light-emitting diode based on ZnO. *Nature Materials*, 4:42–46, 2005.

[82] K.K. Kim, J.H. Song, H.J. Jung, W.K. Choi, and S.J. Park. The grain size effects on the photoluminescence of ZnO/alpha-Al_2O_3 grown by radio-frequency magnetron sputtering. *Journal of Applied Physics*, 87:3573–3575, 2000.

[83] J.P. Liu, S.C. Qu, X.B. Zeng, Y. Xu, X.F. Gou, Z.J. Wang, H.Y. Zhou, and Z.G. Wang. Fabrication of ZnO and its enhancement of charge injection and transport in hybrid organic/inorganic light emitting devices. *Applied Surface Science*, 253:7506–7509, 2007.

[84] B.C. Mohanty, Y.H. Jo, D.H. Yeon, I.J. Choi, and Y.S. Cho. Stress-induced anomalous shift of optical band gap in ZnO:Al thin films. *Applied Physics Letters*, 95:062103, 2009.

[85] J. Hinze and K. Ellmer. In situ measurement of mechanical stress in polycrystalline zinc-oxide thin films prepared by magnetron sputtering. *Journal of Applied Physics*, 88:2443–2450, 2000.

[86] C.R. Gorla, N.W. Emanetoglu, S. Liang, W.E. Mayo, Y. Lu, M. Wraback, and H. Shen. Structural, optical, and surface acoustic wave properties of epitaxial ZnO films grown on $(01\bar{1}2)$ sapphire by metalorganic chemical vapor deposition. *Journal of Applied Physics*, 85:2595–2602, 1999.

[87] B.P. Zhang, N.T. Binh, K. Wakatsuki, C.Y. Liu, Y. Segawa, and N. Usami. Growth of ZnO/MgZnO quantum wells on sapphire substrates and observation of the two-dimensional confinement effect. *Applied Physics Letters*, 86:032105, 2005.

[88] Y.F. Li, B. Yao, Y.M. Lu, C.X. Cong, Z.Z. Zhang, Y.Q. Gai, C.J. Zheng, B.H. Li, Z.P. Wei, D.Z. Shen, X.W. Fan, L. Xiao, S.C. Xu, and Y. Liu. Characterization of biaxial stress and its effect on optical properties of ZnO thin films. *Applied Physics Letters*, 91:021915, 2007.

[89] Y.F. Li, B. Yao, Y.M. Lu, Y.Q. Gai, C.X. Cong, Z.Z. Zhang, D.X. Zhao, J.Y. Zhang, B.H. Li, D.Z. Shen, X.W. Fan, and Z.K. Tang. Biaxial stress-dependent optical band gap, crystalline, and electronic structure in wurtzite ZnO: Experimental and ab initio study. *Journal of Applied Physics*, 104:083516, 2008.

[90] R. Ghosh, D. Basak, and S. Fujihara. Effect of substrate-induced strain on the structural, electrical, and optical properties of polycrystalline ZnO thin films. *Journal of Applied Physics*, 96:2689–2692, 2004.

[91] C.H. Park, S.B. Zhang, and S.-H. Wei. Origin of p-type doping difficulty in ZnO: The impurity perspective. *Physical Review B*, 66:073202, 2002.

[92] J.K. Lee, T.A. Harriman, D.A. Lucca, H.S. Jung, D.B. Ryan, and M. Nastasi. Dynamic recovery and optical properties changes in He-implanted ZnO nanoparticles. *Nuclear Instruments & Methods in Physics Research Section B-Beam Interactions with Materials and Atoms*, 257:71–74, 2007.

[93] M. Gao, J. Yang, L. Yang, Y. Zhang, J. Lang, H. Liu, H. Fan, Y. Sun, Z. Zhang, and H. Song. Enhancement of optical properties and donor-related emissions in Y-doped ZnO. *Superlattices and Microstructures*, 52:84–91, 2012.

[94] S. Major, A. Banerjee, and K.L. Chopra. Highly transparent and conducting indium-doped zinc oxide films by spray pyrolysis. *Thin Solid Films*, 108:333–340, 1983.

[95] T. Minami, H. Sato, H. Nanto, and S. Takata. Group-III impurity doped zinc-oxide thin-films prepared by rf magnetron sputtering. *Japanese Journal of Applied Physics Part 2-Letters*, 24:L781–L784, 1985.

[96] B.M. Ataev, A.M. Bagamadova, A.M. Djabrailov, V.V. Mamedov, and R.A. Rabadanov. Highly conductive and transparent Ga-doped epitaxial ZnO films on sapphire by CVD. *Thin Solid Films*, 260:19–20, 1995.

[97] V. Assunção, E. Fortunato, A. Marques, H. Águas, I. Ferreira, M.E.V. Costa, and R. Martins. Influence of the deposition pressure on the properties of transparent and conductive ZnO:Ga thin-film produced by r.f. sputtering at room temperature. *Thin Solid Films*, 427:401–405, 2003.

[98] Z.F. Liu, F.K. Shan, Y.X. Li, B.C. Shin, and Y.S. Yu. Epitaxial growth and properties of Ga-doped ZnO films grown by pulsed laser deposition. *Journal of Crystal Growth*, 259:130–136, 2003.

[99] T. Minami, H. Nanto, and S. Takata. Highly conductive and transparent aluminum doped zinc-oxide thin-films prepared by rf magnetron sputtering. *Japanese Journal of Applied Physics Part 2-Letters*, 23:L280–L282, 1984.

[100] S.Y. Myong, S.J. Baik, C.H. Lee, W.Y. Cho, and K.S. Lim. Extremely transparent and conductive ZnO:Al thin films prepared by photo-assisted metalorganic chemical vapor deposition (photo-MOCVD) using $AlCl_3(6H_2O)$ as new doping material. *Japanese Journal of Applied Physics Part 2-Letters*, 36:L1078–L1081, 1997.

[101] H.P. He, F. Zhuge, Z.Z. Ye, L.P. Zhu, F.Z. Wang, B.H. Zhao, and J.Y. Huang. Strain and its effect on optical properties of Al-N codoped ZnO films. *Journal of Applied Physics*, 99:023503, 2006.

[102] H. Kato, M. Sano, K. Miyamoto, and T. Yao. Growth and characterization of Ga-doped ZnO layers on a-plane sapphire substrates grown by molecular beam epitaxy. *Journal of Crystal Growth*, 237239, Part 1:538–543, 2002.

[103] D.W. Langer and H.J. Richter. Zero-phonon lines and phonon coupling of ZnSe - Mn and CdS - Mn. *Physical Review*, 146:554, 1966.

[104] C. Ehrlich, W. Busse, H.E. Gumlich, and D. Tschierse. Luminescence of $Cd_{1-x}Mn_xS$ within the concentration range $0.0001 \leq x \leq 0.28$. *Journal of Crystal Growth*, 72:371–375, 1985.

[105] Y. Kanemitsu, H. Matsubara, and C.W. White. Optical properties of Mn-doped CdS nanocrystals fabricated by sequential ion implantation. *Applied Physics Letters*, 81:535–537, 2002.

[106] H. Ohno. Making nonmagnetic semiconductors ferromagnetic. *Science*, 281:951–956, 1998.

[107] T. Fukumura, Z.W. Jin, A. Ohtomo, H. Koinuma, and M. Kawasaki. An oxide-diluted magnetic semiconductor: Mn-doped ZnO. *Applied Physics Letters*, 75:3366–3368, 1999.

[108] Z.W. Jin, T. Fukumura, M. Kawasaki, K. Ando, H. Saito, T. Sekiguchi, Y.Z. Yoo, M. Murakami, Y. Matsumoto, T. Hasegawa, and H. Koinuma. High throughput fabrication of transition-metal-doped epitaxial ZnO thin films: A series of oxide-diluted magnetic semiconductors and their properties. *Applied Physics Letters*, 78:3824–3826, 2001.

[109] K. Ueda, H. Tabata, and T. Kawai. Magnetic and electric properties of transition-metal-doped ZnO films. *Applied Physics Letters*, 79:988–990, 2001.

[110] Y.W. Heo, M.P. Ivill, K. Ip, D.P. Norton, S.J. Pearton, J.G. Kelly, R. Rairigh, A.F. Hebard, and T. Steiner. Effects of high-dose Mn implantation into ZnO grown on sapphire. *Applied Physics Letters*, 84:2292–2294, 2004.

[111] S. Thota, T. Dutta, and J. Kumar. On the sol-gel synthesis and thermal, structural, and magnetic studies of transition metal (Ni, Co, Mn) containing ZnO powders. *Journal of Physics-Condensed Matter*, 18:2473–2486, 2006.

[112] J. Das, D.K. Mishra, D.R. Sahu, and B.K. Roul. Structural and magnetic property of Mn:ZnO bulk ceramic doped with rare earth (Gd/Sm) atoms. *Physica B: Condensed Matter*, 407:3575–3579, 2012.

[113] H.-J. Lee, S.Y. Jeong, C.R. Cho, and C.H. Park. Study of diluted magnetic semiconductor: Co-doped ZnO. *Applied Physics Letters*, 81:4020–4022, 2002.

[114] B.D. Ngom, O. Sakho, N. Manyala, J.B. Kana, N. Mlungisi, L. Guerbous, A.Y. Fasasi, M. Maaza, and A.C. Beye. Structural, morphological and photoluminescence properties of W-doped ZnO nanostructures. *Applied Surface Science*, 255:7314–7318, 2009.

[115] B.D. Ngom, M. Chaker, N. Manyala, B. Lo, M. Maaza, and A.C. Beye. Temperature-dependent growth mode of W-doped ZnO nanostructures. *Applied Surface Science*, 257:6226–6232, 2011.

[116] C. Bundesmann, N. Ashkenov, M. Schubert, D. Spemann, T. Butz, E.M. Kaidashev, M. Lorenz, and M. Grundmann. Raman scattering in ZnO thin films doped with Fe, Sb, Al, Ga, and Li. *Applied Physics Letters*, 83:1974–1976, 2003.

[117] W.F. Meggers. Rhenium. *Scientific Monthly*, 33:413–418, 1931.

[118] Y.L. Li and Z. Zeng. Structural, elastic and electronic properties of ReO_2. *Chinese Physics Letters*, 25:4086–4089, 2008.

[119] M. Doerr. Coexistent phases and their electrical and structural behaviour in the ternary Re/Mo/O system. *Crystal Research and Technology*, 31:231, 1996.

[120] P. Gibart. Physico-chemical properties of rhenium dioxides. *Bulletin De La Societe Chimique De France*, 2:444, 1967.

[121] J. Wu, H.-Y. Li, L.-C. Kang, D.-P. Li, H.-R. Li, X.-H. Zhou, Y. Sui, Y.-X. Zheng, J.-L. Zuo, and X.-Z. You. Synthesis and photoluminescence properties of four rhenium(I) complexes based on diimine ligands with oxadiazole/carbazole moiety. *Journal of Photochemistry and Photobiology A: Chemistry*, 211:135–142, 2010.

[122] Y. Wang, H.-J. Mao, G.-Q. Zang, Y.-S. Yu, and Z.-H. Tang. Photoluminescence properties of Re(I) complex doped composite submicron fibers prepared by electrospinning. *Spectrochimica Acta Part A: Molecular and Biomolecular Spectroscopy*, 78:469–473, 2011.

[123] A.O.E. Animalu. Electronic structure of transition metals. II. Phonon spectra. *Physical Review B*, 8:3555–3562, 1973.

[124] G.K. Straub and W.A. Harrison. Analytic methods for the calculation of the electronic structure of solids. *Physical Review B*, 31:7668–7679, 1985.

[125] R.W. Powell, R.P. Tye, and M.J. Woodman. The thermal conductivity and electrical resistivity of rhenium. *Journal of the Less Common Metals*, 5:49–56, 1963.

[126] R.J. Gambino and P.E. Seiden. Correlation of the superconducting transition temperature with an empirical pseudopotential determined from atomic spectra. *Physical Review B*, 2:3571–3577, 1970.

[127] P. Sisodia and M.P. Verma. Polycrystalline elastic-moduli of some hexagonal and tetragonal materials. *physica status solidi a-Applied Research*, 122:525–534, 1990.

[128] Y. Makino and S. Miyake. Estimation of bulk moduli of compounds by empirical relations between bulk modulus and interatomic distance. *Journal of Alloys and Compounds*, 313:235–241, 2000.

[129] D. Late, P. Misra, B. Singh, L. Kukreja, D. Joag, and M. More. Enhanced field emission from pulsed laser deposited nanocrystalline ZnO thin films on Re andW. *Applied Physics A: Materials Science & Processing*, 95:613–620, 2009.

[130] J.-G. Han, Z.-Y. Ren, and B.-Z. Lu. Geometries and stabilities of Re-doped $\mathrm{Si_n}$ (n = 1-12) clusters: A density functional investigation. *The Journal of Physical Chemistry A*, 108:5100–5110, 2004.

[131] V.M. Andreev, N.S. Zimogorova, L.B. Karlina, L.P. Nikitin, V.M. Ustinov, and A.M. Vasilev. Photoluminescence properties of rhenium-doped $\mathrm{In_{0.53}Ga_{0.47}As}$ solid-solutions. *Soviet Physics Semiconductors-USSR*, 23:382–384, 1989.

[132] V.M. Andreev, A.M. Vasilev, N.S. Zimogorova, V.M. Lantratov, and V.I. Myrzin. Photoluminescence of rhenium-doped GaAs. *Soviet Physics Semiconductors-USSR*, 24:753–756, 1990.

[133] M.K. Agarwal, P.D. Patel, and S.K. Gupta. Effect of doping $MoSe_2$ single crystals with rhenium. *Journal of Crystal Growth*, 129:559–562, 1993.

[134] M.M. Vora and A.M. Vora. Effect of rhenium doping on various properties of $MoSe_2$ single crystal. *Chalcogenide Letters*, 4:97–100, 2007.

[135] V.M. Skorikov, T.I. Milenov, A.V. Egorysheva, P.M. Rafailov, T.D. Dudkina, M.N. Veleva, A.Y. Vasil'ev, and M.M. Gospodinov. An optical excitation study of Ru-, Rh-, Re- and Os-doped $Bi_{12}SiO_{20}$ crystals. *physica status solidi (b)*, 244:3292–3296, 2007.

[136] P.C. Yen, H.P. Hsu, Y.T. Liu, Y.S. Huang, and K.K. Tiong. Temperature dependences of energies and broadening parameters of the band-edge excitons of Re-doped WS_2 and $2H - WS_2$ single crystals. *Journal of Physics-Condensed Matter*, 16:6995–7005, 2004.

[137] L. Zhang, F. Yan, M. Su, G. Han, and P. Kang. A study on the degradation of methamidophos in the presence of $nano - TiO_2$ catalyst doped with Re. *Russian Journal of Inorganic Chemistry*, 54:1210–1216, 2009.

[138] M. Reder, J. Krelaus, L. Schmidt, K. Heinemann, and H.C. Freyhardt. Effects of Re-doping on microstructure and superconductivity of $HgBa_2Ca_2Cu_3O_{8+\delta}$. *Physica C: Superconductivity*, 306:289–299, 1998.

[139] D.S. Leem, H.D. Park, J.W. Kang, J.H. Lee, J.W. Kim, and J.J. Kim. Low driving voltage and high stability organic light-emitting diodes with rhenium oxide-doped hole transporting layer. *Applied Physics Letters*, 91:011113, 2007.

[140] R.R. Monchamp. Preparation and properties of crystalline laser oxide materials. *Journal of Solid State Chemistry*, 12:201–206, 1975.

[141] C.C. Zheng, S.J. Xu, J.Q. Ning, W. Bao, J.F. Wang, J. Gao, J.M. Liu, J.H. Zhu, and X.L. Liu. Residual strains and optical properties of ZnO thin epilayers grown on r-sapphire planes. *Semiconductor Science and Technology*, 27:035008, 2012.

[142] R.S. Krishnan. Raman spectrum of alumina and the luminescence and absorption spectra of ruby. *Nature*, 160:26–26, 1947.

[143] S.P.S. Porto and R.S. Krishnan. Raman effect of corundum. *Journal of Chemical Physics*, 47:1009–1012, 1967.

[144] H. Yoshikawa and S. Adachi. Optical constants of ZnO. *Japanese Journal of Applied Physics Part 1-Regular Papers Short Notes & Review Papers*, 36:6237–6243, 1997.

[145] M.E. Innocenzi, R.T. Swimm, M. Bass, R.H. French, A.B. Villaverde, and M.R. Kokta. Room-temperature optical absorption in undoped α-Al_2O_3. *Journal of Applied Physics*, 67:7542–7546, 1990.

[146] J.W. Beletic. *Optics in Astrophysics*. Springer-Verlag, 1st edition, 2005.

[147] T.A. Harriman. *Effects of lanthanoid ion implantation on the photoluminescence of silicon nanocrystals embedded in silicon nitride films*. Thesis, Oklahoma State University, 2008.

[148] W.R. Liu, B.H. Lin, C.C. Kuo, W.C. Lee, M. Hong, J. Kwo, C.H. Hsu, and W.F. Hsieh. Thickness-dependent lattice relaxation and the associated optical properties of ZnO epitaxial films grown on Si (111). *CrystEngComm*, 14:8103–8109, 2012.

[149] F. Hennrich, R. Krupke, S. Lebedkin, K. Arnold, R. Fischer, D.E. Resasco, and M.M. Kappes. Raman Spectroscopy of Individual Single-Walled Carbon Nanotubes from Various Sources. *The Journal of Physical Chemistry B*, 109:10567–10573, 2005.

[150] A.T. Maccarone. *Infrared spectroscopy of matrix isolated organic peroxyl radicals*. Thesis, University of Colorado at Boulder, 2007.

[151] K.F. McCarty. Raman scattering as a technique of measuring film thickness: interference effects in thin growing films. *Applied Optics*, 26:4482–4486, 1987.

[152] T. Sovány, K. Nikowitz, G. Regdon, P. Kása, and K. Pintye-Hódi. Raman spectroscopic investigation of film thickness. *Polymer Testing*, 28:770–772, 2009.

[153] D.W. Hamby, D.A. Lucca, and M.J. Klopfstein. Photoluminescence of mechanically polished ZnO. *Journal of Applied Physics*, 97, 2005.

[154] H. Watanabe, M. Wada, and T. Takahashi. Optical and Electrical Properties of ZnO Crystals. *Japanese Journal of Applied Physics*, 3:617, 1964.

[155] L. Bøtter-Jensen, S.W.S. McKeever, and A.G. Wintle. *Optically Stimulated Luminescence Dosimetry*. Elsevier, 1st edition, 2003.

[156] M. Watanabe, M. Sakai, H. Shibata, C. Satou, S. Satou, T. Shibayama, H. Tampo, A. Yamada, K. Matsubara, K. Sakurai, S. Ishizuka, S. Niki, K. Maeda, and I. Niikura. Negative thermal quenching of photoluminescence in ZnO. *Physica B: Condensed Matter*, 376377:711–714, 2006.

[157] S. Tanaka, Y. Ishikawa, T. Suzuki, and N. Shibata. Photoluminescence from ZnO thin film deposited on r-plane sapphire substrate by RF magnetron sputtering. *Key Engineering Materials*, 388:19–22, 2009.

[158] A. Kuzmin, J. Purans, E. Cazzanelli, C. Vinegoni, and G. Mariotto. X-ray diffraction, extended x-ray absorption fine structure and Raman spectroscopy studies of $\mathrm{WO_3}$ powders and, $(1-x)\mathrm{WO}_{3-y}\cdot x\mathrm{ReO_2}$ mixtures. *Journal of Applied Physics*, 84:5515–5524, 1998.

[159] R.D. Shannon. Revised effective ionic-radii and systematic studies of interatomic distances in halides and chalcogenides. *Acta Crystallographica Section A*, 32:751–767, 1976.

[160] G. Cao and X. Chen. Energy analysis of size-dependent elastic properties of ZnO nanofilms using atomistic simulations. *Physical Review B*, 76:165407, 2007.

[161] M.X. Gu, C.Q. Sun, Z. Chen, T.C. Au Yeung, S. Li, C.M. Tan, and V. Nosik. Size, temperature, and bond nature dependence of elasticity and its derivatives on extensibility, Debye temperature, and heat capacity of nanostructures. *Physical Review B*, 75:125403, 2007.

[162] J.B. Wang, H.M. Zhong, Z.F. Li, and W. Lu. Raman study for E-2 phonon of ZnO in $\mathrm{Zn_{1-x}Mn_xO}$ nanoparticles. *Journal of Applied Physics*, 97:086105, 2005.

[163] M. Šćepanović, M. Grujić-Brojčin, K. Vojisavljević, S. Bernik, and T. Srećković. Raman study of structural disorder in ZnO nanopowders. *Journal of Raman Spectroscopy*, 41:914–921, 2010.

VITA

Daniel Steven Hildebrand

Candidate for the Degree of

Master of Science

Thesis: OPTICAL RESPONSE OF DOPED ZINC OXIDE FILMS

Major Field: Mechanical and Aerospace Engineering

Biographical:

Personal Data: Born in Tulsa, OK, USA on June 20, 1987.

Education:
Received the Bachelor of Science degree from Oklahoma State University, Stillwater, Oklahoma, USA in Mechanical Engineering in May 2009. Completed the requirements for the degree of Master of Science in Mechanical and Aerospace Engineering at Oklahoma State University, Stillwater, Oklahoma in November, 2012.

Experience:
Math tutor, Oklahoma State University, 2007 to 2009. Graduate research and teaching assistant, Oklahoma State University, 2009 to 2011. Mechanical Engineer, Tinker Air Force Base, 2011 to present.

Professional Memberships:
Pi Tau Sigma member.

Name: Daniel S. Hildebrand Date of Degree: December, 2012

Institution: Oklahoma State University Location: Stillwater, Oklahoma

Title of Study: OPTICAL RESPONSE OF DOPED ZINC OXIDE FILMS

Pages in Study: 84 Candidate for the Degree of Master of Science

Major Field: Mechanical & Aerospace Engineering

Re-doped ZnO thin films were deposited on *c*-plane and *r*-plane sapphire substrates using pulsed laser deposition (PLD). The effects of doping ZnO with Re were investigated using X-ray diffraction (XRD), Raman spectroscopy, and photoluminescence (PL) spectroscopy. Comparisons to bulk single crystal ZnO indicated the films were of high crystalline quality. It was revealed that low doping concentrations of Re (5-10 wt. % ReO_2) increased the crystalline quality and decreased the residual compressive strain of the ZnO films. PL spectroscopy showed that the donor bound exciton emission increased in intensity, and a structural defect related peak, DBX, decreased in intensity. The Debye temperature of films doped with 5 wt. % ReO_2 increased as calculated using the Manoogian-Woolley model. The ZnO E_2^{high} Raman peak increased in intensity relative to the Al_2O_3 substrate Raman peak and shifted to a lower wavenumber. Higher doping concentrations (10-50 wt. % ReO_2) resulted in a decrease in crystalline quality and an increase in residual compressive strain. The intensity of the donor bound exciton emission decreased and the calculated Debye temperature decreased with increasing doping concentration. The E_2^{high} Raman peak decreased in relative intensity and shifted to a higher wavenumber. A plausible explanation for this behavior is that the Re ions substitute at Zn sites up to a certain saturation threshold, after which the number of Re ions found at interstitial sites increases. Additionally, the formation of precipitated ReO_2 was detected by XRD for the 50 wt. % ReO_2 film deposited on *c*-plane sapphire. The precipitate phase may begin to form at lower Re doping concentrations, and may contribute to the increase in residual compressive strain and decrease in crystalline quality of the ZnO films.

ADVISOR'S APPROVAL: ____________________